INVESTIGATING DESIGN RULES IN ELECTRODES FOR FLUORIDE-ION BATTERIES

Don Heywood McTaggart

A dissertation submitted to the faculty at the University of North Carolina at Chapel Hill in partial fulfillment of the requirements for the degree of Doctor of Philosophy in the Department of Chemistry.

Chapel Hill
2026

Approved by:

James F. Cahoon

Megan N. Jackson

Yosuke Kanai

Shubin Liu

Scott C. Warren

© 2026
Don Heywood McTaggart
ALL RIGHTS RESERVED

ABSTRACT

Don H. McTaggart: Investigating Design Rules in Electrodes for Fluoride-Ion Batteries
(Under the direction of Scott C. Warren)

The expansion of renewable energy is increasing demand for battery chemistries that can deliver high energy density, improved safety, and reduced dependence on critical minerals. Lithium-ion batteries (LIBs) remain dominant, but their long-term limitations have increased interest in chemistries beyond lithium. Among these, fluoride-ion batteries (FIBs) offer an attractive alternative. FIBs are promising because they combine high theoretical energy densities and wide electrochemical stability windows with the natural abundance of fluorine. Despite these advantages, FIBs remain at an early stage of development. Practical progress has been constrained by a narrow electrode design space, uncertainty surrounding material compatibility within electrode composites, and limited understanding of how electronic structure governs anionic storage in promising host materials. This dissertation addresses these problems by investigating what design rules determine FIB material viability, and how those rules can be used to guide rational electrode development.

My dissertation develops a three-part framework spanning composition, composite compatibility, and electronic structure in FIB electrodes. First, I perform a high-throughput thermodynamic screening of more than 5,000 ternary fluoride compounds from the Materials Project database to identify promising cathode charge/discharge pairs and assess cycling stability. This workflow identifies the ABF_6 family as a promising cathode class and is connected to experiment through optimization of a low-cost synthesis route for $NaVF_4$ as a prototype cathode. Second, I extend the same thermodynamic screening logic to parasitic carbon side reactions in electrode composites by evaluating 930 competing metal fluoride and metal carbide formation reactions. This analysis establishes composition-dependent rules showing that carbon additives are generally compatible with late transition metal fluorides but more vulnerable to degradation in systems containing alkali, alkaline earth, and early transition metals. Third, I

investigate disorder in rocksalt Ti_2C using cluster expansion, Monte Carlo simulations, and BadELF analysis to determine whether electride-like electron topology survives loss of long-range order. These calculations show that the fully ordered Ti_2C ground state is kinetically inaccessible, yet the three-dimensional electron network remains robust over a wide range of carbon configurations. Together, these studies establish transferable design rules for discovering and evaluating FIB electrodes.

Fall seven times, stand up eight.

ACKNOWLEDGEMENTS

To my advisor, Professor Scott Warren, thank you for your care to my growth as a scientist. Your steady mentorship created an environment for me to absorb and develop effective ways of thinking about complex problems. This process asks a great deal of patience of the mentor, and I truly appreciate your support.

To the Warren Lab, especially Connor, Becca, Lauren, Sam, Hye Sol, Duncan, Karen, and Matt, thank you being great collogues and friends during my time at UNC. They say you become the average of the people you spend the most time with, and our years together make me proud to be a composite of you all.

To my graduate school friends, thank you for getting up to so many shenanigans our first few years. Graduate school was the first time I regularly went to events with large groups of people, and some of my best memories are from these gatherings. Having people that were going through the same journey is invaluable, and I'm grateful to know that so many of these relationships will extend to our new quests after UNC.

To my Guilford friends, thank you all for making sure our semi-regular trips still happen. As life moves forward, it's difficult to arrange schedules but our beach and ski escapades have set a precedent for deep, lifelong friendships.

To my parents, thank you for setting the stage to support my trajectory. It is truly a blessing to deeply know that my dreams and ambitions are valid. You have supported my development in many ways through many stages of life and integrating that into my psyche has made all the difference. To my sister, Ellie, thank you for paying attention to who I am. Not many siblings live together for years during early adulthood, and that has cemented our bond. These past five years have been a period of intense challenge and growth for both of us, and I'm incredibly grateful that we are each a witness to the other.

TABLE OF CONTENTS

LIST OF FIGURES xi

LIST OF TABLES xiii

LIST OF ABBREVIATIONS AND SYMBOLS xiv

CHAPTER 1: INTRODUCTION 1

1.1 Motivation 1

1.2 Fluoride-Ion Batteries: History and Operation 2

1.2.1 Electrolytes 3

1.2.2 Electrodes 4

1.3 Computational Screening for Battery Materials 5

1.3.1 High-throughput Screening in Battery Research 5

1.3.2 FIB Cathode Design Space and Ternary Fluorides 7

1.3.3 Parasitic Carbon Side Reactions in FIB Composites 8

1.4 Electrides 9

1.4.1 Electride Overview 10

1.4.2 Electrides as Anion Storage Materials 11

1.4.3 Factors Controlling Electride Topology 12

1.4.4 Structural Disorder and Aperiodic Electron Topology in Ti_2C 14

1.5 Overview of Research Described in this Thesis 15

REFERENCES 17

CHAPTER 2: METHODS 28

2.1 Introduction 28

2.2 Computational Methods 28
2.2.1 High-Throughput Computational Screening of FIB Materials 28
2.2.1.1 General High-Throughput Approach 29
2.2.1.2 Electrochemical Potentials 30
2.2.1.3 DFT Energy Uncertainty 32
2.2.1.4 Ternary Cathode Screening 33
2.2.1.4.1 Identification of Defluorination Pairs 33
2.2.1.4.2 Scale Factor Correction 34
2.2.1.4.3 Interface Reaction Analysis 34
2.2.1.4.4 Calculated Properties 35
2.2.1.4.4 Data Compilation 36
2.2.2 Carbide Screening 37
2.2.3 Titanium Center Geometry in Partially Ordered Ti_2C 38
2.2.4 Other Tools Used 41
2.3 Synthetic Methods 41
2.3.1 Synthesis of $NaVF_4$ 42
2.3.1.1 Solid State Synthesis Using Metal Fluorides 43
2.3.1.2 Containment Strategy 44
2.3.1.3 Temperature Optimization 45
2.3.1.4 Mechanochemical Activation 46
2.3.1.5 Optimized Synthesis Protocol 47
2.3.2 Synthesis of Ti_2C 48
2.3.2.1 Ti_2C Procedure 1: Arc Melting 49
2.3.2.2 Ti_2C Procedure 2: Powder Mixing 50
2.3.2.3 Ti_2C Optimization Attempts 50

2.3.2.4 Synthesis of Layered Ti_2CH_2 51
2.3.2.5 Dehydrogenation of Layered Ti_2CH_2 52
2.4 Characterization Methods 52
2.4.1 Powder X-ray Diffraction and Rietveld Refinement 52
2.4.1.1 XRD Background and Theory 52
2.4.1.2 Instrument Details and Sample Preparation 53
2.4.1.3 Rietveld Refinement and Quantitative Phase Analysis in Materials Studio 55
2.4.1.3.1 The Refinement Problem 55
2.4.1.3.2 Instrument Broadening Calibration with Si Standard 57
2.4.1.3.3 Single-Phase Preliminary Refinements 58
2.4.1.3.4 Quantitative Phase Analysis 60
2.4.1.4 Materials Studio Navigation and File Management 63
REFERENCES 65
CHAPTER 3: HIGH-THROUGHPUT SCREENING OF TERNARY FLUORIDE CATHODE MATERIALS 68
3.1 Introduction 68
3.2 Results and Discussion 69
3.2.1 Screening Workflow 69
3.2.2 Final Dataset 73
3.2.3 ABF_6 Composition 75
3.2.4 Synthesis of $NaVF_4$ 76
3.3 Conclusions 78
REFERENCES 79
CHAPTER 4: CARBON ADDITIVE SIDE REACTIONS IN FIB ANODE COMPOSITES 82

4.1 Introduction 82

4.2 Results and Discussions 83

4.3 Conclusions 94

REFERENCES 97

CHAPTER 5: DISORDERED ELECTRON NETWORK IN Ti_2C 100

5.1 Introduction 100

5.2 Results and Discussion 104

5.2.1 Synthesis of Partially Ordered Ti_2C 104

5.2.2 Temperature-Dependent Model of C Ordering 106

5.2.3 Vacancy Network Connectivity 108

5.2.4 Electride Topology within Order/Disorder Regime 109

5.2.5 Tetrahedral Nodes in Network Topology 111

5.2.6 Visualizing Disorder-Induced Topological Changes in the ELF 113

5.3 Conclusion 116

REFERENCES 118

APPENDIX: SUPPORTING INFORMATION FOR CHAPTER 3 121

APPENDIX: SUPPORTING INFORMATION FOR CHAPTER 4 130

LIST OF FIGURES

Figure 2-1. Python imports for high-throughput screening projects. 29

Figure 2-2. Initial filtering step for ternary fluoride structures. 30

Figure 2-3. Calculation of voltage vs. Li/LiF for ternary fluoride materials. 32

Figure 2-4: Six-bit motif representation of C (black) configuration around Ti (red) centers. 39

Figure 2-5: 2NOTC configuration. 40

Figure 2-6. Burst quartz tube resulting from TaF_5 overpressure during $NaVF_4$ synthesis. 44

Figure 2-7. Temperature-dependent quartz tube etching. 46

Figure 2-8. XRD pattern of the optimized $NaVF_4$ synthesis 47

Figure 2-9. XRD patterns of Ti_2C phases. 49

Figure 2-10. Examples of poor two-phase Rietveld refinements for Ti_2C 56

Figure 2-11. QPA phase table in Materials Studio. 61

Figure 2-12. Results of advanced Rietveld refinement. 62

Figure 3-1: Screening workflow used to obtain the final dataset of ternary cathode material pairs 70

Figure 3-2: Interface reaction screening schematic. 72

Figure 3-3: Calculated properties for direct reaction cathode pairs. 74

Figure 4-1: Intercalation features for some carbide materials. 85

Figure 4-2. Crystal structures of several metal carbides. 86

Figure 4-3. Reaction scheme of energetics comparing the metal fluoride reduction [Eq. (1)], to the metallization coupled carbon reduction, [Eq. (2)]. 87

Figure 4-4. Impact of overpotentials in formation energetics. 90

Figure 4-5. Summary of competing formation energetics. 94

Figure 5-1. Rocksalt Ti-C system. 102

Figure 5-2. 2NOTC fraction vs. Temperature. 108

Figure 5-3. Charge/oxidation state statistics for Ti_2C..... 111

Figure 5-4. Average tetrahedral site charge vs. number of C neighbors..... 113

Figure 5-5. Impact of C displacement on ELF topology..... 115

Figure 5-6: Partially ordered Ti_2C electron network..... 116

LIST OF TABLES

Table 2-1. Quantification of ternary fluoride candidates along screening workflow 34

Table 2-2: Column titles in cathode datasets with descriptions. 37

Table 2-3. Calibrated U, V, W, values in the Materials Studio Reflex refinement window from Si standard refinement. 58

Table 3-1. Summary of experimental conditions for optimizing $NaVF_4$ synthesis 78

Table A3-1: Dataset of 168 ternary fluoride material pairs identified from high throughput screening. 129

Table A4-1. Subset of competing formation energetics identified from high throughput screening. 133

LIST OF ABBREVIATIONS AND SYMBOLS

0D	zero-dimensional
1D	one-dimensional
1NOTC	first neighbour ordered titanium center
2NOTC	second neighbour ordered titanium center
2D	two-dimensional
3D	three-dimensional
CLEASE	cluster expansion in atomic simulation environment
DFT	density functional theory
EAX	electron anion exchange
ELF	electron localization function
FIB	fluoride-ion battery
FWHM	full width at half maximum
GGA	generalized gradient approximation
LIB	lithium-ion battery
LOOCV	leave-one-out cross validation
PAW	Projector-augmented wave
PBE	Perdew–Burke-Ernzerhof
PXRD	powder x-ray diffraction
PyMatGen	Python Package for Material Genomics

Simmate	The Simulated Materials Ecosystem
VASP	Vienna ab initio software package

CHAPTER 1: INTRODUCTION

1.1 Motivation

The global transition to renewable energy, electrification of transportation, and growth of grid-scale storage are driving the demand for battery chemistries with optimized performance, safety, and cost. Lithium-ion batteries (LIBs) have dominated electrochemical energy storage for decades but face growing challenges in terms of critical mineral supplies, thermal runaway safety risks, and capacity and performance limitations. These obstacles have motivated increased investigation of battery chemistries beyond those involving lithium.[1–10]

Among cation-based alternatives, sodium-ion batteries have advanced most rapidly toward commercialization because of the global abundance of sodium precursors and their similarities to LIB electrode architectures.[11–14] Potassium-, magnesium-, zinc-, and aluminum-ion systems have also received attention, each offering distinct advantages in abundance, safety, or multivalent capacity, although each also faces challenges in electrolyte compatibility, sluggish ion diffusion, or limited cyclability.[1,15–19] A less explored alternative system uses anions rather than cations as the charge carrier.

Among anionic chemistries, fluoride-ion batteries (FIBs) are particularly compelling. Fluorine is the lightest halogen, giving it a high charge-to-mass ratio which translates to high gravimetric and volumetric energy densities. Theoretical estimates suggest that FIBs could achieve volumetric energy densities exceeding 2,000 Wh/kg, which is more than twice the value of current LIB technology. As the most electronegative element, fluorine also has wide electrochemical stability windows, thereby enabling the construction of batteries that produce large potentials. Additionally, the natural abundance of fluorine in the Earth's crust removes the geopolitical supply constraints that affect lithium. Despite these advantages, FIBs remain at an early stage of development, with several foundational questions unresolved.[20–23]

My dissertation addresses a central question in FIB research: what design rules govern the viability of FIB electrode materials, and how can they inform rational electrode development? I approach this question at three levels. At the level of composition, which ternary fluoride materials beyond simple binary metal fluorides can function as thermodynamically viable FIB cathodes? At the level of electrode composite compatibility, how can parasitic side reactions between carbon conductive additives and active electrode materials be predicted from competing formation energetics? At the level of electronic structure, how does disorder in a candidate electrode material affect the bare electron network that governs its potential for anionic storage? These questions are addressed in my dissertation work through high-throughput thermodynamic screening, targeted synthesis, and atomistic modeling in three complementary projects.

1.2 Fluoride-Ion Batteries: History and Operation

FIBs operate by shuttling fluoride anions between a cathode and an anode through a fluoride-conducting electrolyte. The cathodic and anodic reactions during discharge of a cell can generally be written as follows:

$$\text{Cathode side: } xe^- + MF_x \rightarrow M + xF^- \quad (1)$$

$$\text{Anode side: } xF^- + M' \rightarrow M'F_x + xe^- \quad (2)$$

Electrochemical cells utilizing these general reactions were first proposed and realized in the 1970s. The earliest experimental cells utilized a doped β-PbF_2 electrolyte with a Pb anode and either a CuF_2 or AgF cathode.[24–26] However, these cells suffered from poor capacities attributed to Pb anode oxidation and low ionic conductivities. Due to these challenges and the broader shift toward LIBs in the battery field after their commercial rise in the 1990s, practical progress in FIBs stalled for decades.

The field was revitalized in 2011 when Reddy and Fichtner reported the first reversible all-solid-state FIB, operating at elevated temperatures of 150–200 °C.[27] They employed several binary metal cathode materials including CuF_2, BiF_3, and SnF_2 with a Ba-doped LaF_3 electrolyte and a Ce metal anode. While these setups displayed short life cycling performance, this work established the practical realization of FIBs and increased research interest. In the following paragraphs I outline these developments.[22,23,28]

1.2.1 Electrolytes

In any battery, the electrolyte must exhibit high ionic conductivity, a large window of electrochemical stability, and low electrical conductivity to prevent self-discharge. For FIBs, the development of suitable electrolytes has been a central challenge.

Solid-state electrolytes: Most solid fluoride-ion conductors studied as FIB electrolytes belong to either the tysonite-type (i.e., LaF_3) or fluorite-type (i.e., CaF_2, PbF_2) crystal families. Tysonite-type structures are often binary fluorides with a rare earth metal and frequently require aliovalent doping to achieve sufficient ionic conductivity. In addition to the Ba-doped LaF_3 system introduced by Anji Reddy and Fichtner, other compositions such as Sr- and Ca-doped LaF_3 have been explored.[21,29,30] More recently, materials in the $MSnF_4$ (M = Pb, Ba) family have shown promising fluoride conductivities.[31–36] Sundberg et al. recently published a high-throughput computational study predicting the activation energy for fluoride diffusion in every known fluoride-containing crystal, identifying several promising new candidates for solid-state electrolytes.[37] However, achieving the ionic conductivity required for practical operation remains a standing challenge for all solid-state FIB electrolytes, which still require elevated temperatures.

Liquid electrolytes: A transformative advance came in 2018 when Davis et al. published the first liquid electrolyte for an FIB system, which was based on tetraalkylammonium fluoride salt (Np_1F) dissolved in a dry fluorinated ether solvent (bis(2,2,2-trifluoroethyl) ether, BTFE).[38] This

electrolyte achieved a room-temperature ionic conductivity of 7.95 mS cm^{-1} and an electrochemical stability window of 4.1 V. The discovery of a liquid electrolyte was ground-breaking because it enabled FIB operation at room temperature and facilitated the study of many new liquid and polymer-based electrolytes such as organic fluorides in ionic liquids, ammonium bifluoride-doped PEG, and CsF salts in organic solvents.[39–42]

1.2.2 Electrodes

FIB electrode materials can be broadly divided into conversion- and intercalation-based systems. Conversion electrodes remain the dominant class in the FIB literature, particularly for cathodes, because they can access high theoretical capacities through complete fluorination and defluorination reactions. Common conversion cathodes include CuF_2 and BiF_3, with additional examples including SnF_2, Cu_2O, BiF_3/BaF_2 solid solution, and AgF_2.[27,43–53] Commonly studied conversion anodes include CeF_2, MgF_2, CaF_2, and ZnF_2.[27,45,54–56] SnF_2 and PbF_2 have been used as both cathode and anode materials because of their intermediate potentials (Pb/PbF_2 is 2.26 V vs Li/LiF).[27,50,55,57–61] These systems are attractive because of their high theoretical energy densities; for example, CuF_2 and BiF_3 provide theoretical cathode capacities of 528 mAh g^{-1} and 302 mAh g^{-1}, respectively, while MgF_2 provides a theoretical anode-side gravimetric capacity of approximately 865 mAh g^{-1}. However, conversion reactions require repeated breaking and reforming of chemical bonds, which results in large activation energies and often large volume changes during cycling. The resulting structural disruption, particle cracking, loss of electrical contact, and voltage hysteresis are major causes of rapid capacity fade and limited cycle life in practical FIB cells.[20–23]

Intercalation-based electrodes offer an alternative strategy in which fluoride ions are inserted into and removed from a host structure while largely preserving the framework of the active material. This approach has attracted increasing attention because it may reduce the mechanical penalties associated with full conversion reactions and improve cyclability. On the

cathode side, early attempts at fluoride intercalation in $YBa_2Cu_3O_{7-x}$ and La_2CuO_4 showed little reversibility.[62,63] A breakthrough came in 2017 with the first demonstration of reversible electrochemical fluoride intercalation in the Ruddlesden–Popper phase $LaSrMnO_4$.[57] This proof of principle motivated broader study of Ruddlesden–Popper-type oxides and oxyfluorides such as La_2CoO_4 and La_2NiO_4, which offer improved structural retention and cycle life.[54,55,57,59,60,64–67] The major challenge of intercalation-based materials is their low gravimetric capacity, typically on the order of 16-70 mAh g^{-1} vs 180-320 mAh g^{-1} for conversion-based materials at the first discharge. On the anode side, intercalation chemistry remains less developed, but electride-based materials such as Y_2C and Sc_2C have recently been discussed as promising next-generation intercalation anodes because they enable fluoride storage via the electron-anion exchange mechanism described later.[68–72]

Despite this progress since 2011, practical FIB electrodes continue to suffer from limitations in electrical and ionic conductivity, volume expansion during cycling, and capacity retention. Progress in identifying new high-performance electrode materials has been slow in part because limited methods exist for assessing material suitability before committing significant experimental time and resources.

1.3 Computational Screening for Battery Materials

1.3.1 High-throughput Screening in Battery Research

The discovery of new electrode materials has historically proceeded through intuition-guided synthesis and characterization, a process that is slow, expensive, and poorly suited to navigating large compositional spaces. Over the past fifteen years, high-throughput computational screening has emerged as a powerful complement to this experimental approach. This paradigm relies on large-scale material databases, particularly the Materials Project,[73] the Open Quantum Materials Database (OQMD),[74] and the Inorganic Crystal Structure Database (ICSD),[75] which provide density functional theory (DFT)-computed thermodynamic

properties for hundreds of thousands of inorganic compounds. By applying sequential computational filters to these databases, researchers can rapidly narrow vast candidate pools to manageable sets of promising materials for experimental follow-up.

For LIBs, this approach has been applied to nearly every component of the electrochemical cell. Hautier et al. demonstrated one of the first high-throughput screenings for novel LIB cathode materials, identifying mixed polyanion compositions as promising candidates.[76] Kirklin, Meredig, and Wolverton extended the approach to LIB anode materials, screening thousands of candidates through sequential filters on thermodynamic stability, voltage, capacity, and volume change upon cycling.[77] Aykol et al. screened more than 130,000 oxygen-bearing compounds to identify cathode coatings that suppress degradation in LIBs by evaluating thermodynamic stability, electrochemical stability, and chemical compatibility.[78] Xiao et al. extended this framework to solid-state battery cathode coatings, screening for thermodynamic and electrochemical stability at the cathode/electrolyte interface.[79] Solid electrolyte discovery has similarly benefited from automated screening workflows, with Kahle et al. using the AiiDA framework to screen over 1,300 Li-containing structures through sequential filters on electronic conductivity and ionic diffusivity.[80]

These methods have also been extended beyond lithium chemistries. Zhang et al. developed a screening method for layered Na-ion cathode materials[81] and other multivalent-ion (Mg^{2+}, Zn^{2+}, Ca^{2+}, Al^{3+}) battery cathodes using thermodynamic stability, voltage, and volume change.[82] Liu et al. investigated fluoride materials, but these were still aimed at LIB cathode coating applications.[83] Gschwind et al. conducted the only prior anion-battery screening study in which binary chlorides were evaluated for energy density and toxicity.[84]

Despite the use of these methods for LIBs and some beyond-Li systems, no high-throughput thermodynamic screening has been applied to FIB electrode materials. This gap is significant for three reasons: (1) the viable material classes for FIB electrodes remain largely

unknown, (2) the thermodynamic stability of cathode candidates under cycling conditions has not been systematically assessed, and (3) the compatibility of practical electrode composites is poorly understood. Without this foundation, the field lacks a principled basis for narrowing the fluoride compositional space or prioritizing materials for experimental investigation. The following two sections examine these limitations, focusing on cathode discovery and electrode composite side reactions addressed by the computational screening described in later chapters.

1.3.2 FIB Cathode Design Space and Ternary Fluorides

In contrast to LIBs, which have benefited from decades of intensive electrode optimization, FIBs still have an underdeveloped cathode material landscape. Exploration has been limited to a few dozen candidates, and the field has focused primarily on a small number of binary metal fluorides. BiF_3 has received the most attention, offering a theoretical capacity of 302 mAh/g at ~2.2 V vs. Ce and was one of the first cathodes to demonstrate repeated cycling in all-solid-state cells.[27,29,54,85–91] However, even the best BiF_3-based cells still give only ~80-190 mAh/g at first discharge and exhibit rapid capacity fading, often decreasing to ~50 mAh/g by cycle 40. Additionally, BiF3 often requires large overpotentials for reliable operation. CuF_2 is another common cathode material because of its high theoretical gravimetric capacity of ~528 mAh/g at ~2.5 V vs. Ce.[27,38,50,51,53,92–98] Although CuF_2 offers higher first discharge capacities than BiF_3 (~208-410 mAh/g) the practical reversibility of CuF_2 has also been poor, with studies reporting that the capacity decreases to ~20-200 mAh/g after 10 cycles. More limited work has been conducted on PbF_2,[99] SnF_2,[27] FeF_3,[100] CoF_2, NiF_2,[101] and AgF_2[89] with similar trends observed. More broadly, binary conversion fluorides suffer from a common set of structural limitations including high activation energies associated with bond breaking during defluorination, large volume changes that disrupt contact between the active material, electrode additives, and solid electrolytes and significant polarization or overpotential during cycling.[20–23] These problems are compounded by the fact that many of the foundational solid-state FIB

demonstrations required operation near 150–170 °C to obtain adequate fluoride-ion transport, underscoring that cathode performance has often been constrained not only by the active material itself but also by slow fluoride mobility and composite-level transport losses.

Beyond binary metal fluoride compositions, a small number of ternary fluoride cathodes have been evaluated, primarily within the Ruddlesden–Popper family.[54,55,57,59–61,66,67] La_2NiO_4 has shown the most promise, sustaining reversible fluoride intercalation over more than 220 cycles with relatively stable capacity, while La_2CoO_4 and $La_{1.3}Sr_{1.7}Mn_2O_7$ exhibit capacity fading within 40–50 cycles. Fluorinated analogs such as $La_2NiO_3F_2$ and perovskite-derived hosts including $BaFeO_{2.5}$ and $Mg_{0.5}Fe_{0.5}Sb_2O_4$ have also been explored. The primary trade-off of increased cycling stability in intercalation cathode is low capacities, ranging from ~3-55 mAh/g in the materials above.

These results hint at the broader potential of ternary compositions, which might offer a richer landscape of conductivity, structural stability, and cycling performance than binary fluorides. However, moving beyond binaries fluorides introduces a combinatorial explosion in candidate compositions, and because experimentally synthesizing and electrochemically characterizing even a single candidate requires significant effort, most of this space remains unexplored. Systematic, data-driven screening of this design space is a natural next step, and one that has not yet been attempted. Chapter 3 addresses this gap through a high-throughput computational screening of ternary fluoride cathode candidates.

1.3.3 Parasitic Carbon Side Reactions in FIB Composites

Beyond identifying viable cathode compositions, practical FIB electrode design must also address compatibility between active materials and other components necessary for full battery operation. Carbon conductive additives are ubiquitous in battery electrode composites, including lithium-ion batteries, due to electronic resistance in pure active materials. Without conductive additives, effective electrochemical cycling is severely limited.[102–106] These carbon

additives are conventionally treated as electrochemically inert, but recent experimental studies have revealed evidence of carbon reduction during FIB charging. One proposed model for these observations is parasitic side reactions between carbon and active material metals, which may be partly responsible for the poor reversibility observed in some FIB configurations.[55,59,107,108]

The thermodynamic driver for these side reactions is predicted to be a competition between metal carbide and metal fluoride formation energetics. When metal carbide formation is more thermodynamically favorable than the reduction of a metal fluoride to its metal, carbon additives can be consumed. This problem is similar to the coating compatibility screening performed by Aykol et al.[78] and Xiao et al.[79] for LIBs, which evaluated competing thermodynamic driving forces at electrode/electrolyte interfaces. Because conductive additives cannot simply be removed from electrode composites, the key question is whether the thermodynamic driving forces behind carbon side reactions are predictable enough to screen for compatible metal fluoride pairings computationally. No systematic comparison of these competing reaction thermodynamics has been attempted across a broad chemical space. Chapter 4 addresses this gap through a targeted thermodynamic analysis of carbon additive side reactions in FIB electrode composites.

1.4 Electrides

While systematic evaluation of fluoride-ion battery (FIB) electrodes remains an open challenge, electrides have emerged as one class of candidate electrode materials.[23,71,72,109] Electrides are promising fluoride-ion battery anodes because their excess anionic electrons make them unusually electron-rich, able to operate at low potentials, and capable of maximizing full-cell voltage when paired with higher-potential cathodes. Many also adopt layered structures, and their diffuse, highly polarizable electron clouds may help maintain electrostatic stability in the host lattice upon fluorination/defluorination. Here, I give a background on electrides to help understand how design rules for electrides can inform viable electrode design for FIBs.

1.4.1 Electride Overview

Electrides are materials with bare electrons in crystallographic lattice sites, giving rise to unique electronic topologies with applications in catalysis, electron emission, and energy storage.[110–115] These crystalline materials are the solid-state realization of an older chemical idea that electrons can exist as discrete anionic species when confined within a suitable environment.[116] Early examples include solvated electrons in alkali metal–ammonia solutions and F-centers in alkali halides, both of which involve electrons trapped in spatially defined regions and exhibiting anion-like behavior.[110,111] The first crystalline electrides were synthesized by Dye and co-workers in the 1980s using crown ether and cryptand complexes to isolate alkali cations and force valence electrons into interstitial sites.[117–119] These organic electrides were critical proof-of-concept materials, but their limited thermal and chemical stability restricted their practical utility.

The field changed substantially with the development of inorganic electrides, which offered greater structural robustness. A major early breakthrough was Hosono and co-workers' demonstration that mayenite, $C_{12}A_7{:}e^-$, could serve as a room-temperature-stable inorganic electride, establishing that bare electrons could be stabilized in an oxide cage framework rather than only in fragile molecular crystals. Layered nitrides such as Ca_2N, Sr_2N, and Ba_2N had long been recognized as chemically unusual, but their identification as electrides became established after structural and electronic studies clarified that the excess charge resides in the interlayer space rather than in hidden hydride defects.[120–122] This was followed by Y_2C, the first transition-metal-containing 2D electride, showing that interstitial anionic electrons can coexist with metal-derived d states.[70] More recently, Sc_2C was identified as the first semiconducting 2D electride, demonstrating that electride behavior is not limited to metallic hosts and that the boundary between electride and non-electride electronic structures can be compositionally tuned.[123] High-throughput studies have since greatly expanded the predicted electride landscape, identifying

many candidate compounds, including transition-metal-containing and magnetic electrides.[124–126] More recent studies have provided a more quantitative framework for identifying electride sites, counting interstitial electrons, and assessing electride dimensionality, discussed further in following sections.[55,59,107,127,128]

1.4.2 Electrides as Anion Storage Materials

The relevance of electrides to FIBs follows from their unusual electronic properties. In conventional intercalation electrodes, charge compensation usually proceeds through ion insertion coupled with host-lattice redox. Electrides introduce a different possibility in which the bare electron can participate as the exchangeable charge species. This idea is captured in the electron–anion exchange (EAX) mechanism, where an incoming anion replaces the electride electron while the host framework is largely preserved.[72] From an electrochemical perspective, this is significant because it suggests a route to fluoride storage that does not rely on transition-metal redox dynamics or full conversion reactions, both of which often create severe kinetic and reversibility limitations in FIB systems.

This mechanism has made electrides especially compelling as candidate FIB anodes. First-principles studies proposed layered electrides as fluoride insertion hosts and predicted that fluorination could occur through EAX. More recently, Y_2C has been experimentally examined as an FIB anode, providing direct evidence that electride hosts can participate in reversible fluorination and defluorination chemistry.[71] Sc_2C has likewise been proposed as a relevant rocksalt-derived electride for fluoride storage, with the added conceptual interest that its semiconducting character reflects stronger hybridization between the cation framework and the interstitial electron states.[123] However, both materials contain expensive rare-earth elements, which limits their practical scalability as FIB anodes and motivates the search for more abundant alternatives.

Insight into how diffuse electron density can assist fluoride transport also comes from fluoride-ion conductors containing stereochemically active lone-pair cations such as Sn and Pb. In these materials, the nonbonding electron pair is not inert. Rather, its polarizability helps distort the local fluoride environment, promote anion disorder, and reduce the energetic barriers for fluoride movement. BaSnF4, for example, has long been recognized as an unusually good fluoride conductor, and recent work has shown that dynamic Sn lone pairs help destabilize specific fluoride sites and generate local disorder within an average fluorite-like framework.[129–131] Related Pb-based studies similarly show that lone-pair electron density can flatten the fluoride migration potential and stabilize transient hopping environments.[132] These observations are conceptually relevant to electrides because EAX likewise involves direct interaction between incoming fluoride and electronically soft, weakly bound electron density. More broadly, they suggest that the spatial distribution, connectivity, and polarizability of non-nuclear electron density may be central to fluoride transport, thereby motivating a deeper examination of the structural and electronic factors that control electride topology in candidate FIB anodes.

1.4.3 Factors Controlling Electride Topology

Electrides are conventionally classified by the dimensionality of their anionic electron network, where bare electrons may occupy isolated cages (0D), channels (1D), planes (2D), or fully connected networks (3D).[110,112,114,128] A central finding from the electride literature is that this localized electron topology can be tuned on the basis of composition, structure, and local environment. Prior work on rocksalt metal carbides shows that electride character can be progressively destabilized by changes in composition, particularly cation electronegativity. Along the series $Y_2C \rightarrow Sc_2C \rightarrow Al_2C$, increasing electronegativity drives stronger hybridization between cation states and the interstitial electron density. Sc_2C represents an intermediate case, retaining electride character but becoming semiconducting, whereas in Al_2C this hybridization becomes strong enough that the electrons are no longer localized in distinct lattice

sites. This progression highlights cation identity as a key control on whether electride electrons persist or are absorbed back into conventional bonding.[70,123]

Structural perturbations also reshape electride topology. In Y_2C, for example, applied pressure has been shown to tune spin alignment and the electronic behavior of the bare electrons, demonstrating that even subtle lattice changes can alter the properties of the electride electron layer.[133] In Ca_2N, pressure drives a metal-to-semiconductor transition accompanied by a reduction in topology from a 2D layered state toward more localized 0D character.[134] Similar sensitivity appears in the local chemical environment. Surface oxidation and passivation can strongly modify or suppress electride behavior,[135,136] while functionalization studies show that replacing interstitial electrons with conventional anions transforms the electronic character of electride-derived materials.[137] Some compositional modification can even strengthen electride behavior. Li et al., for example, showed that the electron-deficient compound Ca_5Pb_3 can be transformed into an electride under pressure or by Hf substitution, expanding the chemical space of electride formation beyond the usual electron-rich hosts.[138]

These studies show that electride character is best understood as a tunable electronic state. Composition, pressure, surface chemistry, and substitution all influence bare electron localization properties. However, substantial structural disorder in electrides remains comparatively underexplored. Although prior studies make clear that electride behavior can evolve under compositional and structural perturbation, much less is known about what happens when crystallographic periodicity is significantly disrupted. This question is especially important regarding dimensionality, because disordered precedents are limited to localized or low-dimensional electron confinement rather than higher dimensional (especially 3D) networks.

The simplest precedent of disorder in electride-like systems is the F-center in alkali halides and metal oxides, where a single electron is trapped at an isolated anion vacancy with no connectivity between sites.[139] A more developed but still local example comes from

mayenite: Kim, Shimoyama, and Hosono showed that the characteristic 0D electride cage survives melt-quenching into an amorphous host, indicating that local electron-trapping motifs can persist even after long-range order is lost.[140] Complementary computational studies by Akola et al. and Johnson et al. supported this interpretation in $CaO–Al_2O_3$ glasses, linking disordered glass topology to the persistence of localized electron-hosting cavities.[141,142] Related studies in known or candidate electrides further show that disorder can create local electride-like features without generating an extended network. Yang et al. and Chae et al., for example, found that vacancies at low concentration in CeO and Ca_2N can produce localized bare electrons or perturb nearby electride sites, but these effects remain isolated and vacancy-centered rather than globally connected.[143,144] Ahmed et al. likewise demonstrated that electride-like behavior beyond 0D can emerge in Si and in alkali or alkaline earth elements under high pressure, but these electron features arise from compression and melting rather than from a disordered vacancy-network topology in the solid state, and they do not establish a continuous interstitial network.[145]

These precedents confirm that localized, 0D electride-like character can survive disorder, but none have examined whether a connected 3D electron network can do the same. That unresolved question extends beyond any single material and motivates the final project of this dissertation, which investigates whether 3D electride connectivity can persist when long-range crystallographic periodicity is substantially lost.

1.4.4 Structural Disorder and Aperiodic Electron Topology in Ti_2C

Materials with partially occupied anion sublattices are natural candidates for investigating disorder-tolerant, high-dimensional electride-like behavior, since a connected 3D electron network requires a high concentration of accessible interstitial or vacancy sites. Titanium carbide is one such material, adopting a disordered rocksalt structure across a wide range of carbon stoichiometries, with carbon atoms and vacancies randomly distributed over the

anion sublattice against a fully occupied Ti framework.[146] At the Ti_2C composition, the thermodynamically predicted ground state is the ordered Fd-3m phase, in which carbon vacancies arrange into a fully connected three-dimensional network that qualifies as a 3D electride under the dimensionality framework of Weaver et al.[128] Experimentally, however, both fully and partially disordered carbon sublattices are commonly observed,[147–150] leaving unresolved whether 3D electride-like connectivity can persist when the ideal vacancy network is substantially disrupted.

Understanding whether this electride topology persists under substantial disorder is important for evaluating whether disordered Ti_2C can retain the diffuse, polarizable electron density that makes electrides attractive for fluoride storage. In that sense, the question parallels the Sn/Pb lone-pair-assisted fluoride conductors discussed earlier, where electronically soft, non-nuclear electron density helps distort local anion environments and facilitate fluoride motion. This gap motivates the work described in Chapter 5, which examines how carbon sublattice disorder reshapes the interstitial electron network in Ti_2C and whether a connected 3D electride-like topology can survive without perfect crystallinity. These results establish a foundation for understanding how disorder influences electride-like electronic character in materials relevant to FIB electrode design.

1.5 Overview of Research Described in this Thesis

Given the gaps in knowledge described in the above sections, my dissertation investigates fundamental design rules for FIB electrodes through three projects.

First, I expand the FIB cathode design space through a high-throughput thermodynamic screening of more than 5,000 ternary fluoride materials in the Materials Project database. I establish a generalizable workflow for identifying cathode charge/discharge pairs and assessing thermodynamic resistance to decomposition during cell cycling. This screening identifies the ABF_6 compositional family as a promising material class. I then connect the computational

predictions to experimental results by optimizing a low-cost synthesis route for $NaVF_4$ as a prototype cathode material.

Next, I adapt this screening framework to address parasitic carbon side reactions in FIB electrode composites. By evaluating the competing thermodynamics of 930 unique metal fluoride and metal carbide formation reactions, I derive composition-dependent design rules illustrating that carbon additives are generally resilient when paired with late transition metals and vulnerable to degradation with alkali, alkaline earth, and early transition metals. These design rules transform carbon compatibility from an empirical unknown into a predictable parameter and provide a thermodynamic basis that can be extended to other additive and active material combinations.

Finally, I investigate structural and electronic disorder in rocksalt Ti_2C. Using cluster expansion, Monte Carlo simulations, and BadELF analysis, I show that the fully ordered ground state of Ti_2C is experimentally inaccessible because of competing thermodynamic and kinetic driving forces. I then demonstrate that the 3D electron topology remains robust across a wide range of carbon sublattice configurations, constituting the first computational evidence for a disordered three-dimensional electron network.

Across these three projects, my dissertation develops design rules for evaluating FIB electrodes across composition, composite compatibility, and electronic structure. I first create a methodology to narrow the ternary fluoride design space for new cathode materials, and then adapt that framework to predict parasitic side reactions between carbon conductive additives and active electrode materials. Finally, I examine how structural disorder reshapes the electron network in Ti_2C, a candidate FIB anode. Taken together, these studies move FIB development toward transferable principles for electrode discovery and characterization.

REFERENCES

(1) Gourley, S. W. D.; Brown, R.; Adams, B. D.; Higgins, D. Zinc-Ion Batteries for Stationary Energy Storage. *Joule*. Cell Press July 19, 2023, pp 1415–1436. https://doi.org/10.1016/j.joule.2023.06.007.

(2) Tian, Y.; Zeng, G.; Rutt, A.; Shi, T.; Kim, H.; Wang, J.; Koettgen, J.; Sun, Y.; Ouyang, B.; Chen, T.; Lun, Z.; Rong, Z.; Persson, K.; Ceder, G. Promises and Challenges of Next-Generation "beyond Li-Ion" Batteries for Electric Vehicles and Grid Decarbonization. *Chemical Reviews*. American Chemical Society February 10, 2021, pp 1623–1669. https://doi.org/10.1021/acs.chemrev.0c00767.

(3) Fichtner, M.; Edström, K.; Ayerbe, E.; Berecibar, M.; Bhowmik, A.; Castelli, I. E.; Clark, S.; Dominko, R.; Erakca, M.; Franco, A. A.; Grimaud, A.; Horstmann, B.; Latz, A.; Lorrmann, H.; Meeus, M.; Narayan, R.; Pammer, F.; Ruhland, J.; Stein, H.; Vegge, T.; Weil, M. Rechargeable Batteries of the Future—The State of the Art from a BATTERY 2030+ Perspective. *Advanced Energy Materials*. John Wiley and Sons Inc May 1, 2022. https://doi.org/10.1002/aenm.202102904.

(4) Feng, X.; Ouyang, M.; Liu, X.; Lu, L.; Xia, Y.; He, X. Thermal Runaway Mechanism of Lithium Ion Battery for Electric Vehicles: A Review. *Energy Storage Materials*. Elsevier B.V. January 1, 2018, pp 246–267. https://doi.org/10.1016/j.ensm.2017.05.013.

(5) Lebrouhi, B. E.; Baghi, S.; Lamrani, B.; Schall, E.; Kousksou, T. *Critical Materials for Electrical Energy Storage: Li-Ion Batteries*; 2022.

(6) Frith, J. T.; Lacey, M. J.; Ulissi, U. A Non-Academic Perspective on the Future of Lithium-Based Batteries. *Nature Communications*. Nature Research December 1, 2023. https://doi.org/10.1038/s41467-023-35933-2.

(7) Grey, C. P.; Hall, D. S. Prospects for Lithium-Ion Batteries and beyond—a 2030 Vision. *Nature Communications*. Nature Research December 1, 2020. https://doi.org/10.1038/s41467-020-19991-4.

(8) Zhang, Q.; Yan, J.; Gao, H. O.; You, F. A Systematic Review on Power Systems Planning and Operations Management with Grid Integration of Transportation Electrification at Scale. *Advances in Applied Energy*. Elsevier Ltd September 1, 2023. https://doi.org/10.1016/j.adapen.2023.100147.

(9) Zhao, C.; Andersen, P. B.; Træholt, C.; Hashemi, S. Grid-Connected Battery Energy Storage System: A Review on Application and Integration. *Renewable and Sustainable Energy Reviews*. Elsevier Ltd August 1, 2023. https://doi.org/10.1016/j.rser.2023.113400.

(10) Dunn, B.; Kamath, H.; Tarascon, J.-M. *Electrical Energy Storage for the Grid: A Battery of Choices*; 2011; Vol. 334. https://about.jstor.org/terms.

(11) Christoph Vaalma; Daniel Buchholz; Marcel Weil; Stefano Passerini. *A Cost and Resource Analysis Of-Ion Batteries*; 2018. https://doi.org/https://doi.org/10.1038/natrevmats.2018.13.

(12) Rudola, A.; Rennie, A. J. R.; Heap, R.; Meysami, S. S.; Lowbridge, A.; Mazzali, F.; Sayers, R.; Wright, C. J.; Barker, J. Commercialisation of High Energy Density Sodium-Ion Batteries: Faradion's Journey and Outlook. *Journal of Materials Chemistry A*. Royal Society of Chemistry April 7, 2021, pp 8279–8302. https://doi.org/10.1039/d1ta00376c.

(13) Yao, A.; Benson, S. M.; Chueh, W. C. Critically Assessing Sodium-Ion Technology Roadmaps and Scenarios for Techno-Economic Competitiveness against Lithium-Ion Batteries. *Nat. Energy* **2025**, *10* (3), 404–416. https://doi.org/10.1038/s41560-024-01701-9.

(14) Yadav, P.; Shelke, V.; Patrike, A.; Shelke, M. Sodium-Based Batteries: Development, Commercialization Journey and New Emerging Chemistries. *Oxford Open Materials Science*. Oxford University Press 2023. https://doi.org/10.1093/oxfmat/itac019.

(15) Zhang, W.; Liu, Y.; Guo, Z. Approaching High-Performance Potassium-Ion Batteries via Advanced Design Strategies and Engineering; 2019; Vol. 5. https://www.science.org.

(16) Zhang, W.; Lu, J.; Guo, Z. Challenges and Future Perspectives on Sodium and Potassium Ion Batteries for Grid-Scale Energy Storage; 2021.

(17) Guo, J.; Schaefer, J. L.; Shao, Y. Rechargeable Multivalent-Ion Batteries. *Energy Material Advances*. American Association for the Advancement of Science January 1, 2024. https://doi.org/10.34133/energymatadv.0112.

(18) Canepa, P.; Sai Gautam, G.; Hannah, D. C.; Malik, R.; Liu, M.; Gallagher, K. G.; Persson, K. A.; Ceder, G. Odyssey of Multivalent Cathode Materials: Open Questions and Future Challenges. *Chem. Rev.* **2017**, *117* (5), 4287–4341. https://doi.org/10.1021/acs.chemrev.6b00614.

(19) Fang, G.; Zhou, J.; Pan, A.; Liang, S. Recent Advances in Aqueous Zinc-Ion Batteries. *ACS Energy Lett.* **2018**, *3* (10), 2480–2501. https://doi.org/10.1021/acsenergylett.8b01426.

(20) Gschwind, F.; Rodriguez-Garcia, G.; Sandbeck, D. J. S.; Gross, A.; Weil, M.; Fichtner, M.; Hörmann, N. Fluoride Ion Batteries: Theoretical Performance, Safety, Toxicity, and a Combinatorial Screening of New Electrodes. *J. Fluor. Chem.* **2016**, *182*, 76–90. https://doi.org/10.1016/j.jfluchem.2015.12.002.

(21) Nowroozi, M. A.; Mohammad, I.; Molaiyan, P.; Wissel, K.; Munnangi, A. R.; Clemens, O. Fluoride Ion Batteries - Past, Present, and Future. *Journal of Materials Chemistry A*. Royal Society of Chemistry 2021, pp 5980–6012. https://doi.org/10.1039/d0ta11656d.

(22) Liu, E.; Duan, Y.; Li, Y.; Peng, C.; Feng, W. Fluoride-Ion Batteries: A Review of Recent Advances and Future Opportunities. *Electrochemical Energy Reviews* **2025**, *8* (1), 28. https://doi.org/10.1007/s41918-025-00268-7.

(23) Xiao, A. W.; Galatolo, G.; Pasta, M. The Case for Fluoride-Ion Batteries. *Joule* **2021**, *5* (11), 2823–2844. https://doi.org/10.1016/j.joule.2021.09.016.

(24) Sokolov, . U S; Crosby, L. J. A Solid-State Galvanic Cell with Fluoride-Conducting Electrolytes; 1976; Vol. 121.

(25) Danto, Y.; Poujade, G.; Pistrt~, J. D.; Lucat, C.; Salardenne, J. *A Pb[PbF2[BiF31Bi THIN SOLID FILM REVERSIBLE GALVANIC CELL*; 1978; Vol. 55.

(26) Kennedy, J. H.; Hunter, J. C. *Thin-Film Galvanic Cell Pb/Pb2 CuF2/Cu*; 1976. https://doi.org/10.1149/1.2132740.

(27) Anji Reddy, M.; Fichtner, M. Batteries Based on Fluoride Shuttle. *J. Mater. Chem.* **2011**, *21* (43), 17059–17062. https://doi.org/10.1039/c1jm13535j.

(28) Nowroozi, M. A.; Mohammad, I.; Molaiyan, P.; Wissel, K.; Munnangi, A. R.; Clemens, O. Fluoride Ion Batteries - Past, Present, and Future. *Journal of Materials Chemistry A*. 2021, pp 5980–6012. https://doi.org/10.1039/d0ta11656d.

(29) Rongeat, C.; Reddy, M. A.; Witter, R.; Fichtner, M. Nanostructured Fluorite-Type Fluorides as Electrolytes for Fluoride Ion Batteries. *Journal of Physical Chemistry C* **2013**, *117* (10), 4943–4950. https://doi.org/10.1021/jp3117825.

(30) Fujara, F.; Kruk, D.; Lips, O.; Privalov, A. F.; Sinitsyn, V.; Stork, H. Fluorine Dynamics in LaF3-Type Fast Ionic Conductors - Combined Results of NMR and Conductivity Techniques. *Solid State Ion.* **2008**, *179* (40), 2350–2357. https://doi.org/10.1016/j.ssi.2008.10.003.

(31) Chaudhuri, S.; Wang, F.; Grey, C. P. Resolving the Different Dynamics of the Fluorine Sublattices in the Anionic Conductor BaSnF4 by Using High-Resolution MAS NMR Techniques. *J. Am. Chem. Soc.* **2002**, *124* (39), 11746–11757. https://doi.org/10.1021/ja026155j.

(32) Preishuber-Pflügl, F.; Epp, V.; Nakhal, S.; Lerch, M.; Wilkening, M. Defect-Enhanced F-Ion Conductivity in Layer-Structured Nanocrystalline BaSnF4 Prepared by High-Energy Ball Milling Combined with Soft Annealing. *Physica Status Solidi (C) Current Topics in Solid State Physics* **2015**, *12* (1–2), 10–14. https://doi.org/10.1002/pssc.201400193.

(33) N. I. Sorokin. SnF 2 -Based Solid Electrolytes. **2004**.

(34) Molaiyan, P. Solid-State Electrolytes for Fluoride-Ion Batteries; 2019.

(35) Murakami, M.; Morita, Y.; Yonemura, M.; Shimoda, K.; Mori, M.; Koyama, Y.; Kawaguchi, T.; Fukuda, K.; Ishikawa, Y.; Kamiyama, T.; Uchimoto, Y.; Ogumi, Z. High Anionic Conductive Form of PbxSn2-XF4. *Chemistry of Materials* **2019**, *31* (18), 7704–7710. https://doi.org/10.1021/acs.chemmater.9b02623.

(36) Trnovcová, V.; Fedorov, P. P.; Furár, I. *Fluoride Solid Electrolytes Containing Rare Earth Elements*; 2008; Vol. 26.

(37) Sundberg, J. D.; Druffel, D. L.; McRae, L. M.; Lanetti, M. G.; Pawlik, J. T.; Warren, S. C. High-Throughput Discovery of Fluoride-Ion Conductors via a Decoupled, Dynamic, and Iterative (DDI) Framework. *NPJ Comput. Mater.* **2022**, *8* (1). https://doi.org/10.1038/s41524-022-00786-8.

(38) Davis, V. K.; Bates, C. M.; Omichi, K.; Savoie, B. M.; Momčilović, N.; Xu, Q.; Wolf, W. J.; Webb, M. A.; Billings, K. J.; Chou, N. H.; Alayoglu, S.; McKenney, R. K.; Darolles, I. M.; Nair, N. G.; Hightower, A.; Rosenberg, D.; Ahmed, M.; Brooks, C. J.; Miller, T. F.; Grubbs, R. H.; Jones, S. C. Room-Temperature Cycling of Metal Fluoride Electrodes: Liquid Electrolytes for High-Energy Fluoride Ion Cells. *Science (1979).* **2018**, *362* (6419), 1144–1148. https://doi.org/10.1126/science.aat7070.

(39) Alshangiti, O.; Galatolo, G.; Rees, G. J.; Guo, H.; Quirk, J. A.; Dawson, J. A.; Pasta, M. Solvent-in-Salt Electrolytes for Fluoride Ion Batteries. *ACS Energy Lett.* **2023**, *8* (6), 2668–2673. https://doi.org/10.1021/acsenergylett.3c00493.

(40) Gschwind, F.; Zao-Karger, Z.; Fichtner, M. A Fluoride-Doped PEG Matrix as an Electrolyte for Anion Transportation in a Roomerature Fluoride Ion Battery. *J. Mater. Chem. A Mater.* **2014**, *2* (5), 1214–1218. https://doi.org/10.1039/c3ta13881j.

(41) Gschwind, F.; Bastien, J. Parametric Investigation of Room-Temperature Fluoride-Ion Batteries: Assessment of Electrolytes, Mg-Based Anodes, and BiF3-Cathodes. *J. Mater. Chem. A Mater.* **2015**, *3* (10), 5628–5634. https://doi.org/10.1039/c4ta06625a.

(42) Konishi, H.; Minato, T.; Abe, T.; Ogumi, Z. Electrochemical Performance of a Bismuth Fluoride Electrode in a Reserve-Type Fluoride Shuttle Battery. *J. Electrochem. Soc.* **2017**, *164* (14), A3702–A3708. https://doi.org/10.1149/2.0931714jes.

(43) Konishi, H.; Minato, T.; Abe, T.; Ogumi, Z. Electrochemical Performance of BiF3-BaF2 Solid Solution with Three Different Phases on a Fluoride Shuttle Battery System. *ChemistrySelect* **2020**, *5* (16), 4943–4946. https://doi.org/10.1002/slct.202000713.

(44) Takami, T.; Saito, T.; Kamiyama, T.; Kawahara, K.; Fukunaga, T.; Abe, T. A New Bi0.7Fe1.3O1.5F1.7phase: Crystal Structure, Magnetic Properties, and Cathode Performance in Fluoride-Ion Batteries. *APL Mater.* **2020**, *8* (5). https://doi.org/10.1063/5.0005817.

(45) Zhang, L.; Reddy, M. A.; Fichtner, M. Electrochemical Performance of All Solid-State Fluoride-Ion Batteries Based on Thin-Film Electrolyte Using Alternative Conductive Additives and Anodes. *Journal of Solid State Electrochemistry* **2018**, *22* (4), 997–1006. https://doi.org/10.1007/s10008-017-3838-2.

(46) Cao, Z.; Yamamoto, K.; Zhang, D.; Matsunaga, T.; Kumar, M.; Thakur, N.; Watanabe, T.; Miki, H.; Iba, H.; Amezawa, K.; Uchimoto, Y. High-Performance Copper/Copper Oxide-Based Cathode Prepared by a Facile Ball-Milling Method for All-Solid-State Fluoride-Ion Batteries. *ACS Appl. Energy Mater.* **2023**, *6* (23), 11906–11914. https://doi.org/10.1021/acsaem.3c02003.

(47) Molaiyan, P.; Witter, R. Mechanochemical Synthesis of Solid-State Electrolyte Sm 1−x Ca x F 3−x for Batteries and Other Electrochemical Devices. *Mater. Lett.* **2019**, *244*, 22–26. https://doi.org/10.1016/j.matlet.2019.02.034.

(48) Molaiyan, P.; Witter, R. Crystal Phase and Surface Defect Driven Synthesis of Pb1−xSnxF2 Solid Solution Electrolyte for Fluoride Ion Batteries. *Journal of Electroanalytical Chemistry* **2019**, *845*, 154–159. https://doi.org/10.1016/j.jelechem.2019.04.063.

(49) Thieu, D. T.; Fawey, M. H.; Bhatia, H.; Diemant, T.; Chakravadhanula, V. S. K.; Behm, R. J.; Kübel, C.; Fichtner, M. CuF2 as Reversible Cathode for Fluoride Ion Batteries. *Adv. Funct. Mater.* **2017**, *27* (31). https://doi.org/10.1002/adfm.201701051.

(50) Yu, Y.; Lei, M.; Li, D.; Li, C. Near-Room-Temperature Quasi-Solid-State F-Ion Batteries with High Conversion Reversibility Based on Layered Structured Electrolyte. *Adv. Energy Mater.* **2023**, *13* (12). https://doi.org/10.1002/aenm.202203168.

(51) Shimoda, K.; Morita, Y.; Noi, K.; Fukunaga, T.; Ogumi, Z.; Abe, T. Practical Reversibility of CuF2 in a Bulk-Type All-Solid-State Fluoride-Ion Battery. *ACS Energy Lett.* **2023**, *8* (6), 2570–2575. https://doi.org/10.1021/acsenergylett.3c00459.

(52) Cui, H.; Gao, X.; Guo, K.; Liu, W.; Ouyang, B.; Yi, W. Lewis Acid–Base Synergistically Enhancing Practical Composite Electrolyte for Fluoride-Ion Batteries at Room Temperature. *Advanced Science* **2025**, *12* (27). https://doi.org/10.1002/advs.202502824.

(53) Shen, T.; Li, S.; Yue, K.; Zheng, J.; Ding, Y.; Song, S.; Li, C.; Jin, R.; Wu, Y.; Wang, Y.; Wang, Y.; Nai, J.; Liu, Y.; Shi, P.; Zou, S.; Luo, J.; Yuan, H.; Tao, X. LiF Doped β-$PbSnF_4$ with Improved Ionic Conductivity toward High-Performance All-Solid-State Fluoride-Ion Batteries. *J. Mater. Chem. A Mater.* **2025**. https://doi.org/10.1039/D5TA01188D.

(54) Nowroozi, M. A.; Clemens, O. Insights on the Behavior of Conversion-Based Anode Materials for Fluoride Ion Batteries by Testing against an Intercalation-Based Reference Cathode. *ACS Appl. Energy Mater.* **2018**, *1* (11), 6626–6637. https://doi.org/10.1021/acsaem.8b01630.

(55) Nowroozi, M. A.; Wissel, K.; Donzelli, M.; Hosseinpourkahvaz, N.; Plana-Ruiz, S.; Kolb, U.; Schoch, R.; Bauer, M.; Malik, A. M.; Rohrer, J.; Ivlev, S.; Kraus, F.; Clemens, O. High Cycle Life All-Solid-State Fluoride Ion Battery with La2NiO4+d High Voltage Cathode. *Commun. Mater.* **2020**, *1* (1), 1–16. https://doi.org/10.1038/s43246-020-0030-5.

(56) Rongeat, C.; Anji Reddy, M.; Diemant, T.; Behm, R. J.; Fichtner, M. Development of New Anode Composite Materials for Fluoride Ion Batteries. *J. Mater. Chem. A Mater.* **2014**, *2* (48), 20861–20872. https://doi.org/10.1039/c4ta02840f.

(57) Nowroozi, M. A.; Wissel, K.; Rohrer, J.; Munnangi, A. R.; Clemens, O. LaSrMnO4: Reversible Electrochemical Intercalation of Fluoride Ions in the Context of Fluoride Ion Batteries. *Chemistry of Materials* **2017**, *29* (8), 3441–3453. https://doi.org/10.1021/acs.chemmater.6b05075.

(58) Takami, T.; Saito, T.; Kamiyama, T.; Kawahara, K.; Fukunaga, T.; Abe, T. A New Bi0.7Fe1.3O1.5F1.7phase: Crystal Structure, Magnetic Properties, and Cathode Performance in Fluoride-Ion Batteries. *APL Mater.* **2020**, *8* (5), 4–10. https://doi.org/10.1063/5.0005817.

(59) Wissel, K.; Schoch, R.; Vogel, T.; Donzelli, M.; Matveeva, G.; Kolb, U.; Bauer, M.; Slater, P. R.; Clemens, O. Electrochemical Reduction and Oxidation of Ruddlesden − Popper- Type La 2 NiO 3 F 2 within Fluoride-Ion Batteries. **2021**. https://doi.org/10.1021/acs.chemmater.0c01762.

(60) Nowroozi, M. A.; Laune, B. De; Clemens, O. Reversible Electrochemical Intercalation and Deintercalation of Fluoride Ions into Host Lattices with Schafarzikite-Type Structure. **2018**, 617–623. https://doi.org/10.1002/open.201800106.

(61) Nowroozi, M. A.; Ivlev, S.; Rohrer, J.; Clemens, O. La2CoO4: A New Intercalation Based Cathode Material for Fluoride Ion Batteries with Improved Cycling Stability. *J. Mater. Chem. A Mater.* **2018**, *6* (11), 4658–4669. https://doi.org/10.1039/c7ta09427b.

(62) Delville, M. H.; Barbut, D.; Wattiaux, A.; Bassat, J. M.; Ménétrier, M.; Labrugère, C.; Grenier, J. C.; Etourneau, J. Electrochemical Fluorination of La2CuO4: A Mild “Chimie Douce” Route to Superconducting Oxyfluoride Materials. *Inorg. Chem.* **2009**, *48* (16), 7962–7969. https://doi.org/10.1021/ic900912d.

(63) Macmanus, J. L.; Fray, D. J.; Evetts, J. E. Fluorination of YIBaECU307_x by a Solid State Electrochemical Method; 1991; Vol. 184.

(64) Zhang, S.; Wang, T.; Zhang, J.; Miao, Y.; Yin, Q.; Wu, Z.; Wu, Y.; Yuan, Q.; Han, J. A Zero-Strain Insertion Cathode Material for Room-Temperature Fluoride-Ion Batteries. *ACS Appl. Mater. Interfaces* **2022**, *14* (21), 24518–24525. https://doi.org/10.1021/acsami.2c06376.

(65) Mohammad, M. S.; Nowroozi Geboren In Shiraz, A. *On the Development of Intercalation-Based Cathode Materials for All-Solid-State Fluoride Ion Batteries*; 2019. https://doi.org/https://doi.org/10.25534/tuprints-00011523.

(66) Vasala, S.; Jakob, A.; Wissel, K.; Waidha, A. I.; Alff, L.; Clemens, O. Reversible Tuning of Magnetization in a Ferromagnetic Ruddlesden–Popper-Type Manganite by Electrochemical Fluoride-Ion Intercalation. *Adv. Electron. Mater.* **2020**, *6* (2). https://doi.org/10.1002/aelm.201900974.

(67) Clemens, O.; Rongeat, C.; Reddy, M. A.; Giehr, A.; Fichtner, M.; Hahn, H. Electrochemical Fluorination of Perovskite Type BaFeO2.5. *Dalton Transactions* **2014**, *43* (42), 15771–15778. https://doi.org/10.1039/c4dt02485k.

(68) McRae, L. M.; Radomsky, R. C.; Pawlik, J. T.; Druffel, D. L.; Sundberg, J. D.; Lanetti, M. G.; Donley, C. L.; White, K. L.; Warren, S. C. Sc2C, a 2D Semiconducting Electride. *J. Am. Chem. Soc.* **2022**, *144* (24), 10862–10869. https://doi.org/10.1021/jacs.2c03024.

(69) Alhasani, Z. A. A.; Ajeel, F. N. DFT Investigations of Structural and Electronic Properties of Two-Dimensional Y2C and Y2CF2 Monolayers. *Nano Trends* **2025**, *9*. https://doi.org/10.1016/j.nwnano.2025.100073.

(70) Zhang, X.; Xiao, Z.; Lei, H.; Toda, Y.; Matsuishi, S.; Kamiya, T.; Ueda, S.; Hosono, H. Two-Dimensional Transition-Metal Electride Y2C. *Chemistry of Materials* **2014**, *26* (22), 6638–6643. https://doi.org/10.1021/cm503512h.

(71) Tojigamori, T.; Matsui, N.; Suzuki, K.; Hirayama, M.; Abe, T.; Kanno, R. Fluorination/Defluorination Behavior of Y2C in Fluoride-Ion Battery Anodes. *ACS Appl. Energy Mater.* **2024**, *7* (3), 1100–1108. https://doi.org/10.1021/acsaem.3c02613.

(72) Druffel, D. L.; Pawlik, J. T.; Sundberg, J. D.; Mcrae, L. M.; Lanetti, M. G.; Warren, S. C. First-Principles Prediction of Electrochemical Electron-Anion Exchange: Ion Insertion without Redox. *Journal of Physical Chemistry Letters* **2020**, *11* (1), 9210–9214. https://doi.org/10.1021/acs.jpclett.0c02266.

(73) Jain, A.; Ong, S. P.; Hautier, G.; Chen, W.; Richards, W. D.; Dacek, S.; Cholia, S.; Gunter, D.; Skinner, D.; Ceder, G.; Persson, K. A. Commentary: The Materials Project: A Materials Genome Approach to Accelerating Materials Innovation. *APL Mater.* **2013**, *1* (1). https://doi.org/10.1063/1.4812323.

(74) Kirklin, S.; Saal, J. E.; Meredig, B.; Thompson, A.; Doak, J. W.; Aykol, M.; Rühl, S.; Wolverton, C. The Open Quantum Materials Database (OQMD): Assessing the Accuracy of DFT Formation Energies. *NPJ Comput. Mater.* **2015**, *1*. https://doi.org/10.1038/npjcompumats.2015.10.

(75) Rühl, S. The Inorganic Crystal Structure Database (ICSD): A Tool for Materials Sciences. In *Materials Informatics: Methods, Tools and Applications*; wiley, 2019; pp 41–54. https://doi.org/10.1002/9783527802265.ch2.

(76) Hautier, G.; Jain, A.; Chen, H.; Moore, C.; Ong, S. P.; Ceder, G. Novel Mixed Polyanions Lithium-Ion Battery Cathode Materials Predicted by High-Throughput Ab Initio Computations. *J. Mater. Chem.* **2011**, *21* (43), 17147–17153. https://doi.org/10.1039/c1jm12216a.

(77) Kirklin, S.; Meredig, B.; Wolverton, C. High-Throughput Computational Screening of New Li-Ion Battery Anode Materials. *Adv. Energy Mater.* **2013**, *3* (2), 252–262. https://doi.org/10.1002/aenm.201200593.

(78) Aykol, M.; Kim, S.; Hegde, V. I.; Snydacker, D.; Lu, Z.; Hao, S.; Kirklin, S.; Morgan, D.; Wolverton, C. High-Throughput Computational Design of Cathode Coatings for Li-Ion Batteries. *Nat. Commun.* **2016**, *7*. https://doi.org/10.1038/ncomms13779.

(79) Xiao, Y.; Miara, L. J.; Wang, Y.; Ceder, G. Computational Screening of Cathode Coatings for Solid-State Batteries. *Joule* **2019**, *3* (5), 1252–1275. https://doi.org/10.1016/j.joule.2019.02.006.

(80) Kahle, L.; Marcolongo, A.; Marzari, N. High-Throughput Computational Screening for Solid-State Li-Ion Conductors. *Energy Environ. Sci.* **2020**, *13* (3), 928–948. https://doi.org/10.1039/c9ee02457c.

(81) Zhang, X.; Zhang, Z.; Yao, S.; Chen, A.; Zhao, X.; Zhou, Z. An Effective Method to Screen Sodium-Based Layered Materials for Sodium Ion Batteries. *NPJ Comput. Mater.* **2018**, *4* (1). https://doi.org/10.1038/s41524-018-0070-2.

(82) Zhang, Z.; Zhang, X.; Zhao, X.; Yao, S.; Chen, A.; Zhou, Z. Computational Screening of Layered Materials for Multivalent Ion Batteries. *ACS Omega* **2019**, *4* (4), 7822–7828. https://doi.org/10.1021/acsomega.9b00482.

(83) Li, W.; Han, C.; Wang, W.; Xia, Q.; Chou, S.; Gu, Q.; Johannessen, B.; Liu, H. K.; Dou, S. Stress Distortion Restraint to Boost the Sodium Ion Storage Performance of a Novel Binary Hexacyanoferrate. *Adv. Energy Mater.* **2020**, *10* (4). https://doi.org/10.1002/aenm.201903006.

(84) Gschwind, F.; Euchner, H.; Rodriguez-Garcia, G. Chloride Ion Battery Review: Theoretical Calculations, State of the Art, Safety, Toxicity, and an Outlook towards Future Developments. *European Journal of Inorganic Chemistry*. Wiley-VCH Verlag 2017, pp 2784–2799. https://doi.org/10.1002/ejic.201700288.

(85) Bhatia, H.; Thieu, D. T.; Pohl, A. H.; Chakravadhanula, V. S. K.; Fawey, M. H.; Kübel, C.; Fichtner, M. Conductivity Optimization of Tysonite-Type La1-XBaxF3-x Solid Electrolytes for Advanced Fluoride Ion Battery. *ACS Appl. Mater. Interfaces* **2017**, *9* (28), 23707–23715. https://doi.org/10.1021/acsami.7b04936.

(86) Rongeat, C.; Anji Reddy, M.; Witter, R.; Fichtner, M. Solid Electrolytes for Fluoride Ion Batteries: Ionic Conductivity in Polycrystalline Tysonite-Type Fluorides. *ACS Appl. Mater. Interfaces* **2014**, *6* (3), 2103–2110. https://doi.org/10.1021/am4052188.

(87) Mohammad, I.; Witter, R.; Fichtner, M.; Reddy, M. A. Introducing Interlayer Electrolytes: Toward Room-Temperature High-Potential Solid-State Rechargeable Fluoride Ion Batteries. *ACS Appl. Energy Mater.* **2019**, *2* (2), 1553–1562. https://doi.org/10.1021/acsaem.8b02166.

(88) Liu, L.; Yang, L.; Liu, M.; Li, X.; Shao, D.; Luo, K.; Wang, X.; Luo, Z. SnF2-Based Fluoride Ion Electrolytes MSnF4 (M = Ba, Pb) for the Application of Room-Temperature Solid-State Fluoride Ion Batteries. *J. Alloys Compd.* **2020**, *819*. https://doi.org/10.1016/j.jallcom.2019.152983.

(89) Wang, J.; Hao, J.; Duan, C.; Wang, X.; Wang, K.; Ma, C. A Fluoride-Ion-Conducting Solid Electrolyte with Both High Conductivity and Excellent Electrochemical Stability. *Small* **2022**, *18* (5). https://doi.org/10.1002/smll.202104508.

(90) Zang, Z.; Liu, L.; Yang, L.; Luo, K.; Zou, C.; Chen, X.; Tao, X.; Luo, Z.; Chang, B.; Wang, X. Preparation and Performance of Eu3+-Doped BaSnF4-Based Solid-State Electrolytes for Room-Temperature Fluoride-Ion Batteries. *ACS Sustain. Chem. Eng.* **2021**, *9* (38), 12978–12989. https://doi.org/10.1021/acssuschemeng.1c04523.

(91) Liu, J.; Yi, L.; Zeng, P.; Zou, C.; Chen, X.; Tao, X.; Liu, X.; Yang, L.; Zang, Z.; Chang, B.; Shen, Y.; Wang, X. Point Defect Engineering Enabled the High Ionic Conductivity of BaSnF4for Solid-State Fluoride-Ion Batteries at Room Temperature. *Energy and Fuels* **2022**, *36* (24), 15258–15267. https://doi.org/10.1021/acs.energyfuels.2c03509.

(92) Rongeat, C.; Anji Reddy, M.; Diemant, T.; Behm, R. J.; Fichtner, M. Development of New Anode Composite Materials for Fluoride Ion Batteries. *J. Mater. Chem. A Mater.* **2014**, *2* (48), 20861–20872. https://doi.org/10.1039/c4ta02840f.

(93) Bhatia, H.; Thieu, D. T.; Pohl, A. H.; Chakravadhanula, V. S. K.; Fawey, M. H.; Kübel, C.; Fichtner, M. Conductivity Optimization of Tysonite-Type La1-XBaxF3-x Solid Electrolytes for Advanced Fluoride Ion Battery. *ACS Appl. Mater. Interfaces* **2017**, *9* (28), 23707–23715. https://doi.org/10.1021/acsami.7b04936.

(94) Cui, H.; Gao, X.; Guo, K.; Liu, W.; Ouyang, B.; Yi, W. Lewis Acid–Base Synergistically Enhancing Practical Composite Electrolyte for Fluoride-ion Batteries at Room Temperature. *Advanced Science* **2025**. https://doi.org/10.1002/advs.202502824.

(95) Matsuo, Y.; Inamoto, J.; Mineshige, A.; Murakami, M.; Matsumoto, K.; Hagiwara, R. Charge-Discharge Behavior of Fluorine-Intercalated Graphite for the Positive Electrode of Fluoride Ion Shuttle Battery. *Electrochem. commun.* **2020**, *110*. https://doi.org/10.1016/j.elecom.2019.106626.

(96) Tojigamori, T.; Nakajima, H.; Miki, H.; Matsui, N.; Nakatani, T.; Fujinami, S.; Noi, K.; Tsukasaki, H.; Suzuki, K.; Hirayama, M.; Mori, S.; Abe, T.; Kanno, R. Reversible

Charge/Discharge Reaction of a Ternary Metal Fluoride, Pb2CuF6: A Highly Conductive Cathode Material for Fluoride-Ion Batteries. *ACS Appl. Energy Mater.* **2022**, *5* (1), 1002–1009. https://doi.org/10.1021/acsaem.1c03375.

(97) Nakano, H.; Matsunaga, T.; Mori, T.; Nakanishi, K.; Morita, Y.; Ide, K.; Okazaki, K. I.; Orikasa, Y.; Minato, T.; Yamamoto, K.; Ogumi, Z.; Uchimoto, Y. Fluoride-Ion Shuttle Battery with High Volumetric Energy Density. *Chemistry of Materials* **2021**, *33* (1), 459–466. https://doi.org/10.1021/acs.chemmater.0c04570.

(98) Yoshinari, T.; Zhang, D.; Yamamoto, K.; Kitaguchi, Y.; Ochi, A.; Nakanishi, K.; Miki, H.; Nakanishi, S.; Iba, H.; Uchiyama, T.; Watanabe, T.; Matsunaga, T.; Amezawa, K.; Uchimoto, Y. Kinetic Analysis and Alloy Designs for Metal/Metal Fluorides toward High Rate Capability for All-Solid-State Fluoride-Ion Batteries. *J. Mater. Chem. A Mater.* **2021**, *9* (11), 7018–7024. https://doi.org/10.1039/d0ta12055c.

(99) Konishi, H.; Minato, T.; Abe, T.; Ogumi, Z. Electrochemical Properties of Lead Fluoride Electrode in Fluoride Shuttle Battery. *Journal of Electroanalytical Chemistry* **2018**, *826*, 60–64. https://doi.org/10.1016/j.jelechem.2018.08.027.

(100) Inoishi, A.; Setoguchi, N.; Hori, H.; Kobayashi, E.; Sakamoto, R.; Sakaebe, H.; Okada, S. FeF3 as Reversible Cathode for All-Solid-State Fluoride Batteries. *Advanced Energy and Sustainability Research* **2022**, *3* (12). https://doi.org/10.1002/aesr.202200131.

(101) Zhang, D.; Yamamoto, K.; Ochi, A.; Wang, Y.; Yoshinari, T.; Nakanishi, K.; Nakano, H.; Miki, H.; Nakanishi, S.; Iba, H.; Uchiyama, T.; Watanabe, T.; Amezawa, K.; Uchimoto, Y. Understanding the Reaction Mechanism and Performances of 3d Transition Metal Cathodes for All-Solid-State Fluoride Ion Batteries. *Journal of Materials Chemistry A*. 2021, pp 406–412. https://doi.org/10.1039/d0ta08824b.

(102) Jiao, X.; Kirianova, A. V.; Xu, X.; Kapitanova, O. O.; Krivchenko, V. A.; Napolskiy, F. S.; Volkov, V. S.; Gallyamov, M. O.; Liu, Y. Conductive Additives for Improving the Rate Capability of Cathode Materials in Secondary Lithium Batteries. *ACS Appl. Energy Mater.* **2023**, *6* (5), 2855–2862. https://doi.org/10.1021/acsaem.2c03772.

(103) Stenina, I.; Shaydullin, R.; Kulova, T.; Kuz'mina, A.; Tabachkova, N.; Yaroslavtsev, A. Effect of Carbon Additives on the Electrochemical Performance of Li4Ti5O12/C Anodes. *Energies (Basel).* **2020**, *13* (15). https://doi.org/10.3390/en13153941.

(104) Lee, Y. K. The Effect of Active Material, Conductive Additives, and Binder in a Cathode Composite Electrode on Battery Performance. *Energies (Basel).* **2019**, *12* (4). https://doi.org/10.3390/en12040658.

(105) Zhang, Q.; Yu, Z.; Du, P.; Su, C. Carbon Nanomaterials Used as Conductive Additives in Lithium Ion Batteries; 2010; Vol. 4.

(106) Kwon, N. H.; Mouck-Makanda, D.; Fromm, K. M. A Review: Carbon Additives in LiMnPO4-and LiCoO2-Based Cathode Composites for Lithium Ion Batteries. *Batteries*. MDPI December 1, 2018. https://doi.org/10.3390/batteries4040050.

(107) Galatolo, G.; Alshangiti, O.; Di Mino, C.; Matthews, G.; Xiao, A. W.; Rees, G. J.; Schart, M.; Chart, Y. A.; Olbrich, L. F.; Pasta, M. Advancing Fluoride-Ion Batteries with a Pb-PbF2 Counter Electrode and a Diluted Liquid Electrolyte. *ACS Energy Lett.* **2024**, *9* (1), 85–92. https://doi.org/10.1021/acsenergylett.3c02228.

(108) Grenier, A.; Porras-Gutierrez, A. G.; Body, M.; Legein, C.; Chrétien, F.; Raymundo-Piñero, E.; Dollé, M.; Groult, H.; Dambournet, D. Solid Fluoride Electrolytes and Their Composite with Carbon: Issues and Challenges for Rechargeable Solid State Fluoride-Ion

Batteries. *Journal of Physical Chemistry C* **2017**, *121* (45), 24962–24970. https://doi.org/10.1021/acs.jpcc.7b07988.

(109) Hartman, S. T.; Mishra, R. Layered Electrides as Fluoride Intercalation Anodes. *J. Mater. Chem. A Mater.* **2020**, *8* (46), 24469–24476. https://doi.org/10.1039/d0ta06162j.

(110) Hosono, H.; Kitano, M. Advances in Materials and Applications of Inorganic Electrides. *Chem. Rev.* **2021**, *121* (5), 3121–3185. https://doi.org/10.1021/acs.chemrev.0c01071.

(111) Dye, J. L. Electrides: Early Examples of Quantum Confinement. *Acc. Chem. Res.* **2009**, *42* (10), 1564–1572. https://doi.org/10.1021/ar9000857.

(112) Sun, F.; Guo, Z.; Lu, Y.; Li, J.; Ye, T. N.; Hosono, H.; Wu, J. Electrides: Emerging Electronic Materials for Catalysis. *Fundamental Research*. KeAi Communications Co. January 1, 2025. https://doi.org/10.1016/j.fmre.2024.11.026.

(113) Dye, J. L. Electrides: Ionic Salts with Electrons as the Anions. *Science (1979).* **1990**, *247* (4943), 663–668. https://doi.org/10.1126/science.247.4943.663.

(114) Meng, W.; Bai, J.; Ma, F.; Jiao, Y.; Wang, S.; Jiang, J.; Zhang, X.; Cheng, Z.; Yang, T. Magnetic Electrides: Recent Advances in Materials Realization and Application Prospects. *Applied Physics Reviews*. American Institute of Physics March 1, 2025. https://doi.org/10.1063/5.0233622.

(115) Zhang, X.; Yang, G. Recent Advances and Applications of Inorganic Electrides. *Journal of Physical Chemistry Letters* **2020**, *11* (10), 3841–3852. https://doi.org/10.1021/acs.jpclett.0c00671.

(116) Kraus, C. A. *Solutions of Metals in Non-Metallic Solvents IV*; 1908. https://pubs.acs.org/sharingguidelines.

(117) Cesium 18-Crown-6 Compounds. A Crystalline Ceside and a Crystalline Electride. https://pubs.acs.org/sharingguidelines.

(118) First Electride Crystal Structure.

(119) High-Density Electron Anions in a Nanoporous Single Crystal: [Ca24Al28O64]4ℏ(4e⋗).

(120) Tada, T.; Takemoto, S.; Matsuishi, S.; Hosono, H. High-Throughput Ab Initio Screening for Two-Dimensional Electride Materials. *Inorg. Chem.* **2014**, *53* (19), 10347–10358. https://doi.org/10.1021/ic501362b.

(121) Lee, K.; Kim, S. W.; Toda, Y.; Matsuishi, S.; Hosono, H. Dicalcium Nitride as a Two-Dimensional Electride with an Anionic Electron Layer. *Nature* **2013**, *494* (7437), 336–340. https://doi.org/10.1038/nature11812.

(122) Zhang, Z.; Jiang, Y.; Li, J.; Miyazaki, M.; Kitano, M.; Hosono, H. A 2D Ba $_2$ N Electride for Transition Metal-Free N $_2$ Dissociation under Mild Conditions. *J. Am. Chem. Soc.* **2023**. https://doi.org/10.1021/jacs.3c09362.

(123) McRae, L. M.; Radomsky, R. C.; Pawlik, J. T.; Druffel, D. L.; Sundberg, J. D.; Lanetti, M. G.; Donley, C. L.; White, K. L.; Warren, S. C. Sc2C, a 2D Semiconducting Electride. *J. Am. Chem. Soc.* **2022**, *144* (24), 10862–10869. https://doi.org/10.1021/jacs.2c03024.

(124) Burton, L. A.; Ricci, F.; Chen, W.; Rignanese, G. M.; Hautier, G. High-Throughput Identification of Electrides from All Known Inorganic Materials. *Chemistry of Materials* **2018**, *30* (21), 7521–7526. https://doi.org/10.1021/acs.chemmater.8b02526.

(125) Zhu, Q.; Frolov, T.; Choudhary, K. Computational Discovery of Inorganic Electrides from an Automated Screening. *Matter* **2019**, *1* (5), 1293–1303. https://doi.org/10.1016/j.matt.2019.06.017.

(126) Zhang, X.; Meng, W.; Liu, Y.; Dai, X.; Liu, G.; Kou, L. Magnetic Electrides: High-Throughput Material Screening, Intriguing Properties, and Applications. *J. Am. Chem. Soc.* **2023**, *145* (9), 5523–5535. https://doi.org/10.1021/jacs.3c00284.

(127) Weaver, S. M.; Sundberg, J. D.; Slamowitz, C. C.; Radomsky, R. C.; Lanetti, M. G.; McRae, L. M.; Warren, S. C. Counting Electrons in Electrides. *J. Am. Chem. Soc.* **2023**. https://doi.org/10.1021/jacs.3c10876.

(128) Weaver, S. M.; Lanetti, M. G.; Slamowitz, C. C.; Radomsky, R. C.; Warren, S. C. Assessing Dimensionality in Electrides. *The Journal of Physical Chemistry C* **2025**. https://doi.org/10.1021/acs.jpcc.4c06803.

(129) Mercadier, B.; Coles, S. W.; Duttine, M.; Legein, C.; Body, M.; Borkiewicz, O. J.; Lebedev, O.; Morgan, B. J.; Masquelier, C.; Dambournet, D. Dynamic Lone Pairs and Fluoride-Ion Disorder in Cubic-$BaSnF_4$. *J. Am. Chem. Soc.* **2023**. https://doi.org/10.1021/jacs.3c08232.

(130) Lian, X.; Dambournet, D.; Salanne, M. Stereoactive Electron Lone Pairs Facilitate Fluoride Ion Diffusion in Tetragonal BaSnF4. *Chemistry of Materials* **2025**, *37* (1), 378–386. https://doi.org/10.1021/acs.chemmater.4c02756.

(131) DENES, G.; Birchall, T.; Sayer, M.; Bell, M. F. *BaSnF4- A NEW FLUORIDE IONIC CONDUCTOR WITH THE PbSnF 4 STRUCTUR*; 1984; Vol. 13.

(132) Matsui, N.; Murakami, M.; Mori, K.; Saito, T.; Shimizu, K.; Suzuki, K.; Kanno, R. Effect of Pb 6s2 Lone Pair on the Potential Flattening of Fluoride-Ion Conduction in Perovskite-Type Fluoride. *J. Mater. Chem. A Mater.* **2024**, *12* (7), 3989–3996. https://doi.org/10.1039/d3ta06367d.

(133) Park, J.; Hwang, J. Y.; Lee, K. H.; Kim, S. G.; Lee, K.; Kim, S. W. Tuning the Spin-Alignment of Interstitial Electrons in Two-Dimensional Y2C Electride via Chemical Pressure. *J. Am. Chem. Soc.* **2017**, *139* (48), 17277–17280. https://doi.org/10.1021/jacs.7b10338.

(134) Tang, H.; Wan, B.; Gao, B.; Muraba, Y.; Qin, Q.; Yan, B.; Chen, P.; Hu, Q.; Zhang, D.; Wu, L.; Wang, M.; Xiao, H.; Gou, H.; Gao, F.; Mao, H. kwang; Hosono, H. Metal-to-Semiconductor Transition and Electronic Dimensionality Reduction of Ca2N Electride under Pressure. *Advanced Science* **2018**, *5* (11). https://doi.org/10.1002/advs.201800666.

(135) Faseela, K. P.; Kim, Y. J.; Kim, S. G.; Kim, S. W.; Baik, S. Dramatically Enhanced Stability of Silver Passivated Dicalcium Nitride Electride: Ag-Ca2N. *Chemistry of Materials* **2018**, *30* (21), 7803–7812. https://doi.org/10.1021/acs.chemmater.8b03202.

(136) Li, W.; You, Y.; Choi, J. H. Oxidation, Stability, and Magnetic Ground States of Two-Dimensional Layered Electrides. *Journal of Physical Chemistry C* **2020**, *124* (46), 25316–25321. https://doi.org/10.1021/acs.jpcc.0c07337.

(137) Wang, D.; Li, H.; Zhang, L.; Sun, Z.; Han, D. X.; Niu, L.; Zhong, X.; Qu, X.; Yang, L. First-Principles Study on OH-Functionalized 2D Electrides: Ca 2 NOH and Y 2 C(OH) 2 , Promising Two-Dimensional Monolayers for Metal-Ion Batteries. *Appl. Surf. Sci.* **2019**, *478*, 459–464. https://doi.org/10.1016/j.apsusc.2019.01.256.

(138) Li, K.; Gong, Y.; Wang, J.; Hosono, H. Electron-Deficient-Type Electride Ca5Pb3: Extension of Electride Chemical Space. *J. Am. Chem. Soc.* **2021**, *143* (23), 8821–8828. https://doi.org/10.1021/jacs.1c03278.

(139) Royce, B. S. H. THE CREATION OF DEFECTS IN ALKALI HALIDES; 1967.

(140) Sung Wng Kim; Terumasa Shimoyama; Hideo Hosono. Solvated Electrons in High-Temperature and Glasses of TheRoom-Temperature Electride [Ca24Al28O64]4+ 4e−. *Science (1979).* **2011**, *333* (6038), 68–71. https://doi.org/10.1126/science.1202232.

(141) Johnson, L. E.; Sushko, P. V.; Tomota, Y.; Hosono, H. Electron Anions and the Glass Transition Temperature. *Proc. Natl. Acad. Sci. U. S. A.* **2016**, *113* (36), 10007–10012. https://doi.org/10.1073/pnas.1606891113.

(142) Akola, J.; Kohara, S.; Ohara, K.; Fujiwara, A.; Watanabe, Y.; Masuno, A.; Usuki, T.; Kubo, T.; Nakahira, A.; Nitta, K.; Uruga, T.; Richard Weber, J. K.; Benmore, C. J. Network Topology for the Formation of Solvated Electrons in Binary CaO-Al2O3 Composition Glasses. *Proc. Natl. Acad. Sci. U. S. A.* **2013**, *110* (25), 10129–10134. https://doi.org/10.1073/pnas.1300908110.

(143) Yang, J.; Pan, J.; Deng, J.; Zhang, Y. F.; Li, Y.; Zhu, Y.; Wan, G.; Du, S. Vacancy-Induced Anionic Electrons in Single-Metal Oxides and Their Possible Applications in Ammonia Synthesis. *J. Am. Chem. Soc.* **2024**, *146* (30), 21160–21167. https://doi.org/10.1021/jacs.4c07362.

(144) Chae, J.; Kim, G. Effects of a Single Vacancy on Electronic Properties of a Ca2N Electride Bilayer. *Appl. Surf. Sci.* **2023**, *612*. https://doi.org/10.1016/j.apsusc.2022.155721.

(145) Ahmed, S.; González-Cataldo, F.; Robinson, V. N.; Militzer, B. Electride Behavior at High Pressure in Silicon and Other Elements in Solid and Liquid Phases. *Phys. Rev. B* **2025**, *112* (16), 1651111–16511113. https://doi.org/10.1103/14dp-bf1n.

(146) Yu, X. X.; Weinberger, C. R.; Thompson, G. B. Ab Initio Investigations of the Phase Stability in Group IVB and VB Transition Metal Carbides. *Comput. Mater. Sci.* **2016**, *112*, 318–326. https://doi.org/10.1016/j.commatsci.2015.10.038.

(147) Goretzki, H. Neutron Diffraction Studies on Titanium-Carbon and Zirconium-Carbon Alloys. *physica status solidi (b)* **1967**, *20* (2), K141–K143. https://doi.org/10.1002/pssb.19670200260.

(148) Em, V. T.; Tashmetov, M. Y. The Structure of the Ordered Phase in Rocksalt Type Titanium Carbide, Carbidenitride, and Carbidehydride. *Phys. Status Solidi B Basic Res.* **1996**, *198* (2), 571–575. https://doi.org/10.1002/pssb.2221980202.

(149) Bell, P. S.; Lewis, M. H. The Ordered Distribution of Carbon Atoms in Titanium Carbide. *Philosophical Magazine* **1971**, *24* (191), 1247–1251. https://doi.org/10.1080/14786437108217083.

(150) Nguyen, J.; Glandut, N.; Jaoul, C.; Lefort, P. Electrochemical Hydrogen Insertion in Substoichiometric Titanium Carbide TiC0.6: Influence of Carbon Vacancy Ordering. *Langmuir* **2013**, *29* (38), 12036–12042. https://doi.org/10.1021/la402043x.

CHAPTER 2: METHODS[1]

2.1 Introduction

Materials chemistry research is often approached in three ways: computational modeling, experimental synthesis, and characterization of structure and properties. Together, these approaches make it possible to both understand materials at a fundamental level and identify promising new ones. My doctoral work at the University of North Carolina at Chapel Hill has involved developing skills across all three areas, and the methods used in each are described in this chapter.

2.2 Computational Methods

2.2.1 High-Throughput Computational Screening of FIB Materials

This section presents the computational screening strategies used in two complementary FIB electrode discovery efforts. The first effort focuses on screening ternary metal fluorides compounds as prospective cathode materials by identifying charge/discharge pairs and evaluating their thermodynamic stability and electrochemical properties. The second effort examines competing thermodynamic driving forces among binary metal fluorides and binary metal carbides to identify chemical and structural trends relevant to carbon conductive additive stability. Together, these studies use high-throughput investigation of the Materials Project database to move from large design spaces toward smaller sets of candidates and trends that can support more focused mechanistic interpretation and future experimental investigation.

---

[1] Portions of this chapter reproduced with permission from McTaggart, D. H.; Sundberg, J. D.; McRae, L. M.; Warren, S. C. Assessing Ternary Materials for Fluoride-Ion Batteries. Sci Data 2023, 10 (1), 1–8 and McTaggart, D.; Warren, S. C.; Clemens, O. Reconsidering Anode Materials for Fluoride-Ion Batteries–The Unexpected Roles of Carbide Formation. ChemSusChem 2023, 16, e202300486.

2.2.1.1 General High-Throughput Approach

Across both screening efforts, all data retrieval, filtering, and workflow execution were carried out via Python scripting through Simmate[1] (developed by Warren Lab alum Dr. Jack Sundberg) using API access to the Materials Project database,[2] with additional structure handling and analysis performed using pymatgen.[3] Simmate provided a consistent interface for querying Materials Project entries, and supported by pymatgen enabled the application of composition and stability based filters, the removal of compositional duplicates, and the assembly of thermodynamic data. Additional details can be found in Simmate, pymatgen, and Materials Project API documentation.

In each study, Spyder was used as the Python programming interface, and necessary database connections were made shown in Figure 2-1. Importantly, the Materials Project database is accessed in two ways. Both screenings use the first method through Simmate's "third_parties" module using MatprojStructure which allows efficient screening using Simmate's architecture. In the ternary cathode screening, additional API access via MPRester was required to access interface reaction capabilities. A user must make a Materials Project account to access a custom API key.

```
from simmate.database import connect
from simmate.database.third_parties import MatprojStructure

import pandas as pd
import copy

from pymatgen.core.composition import Composition
from pymatgen.core.structure import Structure
from pymatgen.ext.matproj import MPRester
from pymatgen.analysis.cost import CostAnalyzer, CostDBCSV

mpr = MPRester("eXE8IJUp6lZSxLAo")            # Legacy MP API key, must use this for interface reactions
```

Figure 2-1. Python imports for high-throughput screening projects. A Materials Project account is necessary to obtain and API key for advanced interfacing.

Candidate compounds were identified from Materials Project by applying a convex-hull stability threshold of 75 meV/atom (Figure 2-2) to only include materials that are stable within the expected uncertainty of DFT-derived formation energies (see 2.2.1.3 DFT Energy Uncertainty**)**. Multiple phases of the same reduced composition were consolidated by keeping only the lowest-energy representative. Additional filters for each screening were applied and described later, but the following calculation of electrochemical potentials vs. Li/LiF was shared. I use ternary fluorides in the description below, with the same approach used for metal carbides.

```
# Initial filter, order by hull energy so that duplicates can be deleted correctly
all_f_strucs = MatprojStructure.objects.filter(
    elements__icontains='"F"',
    energy_above_hull__lt=0.075,
    nelements__gt=2,
).order_by('energy_above_hull').all()
```

Figure 2-2. Initial filtering step for ternary fluoride structures. Similar calls were used for metal carbide screening. “Energy_above_hull” less than 75 meV/atom was a critical stability filtering criteria.

2.2.1.2 Electrochemical Potentials

It is known that open circuit voltages can be predicted for lithium-ion battery materials using energies calculated from DFT+U methods.[4] It is common to refer to voltages against metallic lithium in these systems, which can be considered the natural limit for the usability of a component in a lithium-ion battery. In fluoride-ion batteries, F_2 can be used analogously to calculate open circuit voltages for materials in these systems.[5] These potentials can be calculated for materials by using a hypothetical F_2 electrode according to the following reaction:

$$AB + \frac{x}{2} F_2 \rightarrow ABF_x \qquad (1)$$

While this reaction is useful theoretically, the realization of a gaseous F_2 electrode is unlikely. Moreover, the potentials obtained are oxidation potentials rather than reduction

potentials. To provide a more conventional perspective, we calculate potentials using the Li/LiF pair as an anode according to the following equation:

$$ABF_x + x\ Li \rightarrow AB + x\ LiF \quad (2)$$

The voltages for these two reactions can be calculated starting from the Nernst equation:

$$Potential = -\frac{\Delta G_{rxn}}{xF} \quad (3)$$

Where ΔG_{rxn} is the change in Gibbs free energy of the reaction (J/mol), *x* is the number of fluoride ions transferred, and *F* is Faraday's constant. Volume ($P\Delta V_{rxn}$) and entropic ($T\Delta S_{rxn}$) effects can be neglected for the calculation of ΔG_{rxn} (= $\Delta U_{rxn} + P\Delta V_{rxn} - T\Delta S_{rxn}$) because $P\Delta V_{rxn}$ is on the order of 10^{-5} eV and $T\Delta S_{rxn}$ is on the scale of thermal energy, which are both much smaller than ΔU_{rxn} (~10^{1} eV). Thus, ΔG_{rxn} can be reasonably obtained from the change in internal energy (ΔU_{rxn}).[4,6,7] The Materials Project calculates internal energy for every entry in its database using DFT+U, so ΔG_{rxn} can be calculated from these values for (1) and (2) respectively according to the following equation:

$$\Delta G_{rxn} \approx \Delta U_{rxn} = (U_{ABFx}) - (U_{AB} + \frac{x}{2} U_{F2}) \quad (4)$$

and

$$\Delta G_{rxn} \approx \Delta U_{rxn} = (U_{AB} + x\ U_{LiF}) - (U_{ABFx} + x\ U_{Li}) \quad (5)$$

where U_y is the internal energy of each compound. Because Materials Project provides internal energy values in eV rather than J, Faraday's constant can be dropped from (3). Thus, potentials vs. Li/LiF were calculated from $-\Delta G_{rxn}/x$. Figure 2-3 shows the implementation of these calculations.

```python
# Voltage vs Li/LIf
def Voltage(m1_f, m2_def, e_per_a_f, e_per_a_def, f_transfer, scale_factor):
    # -9.6903 is LiF energy and -1.909 is Li energy
    if scale_factor != 1:
        return (((m2_def.atoms_per_fu / scale_factor)* e_per_a_def + f_transfer * -9.6903) - (m1_f.atoms_per_fu * e_per_a_f + f_transfer * -1.909))
    else:
        return ((m2_def.atoms_per_fu * e_per_a_def + f_transfer * -9.6903) - (m1_f.atoms_per_fu * e_per_a_f + f_transfer * -1.909)) / -f_transfer
```

Figure 2-3. Calculation of voltage vs. Li/LiF for ternary fluoride materials. Similar analysis was conducted for metal fluoride and metal carbide reduction.

2.2.1.3 DFT Energy Uncertainty

Many of the reported properties rely on DFT internal energy calculations, which are known to incorporate systematic and random error. Particularly, the approximate DFT functionals result in errors due to changes of electron self-interaction in localized transition metal states. This originates from changes in oxidation state upon product formation from discrete reactants. Known binding errors of diatomic molecules (F_2, O_2, N_2, Cl_2, H_2) using LDA and GGA functionals further complicate the calculation of accurate internal energies. This is mitigated in transition metal cations by applying a Hubbard U value to d or f orbitals and constant energy corrections based on experimental comparison for anionic species (F^-, O^{2-}, S^{2-} …). Materials Project employs corrections for both errors with a mix of GGA and GGA+U functionals as well as anion-specific corrections.[8–12] Our calculations used these corrections, which reduces the error in GGA or GGA+U formation enthalpies from ≈ 175–450 meV/atom (uncorrected) to ≈ 45–55 meV/atom (corrected). The magnitude of these energies supported the chosen filtering value of 75meV above hull, slightly above the noted correction error. The calculation of potentials relies on internal energies of multiple structures, which somewhat increases the total error. These errors are small compared to the potentials that are spanned across all materials studied, thereby supporting our ability to sort and rank materials according to the predicted potential. The uncertainties of activation energies for F-ion conduction were described previously.[13]

2.2.1.4 Ternary Cathode Screening

This section describes the screening methodology specific to the ternary cathode materials. Initial filtering of the Materials Project database included: (1) the structure contained fluorine, (2) the number elements was greater than two (primarily ternary with several four and five element fluorides), and (3) the energy above the convex hull was less than 75 meV/atom (see above). This yielded the initial set of fluorinated host structures considered for further analysis.

2.2.1.4.1 Identification of Defluorination Pairs

Fluoride-ion batteries operate through reversible fluoride extraction and reinsertion at the cathode. To evaluate this electrochemical process computationally, I attempted to pair each candidate fluorinated structure with a corresponding defluorinated structure representing the discharged cathode state. Two classes of defluorination pairs were identified: complete (i.e., $NaBiF_6$/NaBi) and partial (i.e., $CaNiF_6$/$CaNiF_5$).

For complete defluorination pairs, fluorine was removed from the composition of each candidate, and the resulting reduced formula was queried against the Materials Project database. A match was identified if an entry with an identical reduced formula and a hull energy within 75 meV/atom existed. In cases of multiple matches, the lowest-energy representative was selected. This procedure identifies pairs in which all fluoride ions are extracted during cycling, yielding a fully defluorinated product. There were 425 fluorinated/fully defluorinated pairs identified after this step.

For partial defluorination pairs, I searched for entries with the same elements as the fluorinated entry, with the same ratios of non-fluoride elements, and within 75 meV/atom of hull. An additional constraint required that the atomic fraction of fluorine in the parent structure exceed that of the candidate. For structures with identical compositions, we filtered the dataset

to select the lowest energy phase. This resulted in 382 fluorinated/partially defluorinated pairs. Thus, a total of 807 fluorinated/defluorinated pairs were taken forward through the remaining analyses.

2.2.1.4.2 Scale Factor Correction

The difference in atoms per formula unit between each structure pair, which is used to calculate the number of fluorides transferred and other properties, assumes that each reduced formula has the same number of each type of non-F atoms. This is not true for all structures, however. Therefore, we counted the number of non-fluoride atoms in each pair and rescaled the reduced formulas so that the number of non-fluoride atoms remained unchanged.

2.2.1.4.3 Interface Reaction Analysis

Thermodynamic cyclability between fluorinated and defluorinated pairs was assessed through interface reaction analysis using the Materials Project API "MPRester". For each fluorination pair, the "get_interface_reactions" method was used. This method evaluates whether two compositions in contact react to form more thermodynamically stable phases at various mixing ratios, and is described in greater detail in Chapter 3. A charge/discharge pair was classified as "direct" if the interface reaction products yielded the same input materials (indicating no decomposition) or "indirect" if new product phases were thermodynamically favored. Of the 807 charge/discharge pairs, 168 demonstrated desirable direct reactions.

Screening level	Number of candidate ternary fluoride materials
Materials Project database	5,261
Full defluorination charge/discharge pairs	425
Partial defluorination charge/discharge pairs	382
Direct reaction material pairs	168

Table 2-1. Quantification of ternary fluoride candidates along screening workflow

2.2.1.4.4 Calculated Properties

The following properties were calculated for each direct reaction structure pair, including electrochemical potential vs. Li/LiF described above.

Volume per fluorine (Å^3): Volume per fluoride was calculated using the volume per formula unit of the fluorinated structure divided by the difference in fluorine atoms between the fluorinated and defluorinated structures.

Percent expansion: The expansion from the defluorinated to fluorinated structure was calculated by dividing the fluorinated volume per formula unit by the defluorinated volume per formula unit, subtracting 1, and then multiplying by 100%.

Gravimetric Capacity (mAh/g): The gravimetric capacity for each fluorinated structure was calculated according to Faraday's Law:

$$Capacity = \frac{n * F}{C * MW}$$

Where *n* is the number of charge carriers (fluoride ions), *F* is Faraday's constant (96,485.3 C/mol), *C* is a conversion factor (3.6 C/mAh), and *MW* is the molecular weight of the fluorinated structure in g/mol.

Gravimetric Energy Density (Wh/kg): The gravimetric energy density was obtained by multiplying the gravimetric capacity by voltage.

Volumetric Energy Density (Wh/L): The volumetric energy density was calculated by multiplying the gravimetric energy density by the density of the fluorinated material.

Cost analysis: A cost analysis was done for each material using pymatgen's CostAnalyzer module. Adaptations were made to pymatgen's cost module for more accurate price approximations. Original module reference prices are based on pure elemental forms, which misrepresent the predicted costs because many elements can be obtained as salts for a much

lower cost. Therefore, all elemental costs are obtained from the Wikipedia “Prices of chemical elements” page, which more accurately takes this into account. The prices listed on Wikipedia are primarily average market prices for bulk trade, but when this data is not available the price of a compound is used, per mass of the given element. Costs were not calculated for Rb2UF7 due to issues with the module in calculating a phase diagram containing U.

Transport barrier (eV): When data was available, the activation energy for fluoride transport is presented.[14]

2.2.1.4.4 Data Compilation

Table 2-2 provides the list of column titles for the produced data and a description of each. The dataset is available in the Appendix with some columns listed below excluded. The full dataset is available at https://github.com/donmctaggart15/ternary_f_cathodes.

Column name	Description
orig_index	Original index from initial database filtering
f_form	Reduced formula of fluorinated structure
def_form	Reduced formula of defluorinated structure
voltage_lif	Voltage of F/deF pair vs. Li/LiF
voltage_f2	Voltage of F/deF pair vs F_2
vol_p_f	Volume per mobile F ($Å^3$) (fluorinated)
per_exp	Percent expansion from defluorinated to fluorinated
grav_cap	Gravimetric capacity (mAh/g) (fluorinated)
grav_e_den	Gravimetric energy density (Wh/kg) (fluorinated)
vol_e_den	Volumetric energy density (Wh/L) (fluorinated)
f_transfer	Number of mobile F ions between pair
f_cost_p_kg	$/kg of fluorinated structure
def_cost_p_kg	$/kg of defluorinated structure
f_cost_p_mol	$/mol of fluorinated structure
def_cost_p_mol	$/mol of defluorinated structure

cost_p_mol_f	$/mol of mobile F ion (fluorinated)
log_cost_p_mol_f	Log of $/mol of mobile F ion (fluorinated)
f_id	Materials Project ID (fluorinated)
def_id	Materials Project ID (defluorinated)
f_spacegroup	Spacegroup number (fluorinated)
def_spacegroup	Spacegroup number (defluorinated)
f_e_hull	Hull energy (eV) (fluorinated)
def_e_hull	Hull energy (eV) (defluorinated)
f_bandgap	Bandgap (eV) (fluorinated)
def_bandgap	Bandgap (eV) (defluorinated)
f_barrier	Diffusion barrier (eV) (fluorinated)
def_barrier	Diffusion barrier (eV) (defluorinated)
direct	Is conversion a direct reaction?
products	Products of interface reaction (equal to F structure if direct)
type	Complete or partial defluorination

Table 2-2: Column titles in cathode datasets with descriptions.

2.2.2 Carbide Screening

This section describes the screening choices made for binary metal fluoride (MF) and binary metal carbide (MC) materials beyond the general shared approach above. The Materials Project database was initially screened to include all binary metal fluorides (522 structures). For compositions with more than one known phase, only the most stable phase was used to ensure that each composition was represented by a single entry (258 structures). The database was re-screened for each MF compound to identify MC compounds. Like the MF materials, some MC compositions had more than one phase so only the most stable of these was used. This still allowed for multiple compositions of the same MC system. Carbides were paired with the original fluoride such that all unique fluoride/carbide combinations (930) for element M were represented. Some elements only had carbide structures with hull energies close to or above

the 75 meV/atom limit (i.e., Co_2C) but were still included in later analysis due to their interesting structural properties. For each fluoride/carbide pair, relevant properties like reduction potentials, hull stability, and space group were assembled and are presented in the Appendix. These results are discussed in Chapter 4.

2.2.3 Titanium Center Geometry in Partially Ordered Ti_2C

The carbon sublattice exists at varying degrees of partial order at different temperatures in the converged Ti_2C Monte Carlo (MC) supercells. To quantify carbon sublattice ordering in temperature resolved Ti_2C configurations, I developed a Python-based structural analysis workflow to identify local Ti-centered vacancy environments and their relationships to the ordered Fd-3m state. Starting from each Ti_2C MC structure, the complete carbon sublattice was reconstructed according to the underlying FCC basis. The carbon sublattice was then compared to the actual carbon atoms present in the structure. This produced a map of the complete carbon sublattice in which every carbon position was assigned as occupied or vacant.

Local ordering was then characterized from the perspective of each Ti atom. For rocksalt Ti_2C, every Ti site occupies an octahedral cage of six C positions with different degrees of occupation. These six C positions, defining Ti's first coordination shell, were identified and assigned to a fixed directional basis, allowing construction of a six-bit local motif in which each bit denotes the presence or absence of carbon at one of the six neighboring sites, where 0 is vacant and 1 is C occupied. This yields $2^6 = 64$ possible carbon configurations around a given Ti center. In ordered Fd-3m Ti_2C, every Ti atom is coordinated by a motif containing three carbons and three vacancies arranged in one of eight octahedral face-capping configurations (Figure 2-4). On this basis, I define a "first neighbor ordered Ti center" (1NOTC) as a Ti atom whose six-bit motif matches one of the eight Fd-3m octahedral face configurations. The 1NOTC fraction in Monte Carlo supercells therefore provides a simple nearest-neighbor measure of carbon ordering. Applying this metric across the temperature series showed that 1NOTC fraction

increases approximately linearly from 1500K to 400K, consistent with the expected increase in thermodynamic ordering upon cooling. At 400K, the structure becomes Fd-3m. A limitation of the 1NOTC metric is that it overpredicts Fd-3m character at high temperatures. At 1300 K the 1NOTC fraction is ~25%, yet experimental quenching from 1300 K produces no detectable partial ordering via XRD, indicating that the 1NOTC metric alone does not reliably correlate with Fd-3m character.

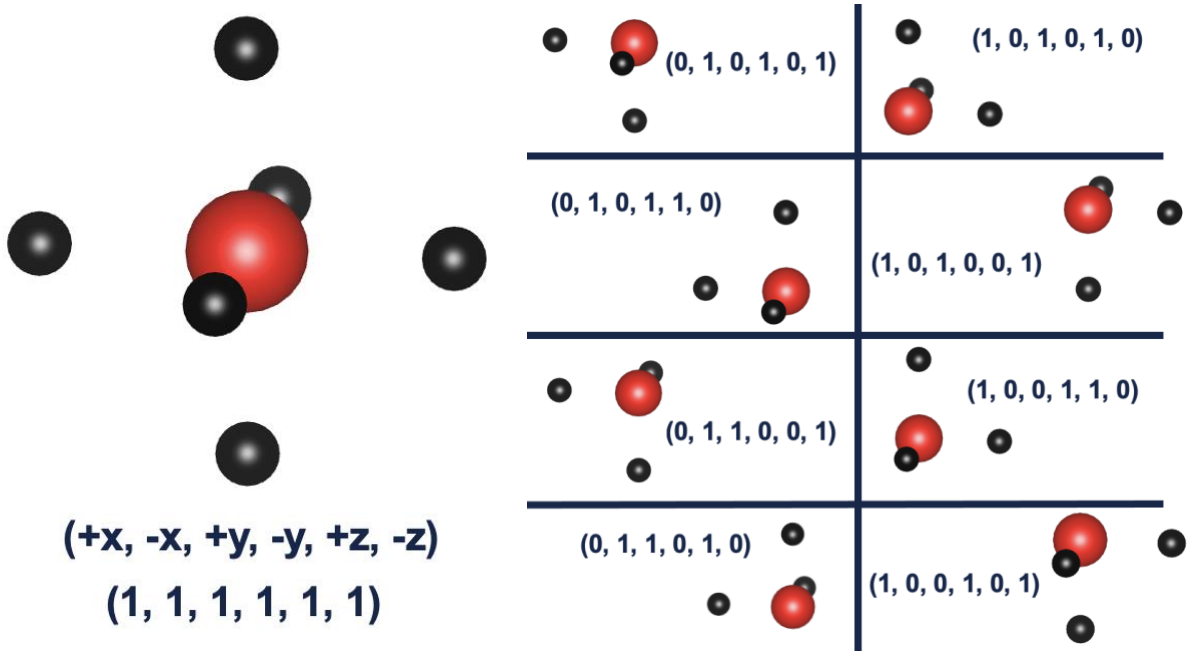


Figure 2-4: Six-bit motif representation of C (black) configuration around Ti (red) centers. The left shows the fully C-occupied octahedral cage around Ti, represented by (1, 1, 1, 1, 1, 1). The right shows the eight octahedral face-capping configurations present in Fd-3m (1NOTCs).

A more restrictive metric was introduced to address this limitation. For each Ti atom, the 12 nearest Ti neighbors were identified and labeled with their respective local C coordination. For Ti centers in Fd-3m, the following criteria are met:

1. All 12 Ti neighbors have local C configurations which are one of the eight octahedral face configurations (1NOTC).

2. No Ti neighbors have the same (i.e., (0, 1, 0, 1, 0, 1)) or inverse (i.e., (1, 0, 1, 0, 1, 0)) 1NOTC configuration as the central Ti.

3. Two Ti neighbors connected by a straight line which passes through the central Ti (opposite pair) have the same 1NOTC configuration.

4. A second opposite pair of Ti neighbors perpendicular to the first opposite pair have the inverse 1NOTC configuration of the first opposite pair.

5. Each 1NOTC configuration, excluding the central Ti's configuration or inverse configuration, is represented twice among the 12 neighbors.

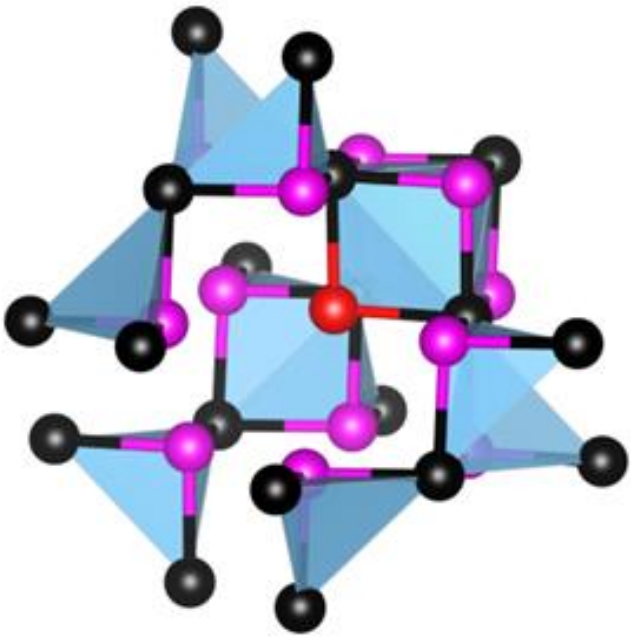


Figure 2-5: 2NOTC configuration. Central Ti (red) and 12 neighbor Ti's (pink), each with 1NOTC C (black) configurations.

Therefore, I define a "second neighbor ordered Ti center" (2NOTC) as Ti atoms who's surrounding Ti neighbors also meet the above criteria. In this way, the 2NOTC metric tests not only whether a Ti atom has the correct local C configuration, but also whether that configuration is embedded within an extended ordering environment more suggestive of Fd-3m-like order.

Measuring the 2NOTC fraction in MC supercells identifies zero centers at 1300 K, in contrast the ~25% predicted by 1NOTC, bringing this structural analysis into much better agreement with experiment. Therefore, the 2NOTC fraction was used as the primary structural descriptor of ordering evolution and is discussed further in Chapter 5.

2.2.4 Other Tools Used

First-principles calculations were performed using the Vienna *ab initio* Simulation Package (VASP) with projector-augmented wave (PAW) potentials.[15–17] Structural relaxations and single-point energy calculations were carried out using PBE or r²SCAN meta-GGA functional, with DFT-D3 dispersion corrections included where appropriate.[18–20] To model configurational disorder on the Ti_2C carbon sublattice, a cluster expansion model was constructed using the CLEASE package[21] based on a DFT training set of random Ti_2C configurations.[22] The fitted model was then used for canonical Monte Carlo simulations from 1K to 1500K on ~1800 atom supercells to sample equilibrium vacancy arrangements and ordering behavior. Resulting configurations were analyzed using the Ti center geometries described above. Electronic structure analysis was carried out using the electron localization function (ELF)[23] and the BadELF method[24] to examine electron localization in Ti_2C. ELF outputs from VASP were used for visualization and assessment of localized electron density, while BadELF was used to partition and analyze localization in vacancy and interstitial sites. These calculations were applied to ordered and disordered Ti_2C configurations. Additional details are provided in Chapter 5.

2.3 Synthetic Methods

Through my doctoral work, I have developed synthesis methods for two materials: ternary metal fluoride $NaVF_4$ and transition metal carbide Ti_2C. All synthesis was performed under inert atmosphere in an Ar-filled glovebox unless otherwise stated. Phase analysis of all

synthesized products was performed by powder X-ray diffraction with Rietveld refinement as described in Section 2.4.

Several solid-state synthesis techniques are shared across both material systems and are described here.[25,26] Reactant powders were pressed into pellets using a 6 mm die at 1.5–2 metric tons for approximately 60 seconds. Pelletization maximizes grain-to-grain contact between reactant particles, improving solid-state reaction kinetics by reducing diffusion distances. Pellets were wrapped in containment foil (the choice of which is system-specific and discussed in each synthesis section), loaded into a quartz tube under Ar, and transferred to a vacuum line for sealing. The tube was evacuated to ~1.3×10^{-2} mbar and heated with an H_2/O_2 torch up and down the length for 2-3 minutes to evaporate any residual moisture in the tube. The tube is then sealed via torching. The sealing technique is delicate because the tube interior is under vacuum, so heating any one spot too aggressively will cause the softened quartz to collapse inward and puncture. The torch must be moved slowly and evenly around the full circumference of the tube, applying gentle heat from all sides. A useful indicator is that any visible warping of the quartz means heat should be removed from that spot immediately. This piecewise approach is continued until all inner walls are in contact and the tube can be bent off cleanly. The sealed ampule was then placed in a tube furnace for annealing.

2.3.1 Synthesis of $NaVF_4$

$NaVF_4$ was identified as a prototype experimental target from the cathode screening project described in Chapter 3. Among the 47 ABF_6 cathode pairs, the Na-V-F system was selected based on three criteria: (1) both the charge and discharge states lie on the ternary hull with favorable formation energies ($NaVF_6$, charged state, $\Delta H = -104$ meV/atom and $NaVF_4$, discharged state, $\Delta H = -55$ meV/atom) (2) moderate discharge voltage of 3.64 V vs. Li/LiF for the $NaVF_6 \rightarrow NaVF_4$ reaction, which falls near the middle of the ABF_6 voltage distribution and (3) cost, as NaF and VF_3 are commercially available and relatively inexpensive. The discharged

state $NaVF_4$ was targeted for initial synthesis because it is less fluorinating than the charged state $NaVF_6$ and therefore predicted to be easier to handle and characterize.

2.3.1.1 Solid State Synthesis Using Metal Fluorides

Solid state fluoride syntheses pose challenges that are less common in oxide or carbide systems because, at high temperature, trace moisture can trigger a degradation cycle where metal fluorides can react with H_2O to form metal oxide byproducts and HF. In quartz ampules, HF etches the quartz tube to produce SiF_4 and more H_2O, which can react with the original metal fluoride.[27,28] This loop accelerates with temperature and leads to loss of metal fluoride reactant and eventual failure of the quartz ampule, making control of moisture, temperature, and containment a central challenge in ternary fluoride synthesis. The standard literature synthesis of $NaVF_4$ addresses this problem by using sealed platinum ampules at 900 °C for 24 hours, since platinum is inert to HF and avoids the feedback loop entirely.[29] However, Pt ampules are prohibitively expensive for iterative optimization. A central methodological contribution of this work is showing that these costly Pt ampules can be replaced by inexpensive quartz tubes lined with graphite foil and paired with careful temperature control, making ternary fluoride synthesis more accessible to laboratories without noble-metal containment ampules.

Each $NaVF_4$ synthesis attempt was performed with a 1:1 molar ratio of NaF (Fisher Chemical, ACS grade) and VF_3 (Thermo Scientific, 98%), ~150-300 mg total, pressed into a pellet and sealed in a quartz ampule. All attempts after the first used graphite foil containment. The VF_3 reagent was used within three months of opening and stored with a taped cap in sealed HDPE bags to further minimize hydration in the glovebox.

2.3.1.2 Containment Strategy

The choice of containment foil wrapped around the pellet inside the quartz tube to act as a physical barrier between the sample and the quartz wall proved critical for $NaVF_4$ synthesis. Two containment materials were tested.

Tantalum foil was the initial choice, following the standard approach used for Y_2C and Ti_2C synthesis in the Warren lab. However, Ta reacts with VF_3 to form TaF_5, which has a boiling point of only 230 °C. At reaction temperatures of 900–1000 °C, the TaF_5 vapor pressure was extreme. In the first synthesis attempt (described below), this caused the quartz tube to burst inside the furnace. The remains showed heavily etched quartz, fully consumed Ta foil, and vanadium oxide byproducts. Tantalum foil is therefore incompatible with metal fluoride reactants.

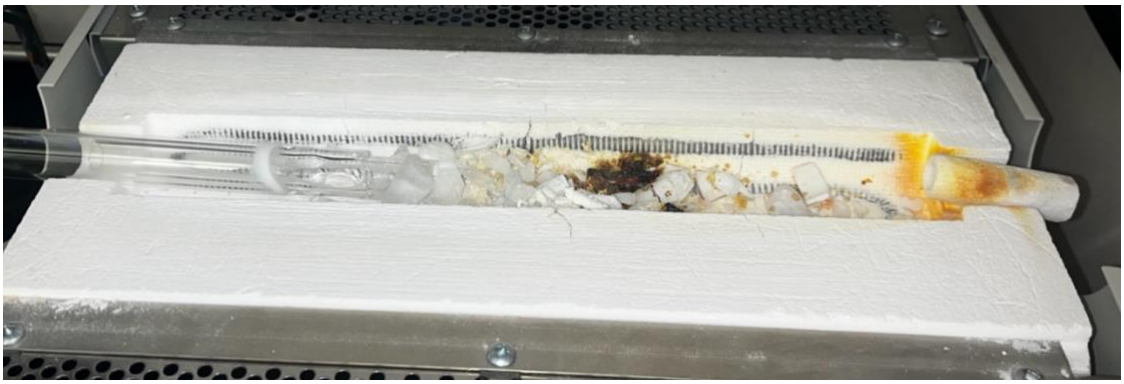


Figure 2-6. Burst quartz tube resulting from TaF_5 overpressure during $NaVF_4$ synthesis. The pellet was wrapped with Ta foil containment and heated at 1000 °C.

Graphite foil (0.13 mm thick, 99.8% metals basis, Thermo Scientific) was adopted as the replacement. Graphite is chemically inert to VF_3 at these temperatures and does not form volatile fluorides, providing an effective physical barrier between the pellet and the quartz wall. The substitution eliminated high pressure volatile fluorides and became the standard containment for subsequent $NaVF_4$ syntheses. A minor consequence is that trace carbon

contamination from the graphite foil contact surface sometimes appears in the product XRD pattern, but this does not interfere with phase identification or quantification.

2.3.1.3 Temperature Optimization

I explored a range of reaction temperatures to understand the interplay between VF_3 reactivity and the proposed HF feedback loop. At 1000 °C, the tube burst due to high TaF_5 vapor pressure as described above. At 900 °C with graphite foil, the tube showed severe quartz etching, with the interior walls no longer visible through the glass, indicating significant HF formation (Figure 2-6). The dominant products via Reitveld analysis was Na_3VF_6 and V_2O_3, consistent with a reduced ratio of available vanadium due to VF_3 loss from the system. At 750 °C, the quartz tube showed mild etching, indicating that the HF-driven degradation cycle was diminished but still present. Na_3VF_6 and V-O species remained the dominant products, suggesting that lowering the temperature helps limit attack on the quartz but does not prevent VF_3 oxidation or formation of Na-rich ternary phases. At 350 °C (4d), approximately 25% $NaVF_4$ was observed by Rietveld refinement, alongside roughly equal fractions of unreacted VF_3, V-oxide species, and Na_3VF_6. This result was demonstrated that the desired product can form at low temperatures, but VF_3 oxidation still limits yield when starting from hand-ground precursors.

These results reveal an inherent temperature tradeoff in ternary fluoride synthesis using quartz containment. Higher temperatures increase reactivity but also accelerate the HF-driven degradation cycle, causing fluorine loss, vanadium oxidation, and attack on the quartz tube. Lower temperatures suppress this cycle enough to allow some $NaVF_4$ formation, but only in limited amounts. Mechanochemical activation[30] offers a solution, where ball milling reduces the particle size of NaF and VF_3 and increases reactant surface area, improving the energetic favorability of $NaVF_4$ formation relative to VF_3 oxidation.



Figure 2-7. Temperature-dependent quartz tube etching. Heavy quartz tube etching at 900 °C (top) and reduced quartz etching at 750 °C (bottom) via HF formation from VF_3 oxidation.

2.3.1.4 Mechanochemical Activation

All ball milling was carried out in inert atmosphere using a Spex SamplePrep BM-400 mixer/mill with a 2.5 mL stainless steel jar, one 6.35 mm stainless steel ball, and a Teflon O-ring seal and taped cap, with the total precursor mass of ~150 mg per jar. We evaluated both milling cycle time and total milling time. Milling for 48 hours with 30 min on/off cycles produced a well-mixed amorphous powder, with XRD showing only broad, low-intensity peaks for VF_3 and NaF precursors. Milling for the same total duration using 4 hour on/off cycles gave similar $NaVF_4$ yields after subsequent annealing but increased glovebox temperatures by ~10 °C, so the 30-minute cycling schedule was used for better thermal management. Extending the milling duration to 72 hours provided negligible improvement over 48 hours for $NaVF_4$ formation after annealing. After milling, the amorphized powder was pressed into a pellet, wrapped in graphite foil, sealed in an evacuated quartz ampule, and annealed, at two different temperatures. Annealing at 500 °C still yielded mainly Na_3VF_6 and V_2O_3, indicating that the HF-driven degradation cycle remained active even with ball-milled precursors. Annealing at 350 °C for 4 days gave the optimal result: Rietveld refinement indicated 84–90 wt% $NaVF_4$, with only minor

graphite contamination from foil contact and trace amounts of V_2O_3 and Na_3VF_6. These results show that ball milling provides sufficient precursor activation for $NaVF_4$ formation at 350 °C on a 4-day timescale while keeping the HF feedback loop largely suppressed.

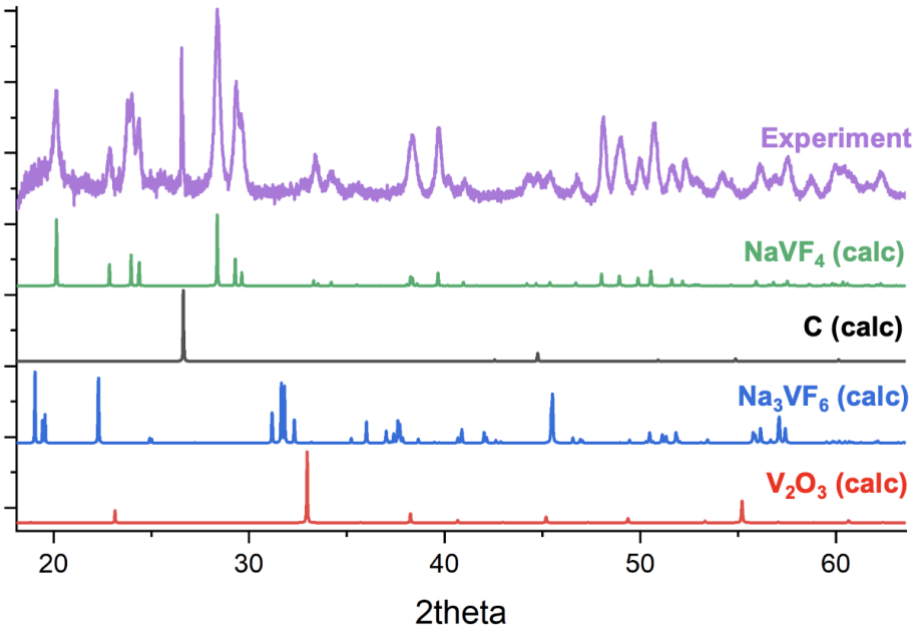


Figure 2-8. XRD pattern of the optimized $NaVF_4$ synthesis. $NaVF_4$ product (purple) shows >80% $NaVF_4$ yield with trace V-O species, Na_3VF_6, and C contamination from graphite foil.

2.3.1.5 Optimized Synthesis Protocol

The final optimized protocol for $NaVF_4$ synthesis is as follows, all under inert atmosphere:

(1) Weigh a 1:1 molar ratio of NaF and VF_3. VF_3 must have been opened within three months to avoid hydration. Total mass ~150-300 mg.

(2) Load the mixed powder into the stainless steel ball mill jar with a single 6.35 mm stainless steel ball. Seal with the Teflon O-ring and tape cap.

(3) Ball mill for 48 hours using 30 minute on/off cycle.

(4) Press the milled powder into a pellet using a 6 mm die at ~1.5–2 metric tons for 60 seconds and wrap in graphite foil.

(5) Load the wrapped pellet into a quartz tube, evacuate to ~1.3×10^{-2} mbar, and flame-seal with an H_2/O_2 torch.

(6) Anneal at 350 °C for 4 days. Heat and cool at 50 °C/hr.

(7) Open the ampule inside glovebox and grind product for PXRD characterization.

The expected product is a dark green powder consisting of ~80-90% $NaVF_4$ by weight, with minor C from graphite foil contact and trace V_2O_3 and Na_3VF_6.

2.3.2 Synthesis of Ti_2C

This section examines the synthesis of Ti_2C as a candidate FIB anode material and potential lower-cost alternative to Y_2C.[31] In the Ti–C rocksalt system, carbon can occupy the anion sublattice over a wide compositional range, but at the Ti_2C stoichiometry two structural limits are relevant. One is a disordered rocksalt (DRX) phase, in which carbon and vacancies are randomly distributed. The other is the ordered Fd-3m Ti_2C phase,[32,33] in which the carbon vacancies form an ordered three-dimensional network and produce a superstructure reflection at 17.7° 2θ. Figure X-1 shows the XRD patterns of experimental DRX and partially ordered Ti_2C samples compared to a calculated pattern for Fd-3m. This section describes efforts to synthesize fully ordered Fd-3m Ti_2C, along with preliminary hydrogenation studies on partially ordered material.

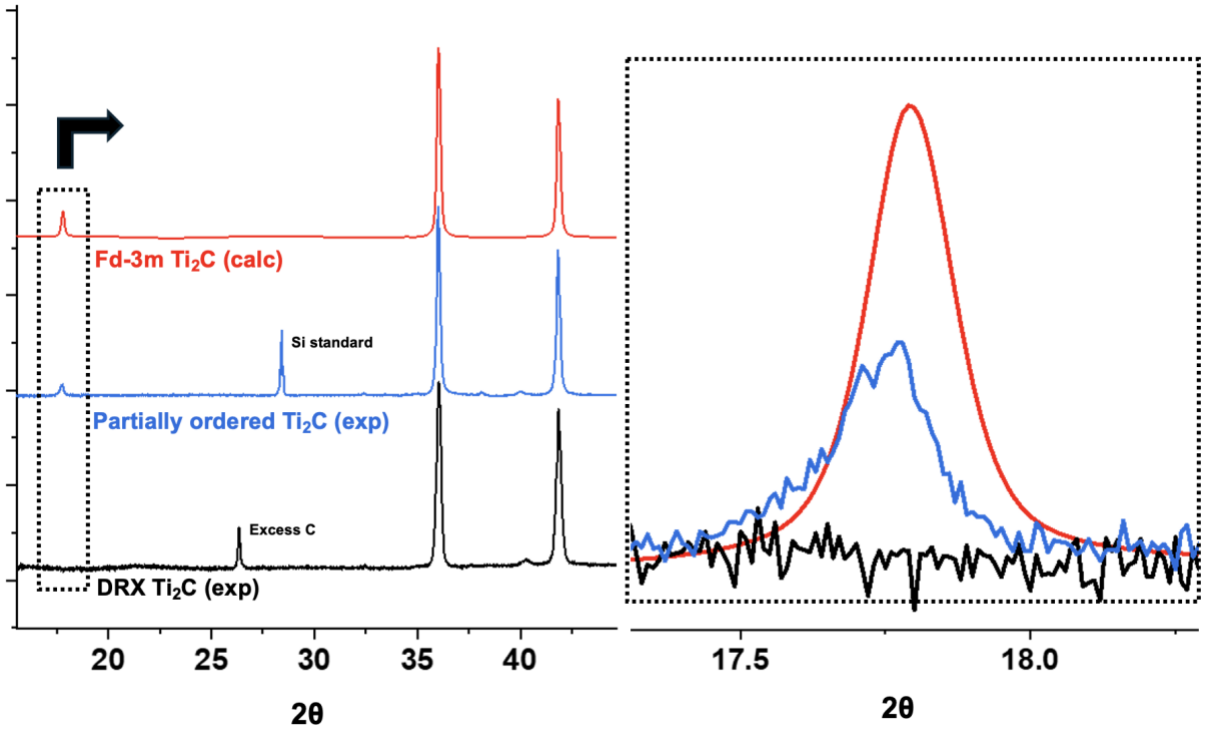


Figure 2-9. XRD patterns of Ti_2C phases. (Left) XRD pattern of experimental DRX (black), experimental partially ordered (blue), and calculated Fd-3m (red) Ti_2C patterns. (Right) Zoomed in pattern overlay of characteristic ordering peak at 17.7° 2θ

2.3.2.1 Ti_2C Procedure 1: Arc Melting

The first procedure for synthesizing Ti_2C used arc melting from Ti ingot and graphitic carbon precursors. Ti ingots (99.995–99.999% purity, 1/8” diameter by 1/8” length ingots from Kurt J. Lesker or American Elements) and graphite (flakes, ~100 mesh, Sigma Aldrich) were weighed in a glovebox, with a total mass of ~200mg and a 6–8 wt% excess of Ti included to compensate for ablation losses during melting. Because Ti ingots cannot be ground, 3-5 were typically used and the correct ratio of C was weighted out. Carbon was pressed into a pellet and the ingots/pellet were arc melted under flowing Ar using a Miller GoldStar 452 TIG welder. Each sample was typically subjected to 8 arcing events of roughly 5 seconds each, with the pellet flipped between melts to improve homogeneity. Comparison of 4-8 arcing events showed no improvement in subsequent Fd-3m conversion. XRD of the resulting product before annealing

showed formation of a DRX Ti_2C phase with residual Ti metal and no detectable Fd-3m ordering. The standard annealing profile following arc melting consisted of a 10 hr ramp to 1000 °C, a 96 hr hold at 1000 °C, and a cooldown over 42 hr with a 30 hr cool to 600 °C followed by a 12 hr step to room temperature. The slow cool time from 1000 °C to 600 °C promotes carbon ordering. This full profile required approximately 6 days. Using this method, approximately ~40% Fd-3m-like character could be achieved according to the Reitveld method described later.

2.3.2.2 Ti_2C Procedure 2: Powder Mixing

Among the optimization attempts used to increase carbon ordering, eliminating the arc-melting step was the most successful, although the improvement remained modest. Arc melting was abandoned for three main reasons. First, the arc-melted Ti–C solid solution was suspected to contain Ti- or C-rich regions, which could limit long-range carbon diffusion and hinder ordering during annealing. Second, arc melting caused substantial ablation losses (18–28%), introducing stoichiometric uncertainty despite compensation efforts. Third, it was incompatible with hydrogen-containing precursors such as TiH_2, which later proved essential for the hydrogenation experiments described in Section 2.3.3. In the no-arc-melt route, Ti powder (99.7%, 100 mesh, Strem; 99%, 325 mesh, Strem; or 99.4%, 100 mesh, Alfa Aesar) and graphite were thoroughly mixed in a mortar and pestle and pressed, wrapped (Ta foil), sealed, and annealed as described above. This approach gave slightly higher Fd-3m conversion, typically ~45–50% which we attribute to improved Ti/C reactant contact area and greater stoichiometric control.

2.3.2.3 Ti_2C Optimization Attempts

The syntheses described above represent the most successful routes to partially ordered Ti_2C. Across more than 20 distinct synthesis conditions, no alternative combination of reaction variables increased the Fd-3m fraction beyond ~40–50%. Annealing temperatures from 800 to 1200 °C, hold times from 2 to 14 days, and cooling rates from 10 to 100 °C/hr were

systematically examined, revealing that ordering develops primarily during cooling, since quenching produced no ordered phase as observed after arc melting. Additional variables, including excess Ti or C (5-20wt%), pellet mass (100-500mg), and arc-melt duration (3-15 seconds) or number of arcing events (4-8), also did not improve ordering. Efforts to manage oxygen contamination including alternative Ti precursors, sacrificial Ti pre-zapped in the arcing chamber, and CaH_2 treatment of the Ti source also failed to increase the ordered fraction. Containment studies showed that foil materials other than Ta promoted undesirable side reactions, with Zr foil degrading during annealing and graphite foil introducing carbon diffusion into the Ti–C matrix. These results support the hypothesis described in Chapter 5 that the ordering limit arises from kinetic arrest rather than incomplete synthetic optimization.

2.3.2.4 Synthesis of Layered Ti_2CH_2

Layered Ti_2CH_2 (P-3m1) was synthesized during efforts to hydrogenate partially ordered cubic Ti_2C. Because TiH_2 decomposes near 600 °C and releases H_2, a separate TiH_2 pellet was introduced into the sealed quartz ampule during the 1000 °C anneal to promote hydrogen uptake into the cubic Ti_2C product. The observation of layered Ti_2CH_2 shifted subsequent optimization toward maximizing the layered hydride fraction. The most important variable was the TiH_2:Ti–C ratio, which controls the H_2 partial pressure in the ampule. Stoichiometric TiH_2 produced ~50% layered conversion, whereas 1.5x excess TiH_2 gave the best result, yielding >90% layered Ti_2CH_2. Smaller Ti particle size (325 mesh) also improved layered conversion, consistent with faster reaction kinetics and greater surface area for hydrogen uptake.

The optimized synthesis followed the no-arc-melt Ti_2C procedure described above, with a separate TiH_2 pellet added at 1.5x excess and placed alongside the Ta-wrapped Ti_2C pellet in the quartz tube. The sealed ampule was annealed at 1000 °C for 4 days and cooled using the standard profile described above.

2.3.2.5 Dehydrogenation of Layered Ti_2CH_2

Exploratory dehydrogenation experiments were performed on layered Ti_2CH_2 to assess the reversibility of hydrogen insertion and evaluate whether the layered framework could persist after hydrogen removal, although an optimized protocol was not established. Several approaches of increasing severity were tested under vacuum (~1.3 x 10^{-2} mbar), ranging from mild heating with a heat gun to torch and furnace treatments. Mild heating via heat gun (~250 °C) on a vacuum line produced no measurable structural change, while intermediate treatments at 500 °C in a tube furnace produced small lattice contractions consistent with partial dehydrogenation, though the results were not definitive. High temperature treatments (~500-1100 °C based on Ta foil glowing via torching) led to varying degrees of conversion (~30-100%) back to DRX Ti_2C. Sustained pressure increases (~3 x 10^{-2} to 9 x 10^{-2} mbar) suggest hydrogen gas removal. These results indicate that dehydrogenation is possible but difficult to control, because hydrogen removal appears to compete with nucleation of the cubic Ti_2C phase. Thus, definitive and reliable dehydrogenation of the layered structure is an area for further optimization.[34–37]

2.4 Characterization Methods

2.4.1 Powder X-ray Diffraction and Rietveld Refinement

2.4.1.1 XRD Background and Theory

Powder X-ray diffraction (PXRD) was the primary structural characterization technique used throughout this dissertation, providing phase identification, lattice parameter determination, and quantitative phase analysis. Below is an overview of the important fitting parameters for PXRD analysis. For a comprehensive treatment of XRD theory, refer to the dissertation of my colleague Lauren McRae (Section 2.4.1).

A PXRD pattern is characterized by five fitting parameters. Peak position is determined by Bragg's law ($n\lambda = 2d \sin\theta$). With the X-ray wavelength fixed (typically Cu Kα, λ = 1.54 Å), peak positions map directly to d-spacings and form the foundation of phase identification. Peak width reflects both instrumental and sample contributions. The Scherrer equation ($\tau = K\lambda / \beta\cos\theta$) relates FWHM to crystallite domain size, but the measured width combines instrumental and sample broadening. The Caglioti equation[38] describes the angular dependence of the instrumental contribution:

$$FWHM^2 = U \tan^2\theta + V \tan\theta + W \quad (1)$$

By refining U, V, and W against a standard with negligible sample broadening, the instrument profile can be isolated and fixed during sample refinements, so that any additional broadening can be attributed to finite domain size or microstrain. This calibration is described in Section 2.4.1.3. Peak intensity is governed by the structure factor, absorption, multiplicity, and preferred orientation.[39–42] For the quantitative phase analysis described below, the scale factor is the most important intensity parameter, encoding each phase's weight fraction in a multiphase sample. Peak shape is modeled by a pseudo-Voigt function combining Gaussian (microstrain) and Lorentzian (domain size) contributions. Peak asymmetry arises from instrumental geometry and sample absorption and is parameterized in Materials Studio by NA and NB, calibrated alongside the Caglioti parameters.

2.4.1.2 Instrument Details and Sample Preparation

All PXRD patterns were collected on a Rigaku SmartLab diffractometer using Cu Kα radiation (λ = 1.54 Å) in Bragg–Brentano geometry. Data were collected in one-dimensional scan mode at a scan rate of 0.01°/sec. For $NaVF_4$ samples, a 2θ range of 18–70° was used; for Ti_2C samples, a range of 14–80° was used, with the lower bound set to capture the Fd-3m superstructure peak at ~17.7°.

Sample preparation differed between the two material systems. For $NaVF_4$, powder was prepared by hand grinding in an agate mortar and pestle inside the glovebox. $NaVF_4$ is not a particularly hard material, and approximately 5 minute of grinding was sufficient to obtain a fine, uniform powder. The powder (30–100 mg) was loaded into a quartz zero-background sample holder and leveled to minimize texture. Kapton tape was applied over the sample inside the glovebox to prevent oxidation during the scan. The Kapton tape introduces a broad amorphous scattering feature centered near 20° 2θ, but this does not interfere with $NaVF_4$ phase identification because all major identifying peaks for $NaVF_4$ and its relevant secondary phases (Na_3VF_6, NaF, VF_3, V-O species) lie outside this region.

For Ti_2C, sample preparation required more effort and a different approach to atmospheric protection. Arc-melted Ti_2C pellets are extremely hard and cannot be directly ground in a mortar and pestle. Each pellet (~200 mg) was first broken into 5–6 pieces using a chisel and steel well, a process that typically took approximately 10 minutes. One piece at a time was then transferred to a larger agate mortar and pestle for grinding. The first stage of grinding, approximately 10 minutes, reduces the fragments until they are no longer visibly shiny. An additional 5 minutes of grinding further reduces particles to an acceptable size for quantitative refinement. Remaining pieces were stored unground to minimize surface oxidation until needed.

Unlike $NaVF_4$, the Ti_2C system cannot be scanned under Kapton tape because the diagnostic Fd-3m superstructure peak at ~17.7° falls directly within the Kapton amorphous background, making it impossible to distinguish from the tape signal. To evaluate whether scanning in air was acceptable, I collected comparison patterns of the same Ti_2C sample with and without Kapton tape and found no significant change in peak intensities over the scan duration. This indicates that while the sample likely forms a thin passivation oxide layer upon air exposure, this process does not measurably affect the bulk diffraction pattern on the timescale

of a single scan. Based on this result, the standard protocol for Ti_2C was to transfer the ground powder (30–100 mg) into a scintillation vial inside the glovebox, seal the vial in an HDPE plastic bag under Ar, transport it to the diffractometer, and then open the bag and vial immediately before scanning. This minimizes the total air exposure to the time required for sample loading and data collection.

2.4.1.3 Rietveld Refinement and Quantitative Phase Analysis in Materials Studio

The Rietveld refinements and quantitative phase analysis (QPA) presented in this dissertation were performed using the Reflex module in Materials Studio. For straightforward systems such as $NaVF_4$, where the target phase and potential secondary phases (Na_3VF_6, NaF, VF_3, V-O species) have distinct, non-overlapping primary peaks, standard Rietveld refinement is sufficient for phase identification and approximate quantification. The Ti_2C system, however, presents a more challenging refinement problem that required the development of a systematic workflow described below.

2.4.1.3.1 The Refinement Problem

The two Ti_2C phases of interest, disordered rocksalt (DRX, Fm-3m) and ordered Ti_2C (Fd-3m), share the same titanium sublattice and differ only in the arrangement of carbon atoms and vacancies on the anion sublattice. Consequently, all major diffraction peaks are common to both phases. The strongest reflections at ~36° and ~42° 2θ are nearly identical in both structures. The only unique crystallographic signature of the Fd-3m phase is a superstructure peak at ~17.7° 2θ, which arises from the long-range ordering of carbon vacancies. This peak is intrinsically weak compared to the shared peaks, making it a sensitive but challenging diagnostic for ordering.

In a two-phase Rietveld model, the refinement must distribute intensity at the shared 36° and 42° peaks between the two Ti_2C phases while simultaneously fitting the weak 17.7° peak to

the Fd-3m phase alone. When all refinement parameters (instrument broadening, lattice parameters, crystallite sizes) are adjusted simultaneously (standard practice for well-separated phases) the optimizer has too many degrees of freedom. The fit is dominated by the intense shared peaks, and the refinement typically converges to a local minimum in which one phase captures nearly all of the 36°/42° intensity while the 17.7° peak is fit poorly or absorbed into the background (Figure 2-9). The result is a mathematically acceptable fit (low residuals at the dominant peaks) but a physically incorrect phase assignment.

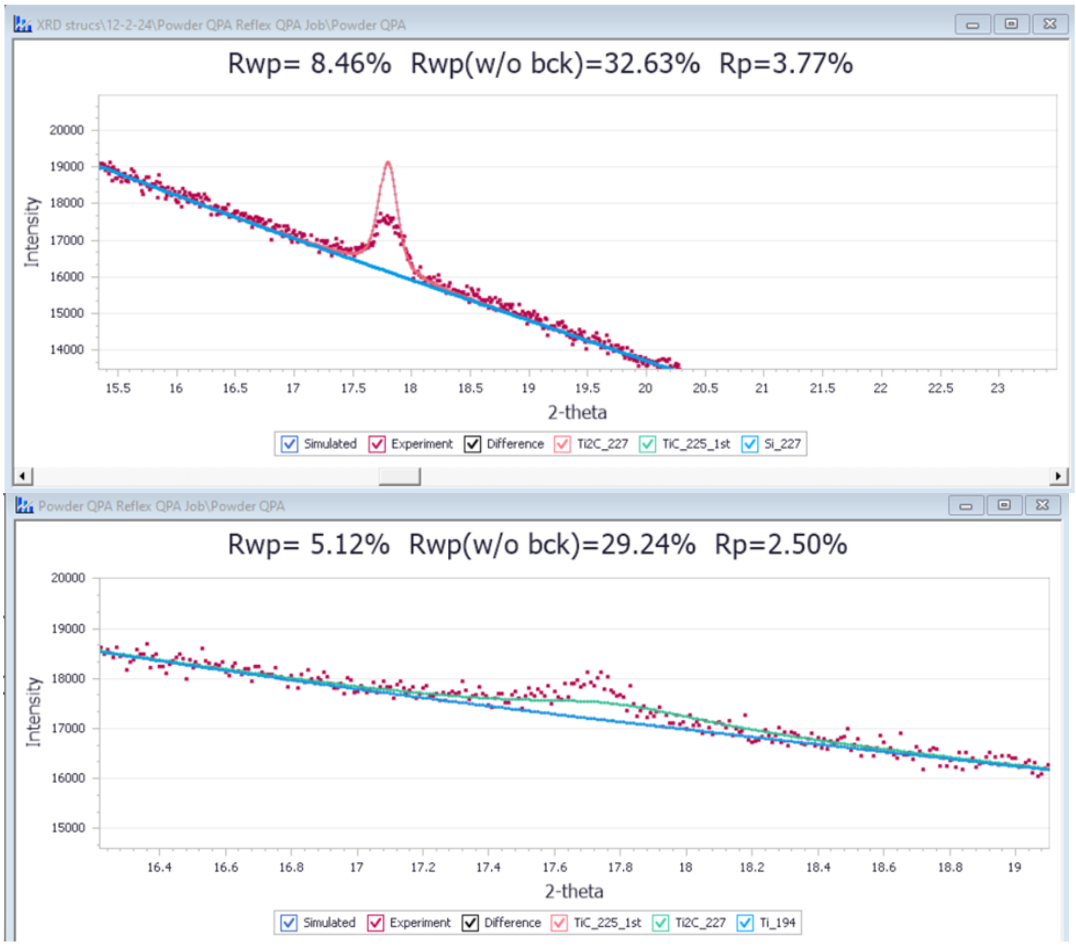


Figure 2-10. Examples of poor two-phase Rietveld refinements for Ti_2C. The top shows overfitting and the bottom shows underfitting of the 17.7° superstructure peak when refinement parameters are not properly constrained.

It is also important to note a conceptual limitation of the two-phase model itself. The Rietveld approach assumes that two spatially distinct phases coexist, where some regions of the sample are 100% Fd-3m and others are 100% DRX. The more physically accurate description, supported by the cluster expansion analysis presented in the Results chapter, is a single continuous phase with a partially ordered carbon sublattice. Traditional Rietveld methods cannot model this continuum. The weight fractions extracted from the two-phase model should therefore be interpreted as a relative ordering metric for comparing synthesis conditions rather than as a claim about the spatial distribution of fully ordered and fully disordered domains.

2.4.1.3.2 Instrument Broadening Calibration with Si Standard

Before refining any Ti_2C sample, the instrumental broadening profile must be calibrated against a standard material with negligible sample broadening. We used the NIST Si 640d standard for this purpose. As described in Section 2.4.1.1, the Caglioti equation parameterizes the angular dependence of instrumental peak broadening through the parameters U, V, and W, while the peak asymmetry is described by the parameters NA and NB. In the Materials Studio Reflex Powder Refinement module, these five parameters were refined against the Si standard pattern to isolate the instrument contribution.

In early refinements, I freely refined U, V, and W directly against Ti_2C data without first calibrating against the Si standard. This produced wildly inconsistent Caglioti values and, consequently, unphysical domain size estimates on the order of ~10,000 nm. Independent FWHM analysis of the same Ti_2C peaks using the Scherrer equation yielded expected domain sizes of 50–120 nm, confirming that the freely refined Caglioti parameters were absorbing sample broadening into the instrument profile. After calibrating against the Si standard and fixing U, V, and W in subsequent Ti_2C refinements, the extracted domain sizes fell in the 80–120 nm range, consistent with the independent Scherrer analysis.

The calibrated values used in all subsequent Ti_2C refinements were U = 0.0221, V = −0.019, W = 0.00757 (Table 2-3). These values fall within the typical ranges for a well-aligned laboratory diffractometer (U: 0 to 0.1; V: −0.1 to 0.1; W: 0.001 to 0.02), confirming that the calibration is physically reasonable. The small positive value of U indicates modest angular-dependent broadening at high angles, the negative V partially compensates at intermediate angles, and the small W reflects the baseline instrumental width at low angles. Together, these produce a smooth, monotonically increasing FWHM curve with angle, consistent with the expected behavior of a Bragg–Brentano diffractometer.

Caglioti parameter	Si standard calibrated value
U	0.0221
V	-0.019
W	0.00757

Table 2-3. Calibrated U, V, W, values in the Materials Studio Reflex refinement window from Si standard refinement.

2.4.1.3.3 Single-Phase Preliminary Refinements

With the instrument profile calibrated, the next step is to refine each Ti_2C phase individually against the experimental pattern before performing the two-phase QPA. This preliminary step provides reliable starting values for lattice parameters and domain sizes and saves the refined profile to the CIF file. This way, the QPA module inherits pre-refined initial conditions rather than starting from scratch which aids in converging to more physically correct refinements.

Two structural models are imported into Materials Studio as CIF files. The DRX phase uses the TiC rock salt structure (Fm-3m) with the carbon site occupancy set to 0.5 to represent the Ti_2C stoichiometry. The ordered phase uses the Fd-3m Ti_2C superstructure. Both CIF files, along with the raw experimental pattern, are copied into a new project folder before refinement begins. This file management practice ensures that unrefined originals remain available for fresh refinement attempts and avoids confusion about which CIFs carry refined parameters.

Each single-phase refinement follows the same general procedure within the Reflex Powder Refinement module. On the Setup tab, the refinement type is set to Rietveld at medium quality, and the 2θ range is specified. On the Radiation tab, the source is set to X-ray with λ = 1.54 Å (Cu) and $K\alpha_2$ is included. On the Pattern tab, U, V, and W are fixed to the Si-calibrated values. The experimental pattern is loaded on the Experimental Data tab. Refinement is then performed by clicking Refine (as opposed to Calculate, which performs a faster but less rigorous calculation useful for troubleshooting). Quality targets of R_wp < 10% and R_p < 6% were used as indicators of an acceptable fit.

For the DRX phase, lattice parameters, domain size, and carbon occupation are refined simultaneously. Refined carbon occupation values typically fall in the range of ~0.5–0.6. This imprecision reflects the inherently poor X-ray sensitivity to carbon occupation given the large scattering factor disparity between Ti and C. In practice, the choice between manually fixing the occupation at 0.5 and using the refined value of ~0.55–0.60 changes the final QPA weight percent assignment by only 2–3%, so refined values were used without significant concern. The refined profile is saved to the CIF file.

For the Fd-3m phase, the same parameters are refined. After refinement, the calculated pattern at 17.7° should show higher intensity than the experimental pattern at that position, because the single-phase model assigns all superstructure intensity to this phase without accounting for the DRX contribution to the rest of the pattern. This overshoot is expected and will be corrected in the QPA step, which scales each phase's contribution to match the experimental data. If the Si internal standard is also present in the sample (used for peak position calibration in hydrogenation experiments), it is refined as a third single-phase model using the same procedure.

2.4.1.3.4 Quantitative Phase Analysis

With reliable single-phase profiles established, the two (or three, if Si is included) pre-refined CIF files are loaded as separate phases into the Reflex Powder QPA module for simultaneous refinement against the experimental pattern (Figure 2-11). QPA distributes the intensity at the shared 36° and 42° peaks between the DRX and Fd-3m phases while fitting the 17.7° peak exclusively to the Fd-3m phase, thereby determining the relative weight fractions of each phase.

The QPA setup proceeds as follows. On the Phases tab, each pre-refined CIF is imported as a new phase. It is critical that these are the refined CIFs from the preliminary single-phase step, not the original unrefined files; the refined CIFs carry the optimized lattice parameters, domain sizes, and profile shapes that provide the QPA with physically meaningful starting conditions. On the Experimental Data tab, the experimental pattern is selected and the background is fit using the default polynomial of order 20, which is sufficient to describe both the baseline and any broad amorphous features. The Job Control tab defaults are acceptable. Before clicking Refine, it is important to verify that the QPA window is the active window in Materials Studio; if a different window is active, the Refine button will be grayed out.

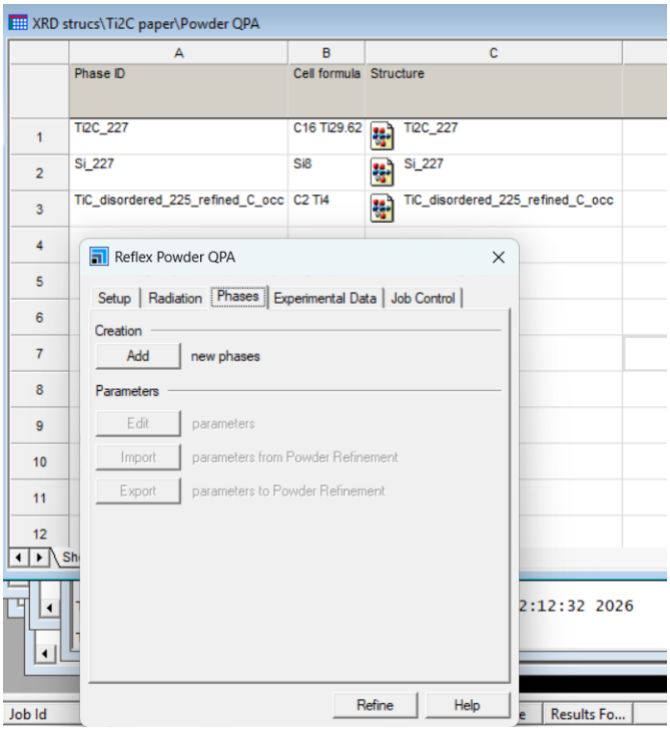


Figure 2-11. QPA phase table in Materials Studio. This shows the imported DRX, Fd-3m, and Si standard phases added through the Reflex Powder QPA Phases tab.

The QPA module produces several outputs. The Powder QPA summary (accessed via the chart icon) reports the integrated intensity, intensity percentage (before atomic scale factor corrections), and weight percentage for each phase (Figure 2-12 (top)). The weight percentage is the primary metric used throughout this dissertation because it accounts for differences in formula weight and unit cell volume between phases. The Powder QPA pattern (accessed via the bar chart icon) displays the experimental pattern, the total simulated pattern, the difference curve, and the individual intensity contribution from each phase. This pattern view is the key diagnostic for assessing refinement quality (Figure 2-12 (middle)).

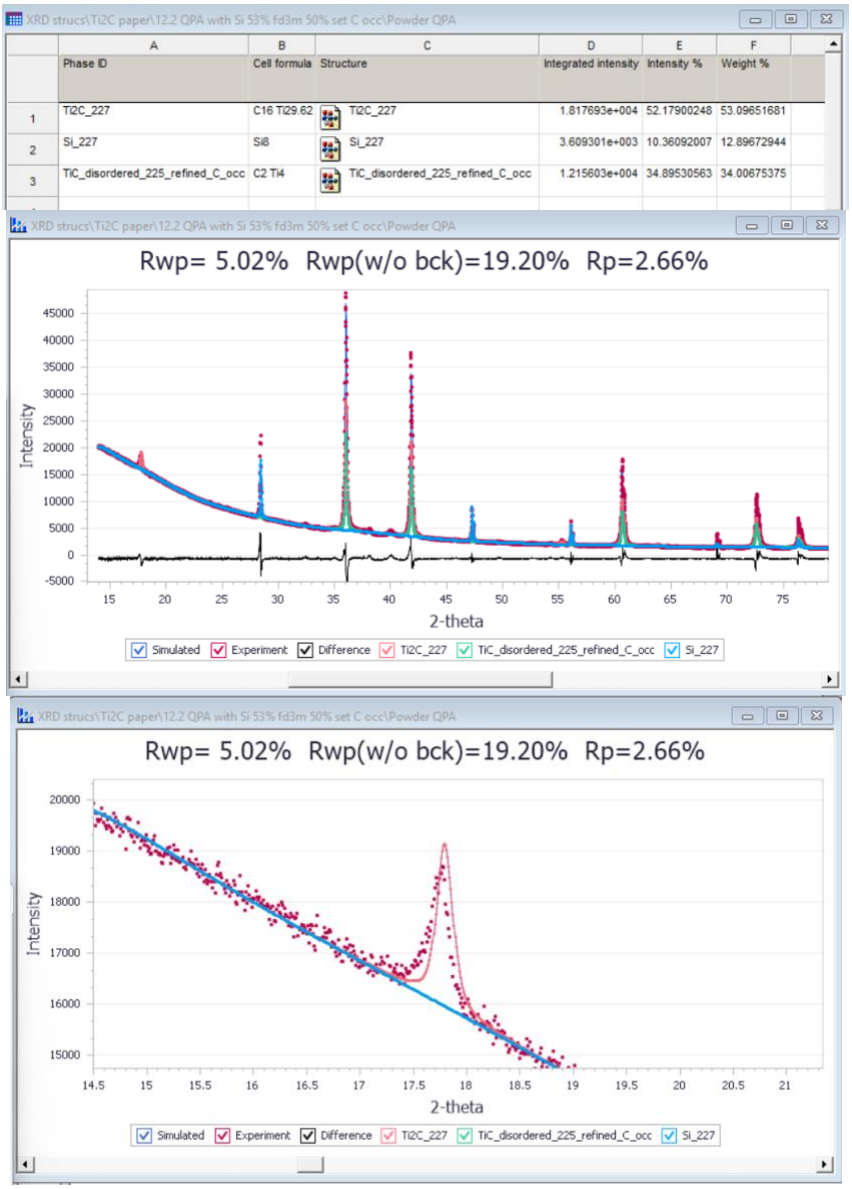


Figure 2-12. Results of advanced Rietveld refinement. QPA weight fraction (top) and pattern fitting (middle/bottom) results for a representative Ti_2C sample, showing the DRX, Fd-3m, and Si weight assignments.

The most important quality check after every QPA refinement is to inspect the fit at 17.7°. The Fd-3m phase should contribute a calculated peak at this position that closely matches the experimental intensity (Figure 2-12 (bottom)). If the calculated Fd-3m intensity at 17.7° is significantly lower than the experimental peak, the QPA is underestimating the Fd-3m fraction, potentially because the background polynomial is absorbing the superstructure peak or

because the starting lattice parameters were insufficiently refined. If the calculated intensity exceeds the experimental peak, the Fd-3m fraction is being overestimated. In either case, the single-phase preliminary refinements should be revisited before rerunning QPA. Additionally, the difference curve across the full pattern should be inspected for systematic residuals at the shared 36° and 42° peaks, which would indicate that the intensity distribution between phases needs further adjustment.

2.4.1.4 Materials Studio Navigation and File Management

The Materials Studio interface for Reflex refinement and QPA is not always intuitive, and several aspects of the workflow can cause confusion for new users. The following practical notes reflect lessons learned during the development of this refinement protocol.

File management is essential. A new project folder should be created for each experimental pattern to be refined. Unrefined CIF files should be copied into this folder before beginning refinement, so that the originals remain available for fresh attempts. The QPA module produces numerous output files in its own subfolder; keeping all files associated with a single pattern localized within one folder prevents the project tree from becoming unmanageable over the course of a multi-sample campaign.

The workflow must proceed in the correct order. Single-phase Powder Refinements are always performed first, followed by Powder QPA. The QPA module relies on the refined profiles saved to the CIF files during the single-phase step. If unrefined CIFs are loaded into QPA, the starting conditions will be poor and the refinement is unlikely to converge to a physically reasonable result.

Finally, Materials Studio has a strict active-window requirement that can be a source of frustration. The specific CIF file being refined must be open and active (in the foreground) for the Powder Refinement settings to be accessible. Similarly, the experimental pattern must be

open and active when configuring the Experimental Data tab. If the wrong window is active, key refinement options will appear grayed out with no explanatory error message. Verifying the active window before each configuration step avoids this issue.

REFERENCES

(1) Sundberg, J. D.; Benjamin, S. S.; McRae, L. M.; Warren, S. C. Simmate: A Framework for Materials Science. *J. Open Source Softw.* **2022**, *7* (75). https://doi.org/10.21105/joss.04364.

(2) Jain, A.; Ong, S. P.; Hautier, G.; Chen, W.; Richards, W. D.; Dacek, S.; Cholia, S.; Gunter, D.; Skinner, D.; Ceder, G.; Persson, K. A. Commentary: The Materials Project: A Materials Genome Approach to Accelerating Materials Innovation. *APL Mater.* **2013**, *1* (1). https://doi.org/10.1063/1.4812323.

(3) Ong, S. P.; Richards, W. D.; Jain, A.; Hautier, G.; Kocher, M.; Cholia, S.; Gunter, D.; Chevrier, V. L.; Persson, K. A.; Ceder, G. Python Materials Genomics (Pymatgen): A Robust, Open-Source Python Library for Materials Analysis. *Comput. Mater. Sci.* **2013**, *68*, 314–319. https://doi.org/10.1016/j.commatsci.2012.10.028.

(4) Urban, A.; Seo, D. H.; Ceder, G. Computational Understanding of Li-Ion Batteries. *NPJ Comput. Mater.* **2016**, *2*. https://doi.org/10.1038/npjcompumats.2016.2.

(5) Nowroozi, M. A.; Ivlev, S.; Rohrer, J.; Clemens, O. La2CoO4: A New Intercalation Based Cathode Material for Fluoride Ion Batteries with Improved Cycling Stability. *J. Mater. Chem. A Mater.* **2018**, *6* (11), 4658–4669. https://doi.org/10.1039/c7ta09427b.

(6) Aydinol, M K., Kohan, A F, Ceder, G. Ab Initio Calculation of the Intercalation Voltage of Lithium-Transition-Metal Oxide Electrodes for Rechargeable Batteries. *J. Power Sources* **1997**, *68* (2), 664–668.

(7) Aydinol, M. K.; Kohan, A. F.; Ceder, G.; Cho, K.; Joannopoulos, J. Ab Initio Study of Lithium Intercalation in Metal Oxides and Metal Dichalcogenides. **1997**, *56* (3), 1354–1365.

(8) Wang, A.; Kingsbury, R.; McDermott, M.; Horton, M.; Jain, A.; Ong, S. P.; Dwaraknath, S.; Persson, K. A. A Framework for Quantifying Uncertainty in DFT Energy Corrections. *Sci. Rep.* **2021**, *11* (1). https://doi.org/10.1038/s41598-021-94550-5.

(9) Jain, A.; Hautier, G.; Ong, S. P.; Moore, C. J.; Fischer, C. C.; Persson, K. A.; Ceder, G. Formation Enthalpies by Mixing GGA and GGA + U Calculations. *Phys. Rev. B Condens. Matter Mater. Phys.* **2011**, *84* (4), 1–10. https://doi.org/10.1103/PhysRevB.84.045115.

(10) Horton, M. K.; Dwaraknath, S.; Persson, K. A. Promises and Perils of Computational Materials Databases. *Nat. Comput. Sci.* **2021**, *1* (1), 3–5. https://doi.org/10.1038/s43588-020-00016-5.

(11) Wang, L.; Maxisch, T.; Ceder, G. Oxidation Energies of Transition Metal Oxides within the GGA+U Framework. *Phys. Rev. B Condens. Matter Mater. Phys.* **2006**, *73* (19), 1–6. https://doi.org/10.1103/PhysRevB.73.195107.

(12) Grindy, S.; Meredig, B.; Kirklin, S.; Saal, J. E.; Wolverton, C. Approaching Chemical Accuracy with Density Functional Calculations : Diatomic Energy Corrections. **2013**, *075150* (February), 1–8. https://doi.org/10.1103/PhysRevB.87.075150.

(13) Sundberg, J. D.; Druffel, D. L.; McRae, L. M.; Lanetti, M. G.; Pawlik, J. T.; Warren, S. C. High-Throughput Discovery of Fluoride-Ion Conductors via a Decoupled, Dynamic, and Iterative (DDI) Framework. *NPJ Comput. Mater.* **2022**, *8* (1). https://doi.org/10.1038/s41524-022-00786-8.

(14) Sundberg, J. D.; Druffel, D. L.; McRae, L. M.; Lanetti, M. G.; Pawlik, J. T.; Warren, S. C. High-Throughput Discovery of Fluoride-Ion Conductors via a Decoupled, Dynamic, and Iterative

(DDI) Framework. *NPJ Comput. Mater.* **2022**, *8* (1). https://doi.org/10.1038/s41524-022-00786-8.

(15) Kresse, G.; Furthmü, J. Efficient Iterative Schemes for Ab Initio Total-Energy Calculations Using a Plane-Wave Basis Set; 1996.

(16) Valiev, M.; Weare, J. H. The Projector-Augmented Plane Wave Method Applied to Molecular Bonding. *Journal of Physical Chemistry A* **1999**, *103* (49), 10588–10601. https://doi.org/10.1021/jp9929770.

(17) Blochl, P. E. Projector Augmented-+rave Method; Vol. 50.

(18) Furness, J. W.; Kaplan, A. D.; Ning, J.; Perdew, J. P.; Sun, J. Accurate and Numerically Efficient R2SCAN Meta-Generalized Gradient Approximation. *Journal of Physical Chemistry Letters* **2020**, *11* (19), 8208–8215. https://doi.org/10.1021/acs.jpclett.0c02405.

(19) Perdew, J. P.; Burke, K.; Ernzerhof, M. *Generalized Gradient Approximation Made Simple*; 1996.

(20) Grimme, S.; Antony, J.; Ehrlich, S.; Krieg, H. A Consistent and Accurate Ab Initio Parametrization of Density Functional Dispersion Correction (DFT-D) for the 94 Elements H-Pu. *Journal of Chemical Physics* **2010**, *132* (15). https://doi.org/10.1063/1.3382344.

(21) Chang, J. H.; Kleiven, D.; Melander, M.; Akola, J.; Garcia-Lastra, J. M.; Vegge, T. CLEASE: A Versatile and User-Friendly Implementation of Cluster Expansion Method. *Journal of Physics Condensed Matter* **2019**, *31* (32). https://doi.org/10.1088/1361-648X/ab1bbc.

(22) Sanchez, J. M. Cluster Expansion and the Configurational Theory of Alloys. *Phys. Rev. B Condens. Matter Mater. Phys.* **2010**, *81* (22). https://doi.org/10.1103/PhysRevB.81.224202.

(23) Becke, A. D.; Edgecombe, K. E. A Simple Measure of Electron Localization in Atomic and Molecular Systems. *J. Chem. Phys.* **1990**, *92* (9), 5397–5403. https://doi.org/10.1063/1.458517.

(24) Weaver, S. M.; Sundberg, J. D.; Slamowitz, C. C.; Radomsky, R. C.; Lanetti, M. G.; McRae, L. M.; Warren, S. C. Counting Electrons in Electrides. *J. Am. Chem. Soc.* **2023**. https://doi.org/10.1021/jacs.3c10876.

(25) Hojo, J. *Materials Chemistry of Ceramics*; Springer Singapore, 2019. https://doi.org/10.1007/978-981-13-9935-0.

(26) Levin, E. E.; Grebenkemper, J. H.; Pollock, T. M.; Seshadri, R. Protocols for High Temperature Assisted-Microwave Preparation of Inorganic Compounds. *Chemistry of Materials* **2019**, *31* (18), 7151–7159. https://doi.org/10.1021/acs.chemmater.9b02594.

(27) Mitra, A.; Rimstidt, J. D. Solubility and Dissolution Rate of Silica in Acid Fluoride Solutions. *Geochim. Cosmochim. Acta* **2009**, *73* (23), 7045–7059. https://doi.org/10.1016/j.gca.2009.08.027.

(28) Gálvez, J. L.; Dufour, J.; Negro, C.; López-Mateos, F. Hydrolysis of Iron and Chromium Fluorides: Mechanism and Kinetics. *J. Hazard. Mater.* **2008**, *154* (1–3), 135–145. https://doi.org/10.1016/j.jhazmat.2007.10.004.

(29) Babel, B. P. D.; Mn, M. I. Die Kristallstrukturen Der Vanadium-Weberite Na2M I1 V I11 F7 (MI ' = Mn , Ni , Cu) Und von NaVF4 The Crystal Structures of the Vanadium Weberites Na2M I1 V I11 F7. *Babel* **1997**, *623*, 1614–1620.

(30) Scholz, G.; Korup, O. High-Energy Ball Milling-a Possible Synthesis Route for Cryolite and Chiolite. *Solid State Sci.* **2006**, *8* (6), 678–684. https://doi.org/10.1016/j.solidstatesciences.2006.02.036.

(31) Zhang, X.; Xiao, Z.; Lei, H.; Toda, Y.; Matsuishi, S.; Kamiya, T.; Ueda, S.; Hosono, H. Two-Dimensional Transition-Metal Electride Y2C. *Chemistry of Materials* **2014**, *26* (22), 6638–6643. https://doi.org/10.1021/cm503512h.

(32) Weinberger, C. R.; Thompson, G. B. Review of Phase Stability in the Group IVB and VB Transition-Metal Carbides. *Journal of the American Ceramic Society* **2018**, *101* (10), 4401–4424. https://doi.org/10.1111/jace.15768.

(33) Yu, X. X.; Weinberger, C. R.; Thompson, G. B. Ab Initio Investigations of the Phase Stability in Group IVB and VB Transition Metal Carbides. *Comput. Mater. Sci.* **2016**, *112*, 318–326. https://doi.org/10.1016/j.commatsci.2015.10.038.

(34) Bhaskar, A.; Muduli, R. C.; Kale, P. Prediction of Hydrogen Storage in Metal Hydrides and Complex Hydrides: A Supervised Machine Learning Approach. *Int. J. Hydrogen Energy* **2025**, *98*, 1212–1225. https://doi.org/10.1016/j.ijhydene.2024.12.121.

(35) Bai, S.; Liu, L.; Liu, C.; Xie, C. Phase-Field Insights into Hydrogen Trapping by Secondary Phases in Alloys. *Materials* **2023**, *16* (8). https://doi.org/10.3390/ma16083189.

(36) Khidirov, I. Neutron Diffraction Study of Dehydrogenation of Titanium Carbohydrides TiCxHy. *Russian Journal of Inorganic Chemistry* **2017**, *62* (4), 498–502. https://doi.org/10.1134/S0036023617040088.

(37) Chu, Y. Z.; Lau, K. C. First-Principles Study of Hydrogen Storage Application of Ti3C2Tx Monolayer MXene. *Int. J. Hydrogen Energy* **2024**, *57*, 1144–1151. https://doi.org/10.1016/j.ijhydene.2024.01.136.

(38) Caglioti, G.; Paolettit, A.; R1cc1, F. P. CHOICE OF COLLIMATORS FOR A CRYSTAL SPECTROMETER FOR NEUTRON DIFFRACTION.

(39) Ida, T.; Ando, M.; Toraya, H. Extended Pseudo-Voigt Function for Approximating the Voigt Profile. *J. Appl. Cryst* **2000**.

(40) Dollase, W. A. CORRECTION OF INTENSITIES OF PREFERRED ORIENTATION IN POWDER DIFFRACTOMETRY: APPLICATION OF THE MARCH MODEL. *J. Appl. Crystallogr.* **1986**, *19* (pt 4), 267–272. https://doi.org/10.1107/S0021889886089458.

(41) Jian, Z.; HEIING, W. The Physical Meanings of 5 Basic Parameters for an X-Ray Diffraction Peak and Their Application*; 2003; Vol. 22.

(42) Mccusker, L. B.; Von Dreele, R. B.; Cox, D. E.; Loue, D.; Scardi, P. Rietveld Re®nement Guidelines. *International Union of Crystallography Journal of Applied Crystallography J. Appl. Cryst* **1999**, *32*, 36–50.

CHAPTER 3: HIGH-THROUGHPUT SCREENING OF TERNARY FLUORIDE CATHODE MATERIALS[2]

3.1 Introduction

The Introduction chapter established that FIBs offer compelling theoretical advantages but remain at an early stage of electrode development. Most experimental cathode work has focused on a small set of binary metal fluorides, particularly BiF_3, and CuF_2, each of which faces fundamental limitations in reversibility, conductivity, or structural stability during cycling. [1–10] Meanwhile, the broader computational screening paradigm that has accelerated electrode discovery in LIB systems and beyond has not been applied to FIB cathodes.[11–18] This chapter addresses that gap by presenting the first systematic, high-throughput thermodynamic screening of ternary fluoride materials as candidate FIB cathodes.

The motivation for moving beyond binary compositions is both practical and chemical. Binary metal fluorides offer limited tunability: once the metal is chosen, the voltage, capacity, and structural behavior of the electrode are largely fixed. Ternary fluorides, which contain two elements in addition to fluorine, introduce additional compositional degrees of freedom that may allow independent optimization of voltage, ionic conductivity, structural stability, and electronic conductivity. Several ternary and quaternary oxide-fluoride cathodes have demonstrated reversible fluoride intercalation, most notably Ruddlesden-Popper phases like La_2NiO_4, but these represent isolated structural families not identified by systematic exploration.[3,19–24] With thousands of known ternary fluoride compositions cataloged in the Materials Project database,[25]

[2] Portions of this chapter reproduced with permission from McTaggart, D. H.; Sundberg, J. D.; McRae, L. M.; Warren, S. C. Assessing Ternary Materials for Fluoride-Ion Batteries. Sci. Data 2023, 10, 90.

computational screening provides a principled strategy for surveying this space before committing experimental resources.

A central challenge in screening cathode materials is not simply identifying compositions with attractive theoretical properties such as voltage or capacity. Many fluoride compositions that appear promising by some metrics will disproportionate during cycling, decomposing into thermodynamically favored side products rather than reversibly converting between charged and discharged states. This failure mode is especially important in ternary systems, where the presence of a third element opens additional decomposition pathways that do not exist in binary fluorides. A screening framework for ternary cathodes must therefore go beyond property calculation and directly evaluate the thermodynamic stability of the electrochemical conversion itself.

This chapter describes such a framework and presents the resulting dataset of thermodynamically viable ternary fluoride cathode candidates. The screening identifies 168 structure pairs that undergo direct, non-disproportionating fluorination/defluorination reactions, and analysis of these pairs reveals compositional clustering around the ABF_6 stoichiometry as a particularly promising material family. We also present an experimental case study in which $NaVF_4$ is synthesized as a prototype defluorinated ABF_6 cathode.

3.2 Results and Discussion

3.2.1 Screening Workflow

To conduct a broad screening of the design space for potential ternary fluoride cathode materials, I develop a workflow which applies a sequence of compositional and thermodynamic filters to the Materials Project database, shown in Figure 3-1. The full procedural details, including database querying methods, convex hull stability thresholds, DFT uncertainty analysis,

voltage derivations, and property calculation formulas, are described in Chapter 2. This section provides an overview of the workflow logic to follow the results presented later.

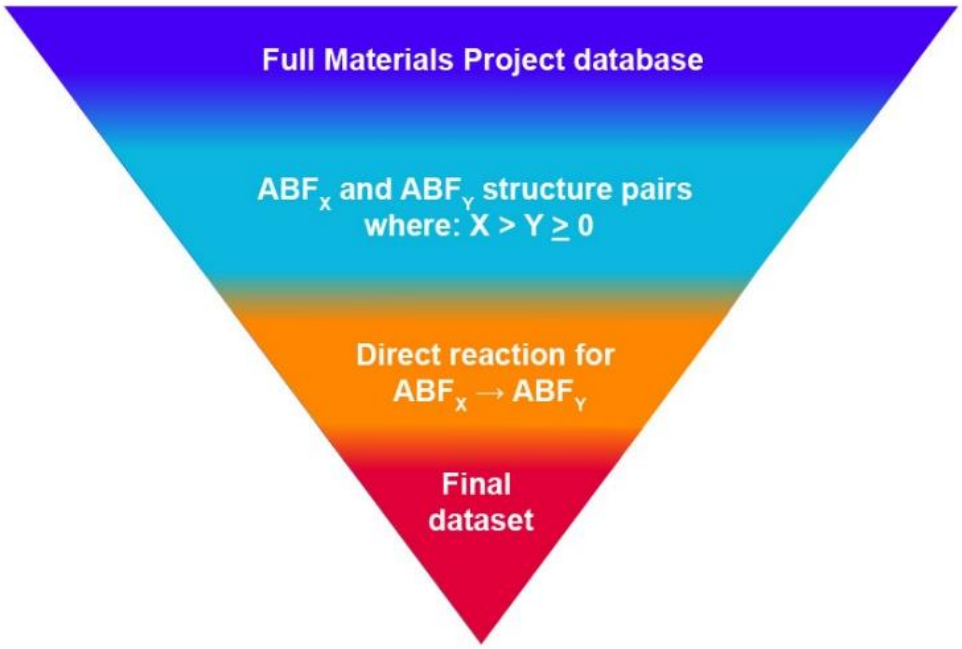


Figure 3-1. Screening workflow used to obtain the final dataset of ternary cathode material pairs.

The pipeline begins with all fluoride-containing structures in the Materials Project that have more than two elements within 75 meV/atom of the convex hull, yielding 4,389 initial entries. These form the charged (fluorinated) half of candidate cathode pairs. For each fluorinated structure, a corresponding defluorinated (discharged) partner is sought through two searches. In the complete defluorination search, fluorine is removed from the composition, and the resulting formula is matched against the database (435 matches). In the partial defluorination search, structures with the same elements and non-fluoride element ratios but lower fluorine content are identified (382 matches). Together, these produce 807 fluorinated/defluorinated structure pairs representing candidate charge/discharge reactions.

Disproportionation analysis is the most important filter in the screening workflow because it distinguishes fluorinated/defluorinated pairs that are connected by a direct thermodynamic pathway from those that decompose into non-active material side phases. In a ternary phase diagram, stable compounds appear as nodes, while tie-lines represent two-phase equilibria between them.[26] When a candidate fluorinated/defluorinated pair is identified, the key question is whether a tie-line directly connects the two compositions. If such a tie-line exists, fluoride removal can proceed as a direct reaction between those two phases alone. If no tie-line exists, then at intermediate global compositions the system will disproportionate into one or more additional phases that are thermodynamically preferred over the target pair.

This distinction is illustrated by the two examples shown in Figure 3-2. In the K–Br–F system, $KBrF_4$ and KBr are connected by a tie-line on the ternary phase diagram (Fig. 3-2a, circled in green), indicating a direct reaction between the fluorinated and defluorinated endpoints. This is reflected in the corresponding interface reaction coordinate (Fig. 3-2c), which is a straight horizontal line, showing that no lower-energy intermediate decomposition products are favored along the reaction path. By contrast, $NaBiF_4$ and NaBi are not connected by a tie-line (Fig. 3-2b; the dotted line marks where such a connection would need to exist). Instead, two other tie-lines intervene between the two endpoints. As a result, at global compositions between $NaBiF_6$ and NaBi, the system will at least partially disproportionate into NaF, BiF_3, and Bi. The interface reaction coordinate for this pair (Fig. 3-2d) confirms that these indirect reactions are thermodynamically favorable, as indicated by the drop in reaction energy per atom. Once disproportionation occurs, the formation of multiple heterogeneous phases makes it less likely that the desired charge/discharge state will fully convert even when the overall composition is correct. In a battery context, this reduces the amount of electrochemically active material impairs cyclability.

To evaluate whether each fluorinated/defluorinated pair followed a direct or indirect pathway, we used pymatgen's interface reaction function.[27] In this analysis, the fluorinated and defluorinated structures were supplied as the two reactants. If no thermodynamically favorable reaction occurred between them, the function returned the original two structures as the "products," indicating a direct reaction. If disproportionation was favored, the function instead returned the set of competing products formed along the indirect pathway. Applying this filter to the 807 fluorinated/defluorinated pairs identified 168 direct reaction pairs, which constitute the final dataset.

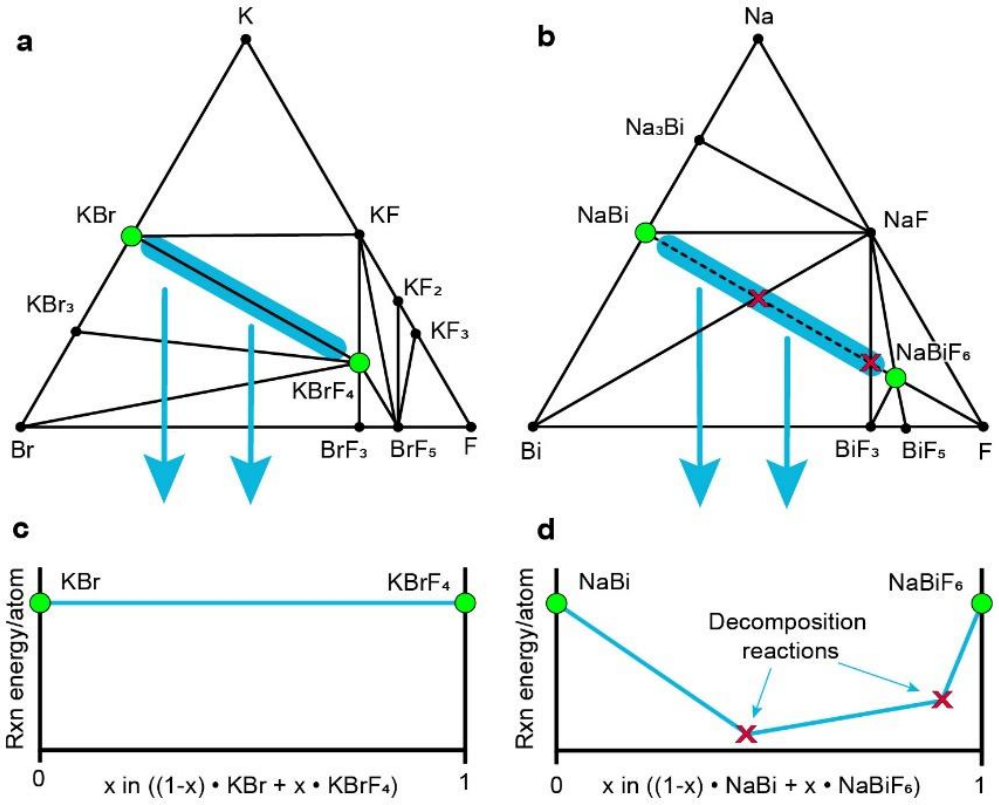


Figure 3-2. Interface reaction screening schematic. Examples of (a,c) direct and (b,d) indirect interface reactions for fluorinated/defluorinated structure pairs. In (a) there is a single tie-line connecting the fluorinated ($KBrF_4$) and defluorinated (KBr) structures. In (b) the drawn-in dotted-line between $NaBiF_6$ and NaBi crosses over the tie-lines connecting NaF/BiF_3 and NaF/Bi, leading to disproportionation to the phases on either end of the crossed tie-lines as F is removed. This is reflected in their interface reaction coordinates (c/d).

3.2.2 Final Dataset

Of the 168 direct reaction charge/discharge pairs identified, 58 are complete defluorination (14% of the original 425 complete pairs) and 110 are partial defluorination (29% of the original 382 partial pairs). The higher survival rate among partial defluorination pairs suggests that smaller fluoride ratio changes are less likely to encounter decomposition channels in the phase diagram. For each surviving pair, a collection of properties was calculated as described in Chapter 2, including voltage vs. Li/LiF, gravimetric and volumetric energy density, percent volume expansion, estimated materials cost, and, where available, fluoride transport barriers.

The 168 direct-reaction pairs span a wide range of electrochemical properties. Reduction potentials vs. Li/LiF range from −0.92 V ($Ca_5(PO_4)_3F/Ca_25(PO_4)_3$) to 5.77 V ($LiAgF_6/LiAgF_4$), with an average of 2.9 V. Gravimetric capacities range from 6.4 mAh/g ($RbSnF_3/RbSn_{2.94}$) to 758 mAh/g ($NClOF_4/NClO$), with an average of 150 mAh/g. Plotting energy density against estimated cost and coloring by volume expansion reveals the property landscape of the dataset (Figure 3-3). Most structures cluster between 100–900 Wh/kg with moderate expansion between 7–40%, and materials costs span five orders of magnitude.

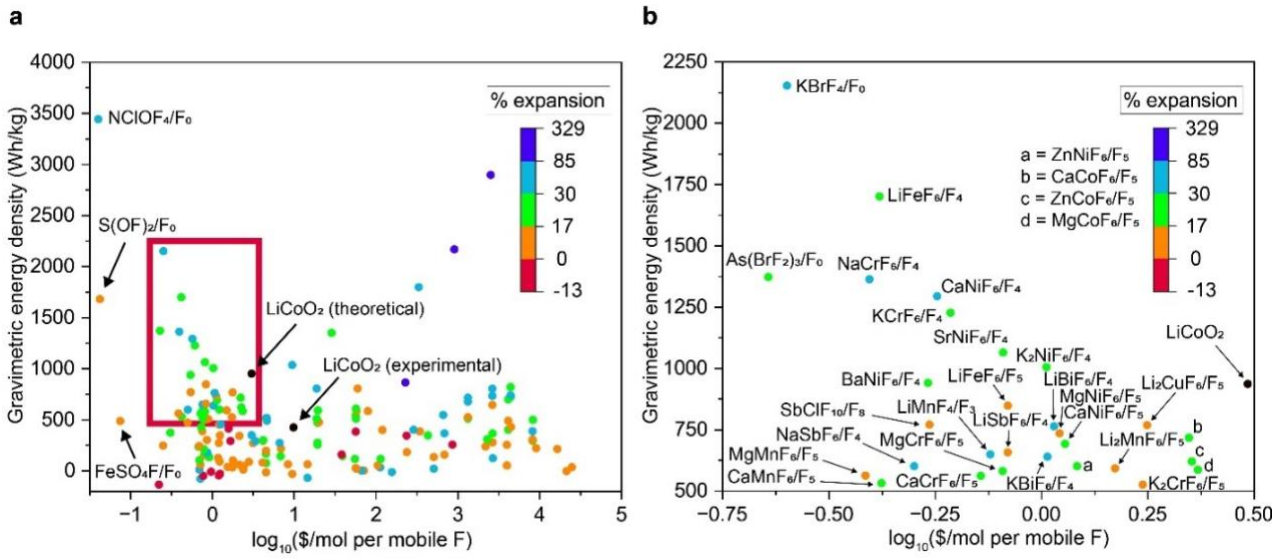


Figure 3-3. Calculated properties for direct reaction cathode pairs. Energy density (Wh/kg) vs. $\log_{10}$($/mol mobile F) for all 168 direct-reaction pairs with colorimetric scale based on percent volume expansion. Zoomed view highlighting the high energy density, low cost region with compounds labeled. $LiCoO_2$ reference values included for comparison.

Of the 168 direct-reaction pairs, 108 involve one mobile fluoride ion and 40 involve two. Only 13 pairs transfer between 3 and 6 fluoride ions, while the remaining pairs involve <1 fluoride transfer. This strong bias toward 1–2 mobile fluoride ions is consistent with the thermodynamic expectation from ternary phase diagrams: smaller compositional changes are less likely to cross intervening tie-lines and therefore more likely to remain on a direct, stable reaction pathway. In practical terms, the most viable direct-reaction cathodes are those with accessible defluorinated states separated by modest compositional changes, rather than those that require traversing large regions of the phase diagram.

The transition-metal distribution across the dataset suggests a corresponding chemical selectivity for metals that can stabilize multiple accessible oxidation states. Frequently recurring metals in the direct-reaction set include Mn, V, Cr, Ti, Fe, and Ni, consistent with the idea that stepwise defluorination is most favorable when the redox-active center can support a sequence of chemically reasonable oxidation-state changes.

Importantly, not all entries in the dataset represent practical cathode candidates. Several of the highest energy density pairs, including $NClOF_4$/NClO, $S(OF)_2$/SO_2, and $As(BrF_2)_3$/$AsBr_3$, are molecular crystals rather than extended inorganic solids. These materials are unlikely to provide the electronic conductivity, fluoride-transport pathways, or mechanical integrity required for electrode operation. Their presence is still chemically informative, since they satisfy the same thermodynamic screening criteria as the more promising inorganic compounds. Accordingly, the energy-density and cost metrics in Figure 3-3 should be interpreted as a map of favorable thermodynamics rather than as a stand-alone measure of experimental viability.

3.2.3 ABF_6 Composition

Among the compounds identified in the direct-reaction dataset, the ABF_6 family emerged as the most promising compositional class. While related stoichiometries such as A_2BF_6 and A_3BF_7 also appeared, ABF_6 compounds and their defluorinated products (ABF_5 or ABF_4) accounted for 45 of the 168 direct-reaction pairs.

This prominence is reflected in their calculated properties. Relative to the full direct-reaction dataset, the ABF_6 family showed a substantially higher average voltage versus Li/LiF (4.07 V vs. 2.91 V) and average energy density (663 Wh/kg vs. 471 Wh/kg), while maintaining a comparatively low median fluorinated-material cost ($6.24/kg vs. $25.054/kg). Median cost is reported here because the mean is strongly skewed by a small number of entries containing expensive elements such as Rb, Au, and Cs. The ABF_6 compounds therefore cluster in a favorable region of the energy density–cost landscape, while also tending to exhibit high predicted voltages. Structurally, most of the identified ABF_6 compounds adopt space groups 148 or 225, both built from corner-sharing BF_6 octahedra, a framework previously associated with relatively low fluoride migration barriers.[28]

An additional notable feature of the ABF_6 family is that several compositions display stepwise redox behavior across multiple structures, rather than only a single

fluorinated/defluorinated pair. In some cases, ABF_6, ABF_5, and ABF_4 compositions all appear as direct-reaction pairs within the same chemical family, indicating that multiple nearby fluoride contents can remain thermodynamically accessible. The Ca–Ni–F system provides one example: $CaNiF_6$/$CaNiF_5$, $CaNiF_6$/$CaNiF_4$, and $CaNiF_5$/$CaNiF_4$ all appear as direct-reaction pairs, with calculated voltages of 5.50, 5.14, and 4.78 V vs. Li/LiF, respectively. Similar behavior is also seen in the Li–Bi and Li–Fe systems. Other ABF_6 entries defluorinate to either ABF_5 or ABF_4, which is consistent with the broader trend in the dataset that direct reactions most often involve transfer of only one or two fluoride ions.

Taken together, these trends suggest that the ABF_6 family is favored not only because of its calculated voltage, energy density, and cost metrics, but also because it frequently supports chemically related and thermodynamically accessible defluorination pathways. This combination makes ABF_6 the clearest design space to emerge from the screening and provides the motivation for closer examination of specific members such as $NaVF_4$ (discharge state) in the following section.

3.2.4 Synthesis of $NaVF_4$

To test whether the computationally identified ABF_6 candidates can be experimentally realized, the $NaVF_6$/$NaVF_4$ pair was selected as a prototype synthesis target. Among the 45 ABF_6 cathode pairs in the direct-reaction dataset, the Na-V-F system was chosen based on three criteria: (1) both the charged state ($NaVF_6$, $\Delta H = -104$ meV/atom) and the discharged state ($NaVF_4$, $\Delta H = -55$ meV/atom) lie on the convex hull with favorable formation energies; (2) the predicted discharge voltage of 3.64 V vs. Li/LiF for the $NaVF_6 \rightarrow NaVF_4$ reaction falls near the middle of the ABF_6 voltage distribution, making it a representative test case; and (3) the precursors NaF and VF_3 are commercially available and relatively inexpensive. The discharged state $NaVF_4$ was targeted for initial synthesis because it is less fluorinating than $NaVF_6$, making it easier to handle and characterize.

The standard literature synthesis of $NaVF_4$ requires sealed platinum ampules.[29] While effective, this approach is prohibitively expensive for iterative optimization. A central methodological contribution of this work is the development of an alternative protocol using quartz tubes lined with graphite foil, combined with mechanochemical activation and reduced annealing temperatures, to produce $NaVF_4$ at reduced cost.

The key challenge of $NaVF_4$ synthesis using quartz containment is a feedback loop in which trace moisture reacts with VF_3 to produce HF, which etches the quartz to form SiF_4 and additional water, accelerating VF_3 oxidation and producing vanadium oxide byproducts. At 900–1000 °C this cycle was severe and reducing the temperature to 350–750 °C diminished etching but still produced predominantly Na-rich ternary phases from hand-ground precursors. The solution was ball milling NaF and VF_3 for 48 hours to produce an amorphous, well-mixed powder that, after pressing, wrapping in graphite foil, sealing under vacuum, and annealing at 350 °C for 4 days, yielded 84–90 wt% $NaVF_4$ by Rietveld refinement with only trace V_2O_3 and Na_3VF_6 impurities. These results are summarized in Table 3-1. This result confirms that at least one ABF_6-type material identified through the computational screening can be synthesized as a bulk powder using commercially available precursors. It also establishes a transferable strategy in which mechanochemical activation replaces the high temperatures and noble-metal containment that have historically made ternary fluorides difficult to access. The full experimental details, including containment strategy, temperature optimization, and ball milling parameters, are described in Chapter 2. Future work will include fluorination of $NaVF_4$ to $NaVF_6$ via electrochemical or chemical (XeF_2) methods to assess cycling behavior and compare the measured voltage to the DFT prediction of 3.64 V.

Synthesis conditions	$NaVF_4$ fraction
High T (>700 °C), no ball mill	0%
Low T (350 °C), no ball mill	26%
Low T (350 °C), 48 hr ball mill	89%

Table 3-1. Summary of experimental conditions for optimizing $NaVF_4$ synthesis.

3.3 Conclusions

In this chapter I expanded the FIB cathode design space through a high-throughput thermodynamic screening of over 5,000 ternary fluoride materials in the Materials Project database. I established a generalizable workflow for identifying fluorinated/defluorinated cathode pairs and evaluating whether those pairs can cycle through direct reaction pathways rather than decomposing through disproportionation. Applying this framework narrows the ternary fluoride design space to a final dataset of 168 thermodynamically viable material pairs.

Within this dataset, the ABF_6 compositional family emerges as the most promising material class due its favorable combination of voltage, energy density, and cost, as well as the presence of chemically related defluorination pathways in several systems. I then connected these computational predictions to experiment by developing and optimizing a low-cost synthesis route for $NaVF_4$, selected as a representative discharged-state member of the ABF_6 family. Together, these results show that high-throughput thermodynamic screening can identify chemically meaningful ternary fluoride cathode families and guide experimentally accessible targets for further FIB development. In the next chapter, I adapt this high-throughput workflow to address the compatibility of carbon conductive additives in practical electrode composites.

REFERENCES

(1) Anji Reddy, M.; Fichtner, M. Batteries Based on Fluoride Shuttle. *J. Mater. Chem.* **2011**, *21* (43), 17059–17062. https://doi.org/10.1039/c1jm13535j.

(2) Rongeat, C.; Reddy, M. A.; Witter, R.; Fichtner, M. Nanostructured Fluorite-Type Fluorides as Electrolytes for Fluoride Ion Batteries. *Journal of Physical Chemistry C* **2013**, *117* (10), 4943–4950. https://doi.org/10.1021/jp3117825.

(3) Nowroozi, M. A.; Clemens, O. Insights on the Behavior of Conversion-Based Anode Materials for Fluoride Ion Batteries by Testing against an Intercalation-Based Reference Cathode. *ACS Appl. Energy Mater.* **2018**, *1* (11), 6626–6637. https://doi.org/10.1021/acsaem.8b01630.

(4) Bhatia, H.; Thieu, D. T.; Pohl, A. H.; Chakravadhanula, V. S. K.; Fawey, M. H.; Kübel, C.; Fichtner, M. Conductivity Optimization of Tysonite-Type La1-XBaxF3-x Solid Electrolytes for Advanced Fluoride Ion Battery. *ACS Appl. Mater. Interfaces* **2017**, *9* (28), 23707–23715. https://doi.org/10.1021/acsami.7b04936.

(5) Rongeat, C.; Anji Reddy, M.; Witter, R.; Fichtner, M. Solid Electrolytes for Fluoride Ion Batteries: Ionic Conductivity in Polycrystalline Tysonite-Type Fluorides. *ACS Appl. Mater. Interfaces* **2014**, *6* (3), 2103–2110. https://doi.org/10.1021/am4052188.

(6) Rongeat, C.; Anji Reddy, M.; Diemant, T.; Behm, R. J.; Fichtner, M. Development of New Anode Composite Materials for Fluoride Ion Batteries. *J. Mater. Chem. A Mater.* **2014**, *2* (48), 20861–20872. https://doi.org/10.1039/c4ta02840f.

(7) Thieu, D. T.; Fawey, M. H.; Bhatia, H.; Diemant, T.; Chakravadhanula, V. S. K.; Behm, R. J.; Kübel, C.; Fichtner, M. CuF2 as Reversible Cathode for Fluoride Ion Batteries. *Adv. Funct. Mater.* **2017**, *27* (31). https://doi.org/10.1002/adfm.201701051.

(8) Cui, H.; Gao, X.; Guo, K.; Liu, W.; Ouyang, B.; Yi, W. Lewis Acid–Base Synergistically Enhancing Practical Composite Electrolyte for Fluoride-ion Batteries at Room Temperature. *Advanced Science* **2025**. https://doi.org/10.1002/advs.202502824.

(9) Matsuo, Y.; Inamoto, J.; Mineshige, A.; Murakami, M.; Matsumoto, K.; Hagiwara, R. Charge-Discharge Behavior of Fluorine-Intercalated Graphite for the Positive Electrode of Fluoride Ion Shuttle Battery. *Electrochem. commun.* **2020**, *110*. https://doi.org/10.1016/j.elecom.2019.106626.

(10) Nakano, H.; Matsunaga, T.; Mori, T.; Nakanishi, K.; Morita, Y.; Ide, K.; Okazaki, K. I.; Orikasa, Y.; Minato, T.; Yamamoto, K.; Ogumi, Z.; Uchimoto, Y. Fluoride-Ion Shuttle Battery with High Volumetric Energy Density. *Chemistry of Materials* **2021**, *33* (1), 459–466. https://doi.org/10.1021/acs.chemmater.0c04570.

(11) Hautier, G.; Jain, A.; Chen, H.; Moore, C.; Ong, S. P.; Ceder, G. Novel Mixed Polyanions Lithium-Ion Battery Cathode Materials Predicted by High-Throughput Ab Initio Computations. *J. Mater. Chem.* **2011**, *21* (43), 17147–17153. https://doi.org/10.1039/c1jm12216a.

(12) Kirklin, S.; Meredig, B.; Wolverton, C. High-Throughput Computational Screening of New Li-Ion Battery Anode Materials. *Adv. Energy Mater.* **2013**, *3* (2), 252–262. https://doi.org/10.1002/aenm.201200593.

(13) Aykol, M.; Kim, S.; Hegde, V. I.; Snydacker, D.; Lu, Z.; Hao, S.; Kirklin, S.; Morgan, D.; Wolverton, C. High-Throughput Computational Design of Cathode Coatings for Li-Ion Batteries. *Nat. Commun.* **2016**, *7*. https://doi.org/10.1038/ncomms13779.

(14) Xiao, Y.; Miara, L. J.; Wang, Y.; Ceder, G. Computational Screening of Cathode Coatings for Solid-State Batteries. *Joule* **2019**, *3* (5), 1252–1275. https://doi.org/10.1016/j.joule.2019.02.006.

(15) Kahle, L.; Marcolongo, A.; Marzari, N. High-Throughput Computational Screening for Solid-State Li-Ion Conductors. *Energy Environ. Sci.* **2020**, *13* (3), 928–948. https://doi.org/10.1039/c9ee02457c.

(16) Zhang, X.; Zhang, Z.; Yao, S.; Chen, A.; Zhao, X.; Zhou, Z. An Effective Method to Screen Sodium-Based Layered Materials for Sodium Ion Batteries. *NPJ Comput. Mater.* **2018**, *4* (1). https://doi.org/10.1038/s41524-018-0070-2.

(17) Zhang, Z.; Zhang, X.; Zhao, X.; Yao, S.; Chen, A.; Zhou, Z. Computational Screening of Layered Materials for Multivalent Ion Batteries. *ACS Omega* **2019**, *4* (4), 7822–7828. https://doi.org/10.1021/acsomega.9b00482.

(18) Li, W.; Han, C.; Wang, W.; Xia, Q.; Chou, S.; Gu, Q.; Johannessen, B.; Liu, H. K.; Dou, S. Stress Distortion Restraint to Boost the Sodium Ion Storage Performance of a Novel Binary Hexacyanoferrate. *Adv. Energy Mater.* **2020**, *10* (4). https://doi.org/10.1002/aenm.201903006.

(19) Nowroozi, M. A.; Laune, B. De; Clemens, O. Reversible Electrochemical Intercalation and Deintercalation of Fluoride Ions into Host Lattices with Schafarzikite-Type Structure. **2018**, 617–623. https://doi.org/10.1002/open.201800106.

(20) Nowroozi, M. A.; Ivlev, S.; Rohrer, J.; Clemens, O. La2CoO4: A New Intercalation Based Cathode Material for Fluoride Ion Batteries with Improved Cycling Stability. *J. Mater. Chem. A Mater.* **2018**, *6* (11), 4658–4669. https://doi.org/10.1039/c7ta09427b.

(21) Nowroozi, M. A.; Wissel, K.; Donzelli, M.; Hosseinpourkahvaz, N.; Plana-Ruiz, S.; Kolb, U.; Schoch, R.; Bauer, M.; Malik, A. M.; Rohrer, J.; Ivlev, S.; Kraus, F.; Clemens, O. High Cycle Life All-Solid-State Fluoride Ion Battery with La2NiO4+d High Voltage Cathode. *Commun. Mater.* **2020**, *1* (1), 1–16. https://doi.org/10.1038/s43246-020-0030-5.

(22) Mohammad, M. S.; Nowroozi Geboren In Shiraz, A. *On the Development of Intercalation-Based Cathode Materials for All-Solid-State Fluoride Ion Batteries*; 2019. https://doi.org/https://doi.org/10.25534/tuprints-00011523.

(23) Nowroozi, M. A.; Wissel, K.; Rohrer, J.; Munnangi, A. R.; Clemens, O. LaSrMnO4: Reversible Electrochemical Intercalation of Fluoride Ions in the Context of Fluoride Ion Batteries. *Chemistry of Materials* **2017**, *29* (8), 3441–3453. https://doi.org/10.1021/acs.chemmater.6b05075.

(24) Nowroozi, M. A.; Mohammad, I.; Molaiyan, P.; Wissel, K.; Munnangi, A. R.; Clemens, O. Fluoride Ion Batteries - Past, Present, and Future. *Journal of Materials Chemistry A*. Royal Society of Chemistry 2021, pp 5980–6012. https://doi.org/10.1039/d0ta11656d.

(25) Jain, A.; Ong, S. P.; Hautier, G.; Chen, W.; Richards, W. D.; Dacek, S.; Cholia, S.; Gunter, D.; Skinner, D.; Ceder, G.; Persson, K. A. Commentary: The Materials Project: A Materials Genome Approach to Accelerating Materials Innovation. *APL Mater.* **2013**, *1* (1). https://doi.org/10.1063/1.4812323.

(26) Aykol, M.; Hegde, V. I.; Hung, L.; Suram, S.; Herring, P.; Wolverton, C.; Hummelshøj, J. S. Network Analysis of Synthesizable Materials Discovery. *Nat. Commun.* **2019**, *10* (1), 1–7. https://doi.org/10.1038/s41467-019-10030-5.

(27) Ong, S. P.; Richards, W. D.; Jain, A.; Hautier, G.; Kocher, M.; Cholia, S.; Gunter, D.; Chevrier, V. L.; Persson, K. A.; Ceder, G. Python Materials Genomics (Pymatgen): A Robust,

Open-Source Python Library for Materials Analysis. *Comput. Mater. Sci.* **2013**, *68*, 314–319. https://doi.org/10.1016/j.commatsci.2012.10.028.

(28) Sundberg, J. D.; Druffel, D. L.; McRae, L. M.; Lanetti, M. G.; Pawlik, J. T.; Warren, S. C. High-Throughput Discovery of Fluoride-Ion Conductors via a Decoupled, Dynamic, and Iterative (DDI) Framework. *NPJ Comput. Mater.* **2022**, *8* (1). https://doi.org/10.1038/s41524-022-00786-8.

(29) Babel, B. P. D.; Mn, M. I. Die Kristallstrukturen Der Vanadium-Weberite Na2M I1 V I11 F7 (MI ’ = Mn , Ni , Cu) Und von NaVF4 The Crystal Structures of the Vanadium Weberites Na2M I1 V I11 F7. *Babel* **1997**, *623*, 1614–1620.

CHAPTER 4: CARBON ADDITIVE SIDE REACTIONS IN FIB ANODE COMPOSITES[3]

4.1 Introduction

Identifying thermodynamically viable cathode compositions, as described in the preceding chapter, is necessary but not sufficient for building a functional FIB electrode. Carbon conductive additives (e. g., acetylene black, carbon black, or carbon nanotubes) are ubiquitous in practical battery electrode composites, including LIBs, due to electronic resistance in pure active materials. Without conductive additives, effective electrochemical cycling is limited.[1–3]

Although carbon is typically considered an inert additive in FIB setups, recent work uncovered the unexpected oxidation of carbon, as identified via XPS measurements that showed the shift in carbon to higher binding energies.[4] Unwanted side reactions can also be observed under reducing conditions. Wissel et al.[5] studied the electrochemical topochemical reduction of $La_2NiO_3F_2$ [6,7] within a solid-state FIB, attempting to form partially defluorinated $La_2NiO_3F_{1.93}$ and La_2NiO_3F, both of which require reduction of Ni^{2+} to Ni^{+}. Remarkably, they observed only the formation of $La_2NiO_3F_{1.93}$, even though the charging plateau exceeded the theoretical capacity for forming La_2NiO_3F by a factor of four. XPS revealed that this additional capacity was accompanied by a shift in carbon to lower binding energies, suggesting that the carbon black was becoming reduced. Due to the absence of other reactants, it is likely that this reduction might result from the interaction with the metals contained within the active material and additives in contact with carbon.

A possible reduction pathway for elemental carbon involves cation intercalation. As a common example, Li inserts into graphitic carbon to form LiC_6, the desired anode reaction for LIBs. Alternatively, if the carbon lacks a layered structure, a metal carbide may result. In fact,

---

[3] Portions of this chapter reproduced with permission from McTaggart, D.; Warren, S. C.; Clemens, O. Reconsidering Anode Materials for Fluoride-Ion Batteries–The Unexpected Roles of Carbide Formation. ChemSusChem 2023, *16*, e202300486.

because a carbide can have a formal oxidation state of -4, pure carbon has a theoretical capacity of 8,934 mAh/g. Although this capacity is purely hypothetical, conventional batteries often contain 10–25 wt% carbon. Therefore, even as an additive, the capacity of carbon could exceed that of the active materials, consistent with the earlier findings.[5]

Despite this evidence, side-reactions in FIB anodes have not been previously considered. Therefore, in this work, we compare two possible anode reduction reactions that can occur by reducing a metal fluoride in the presence of carbon additives. The first is the reduction of the metal fluoride to metal; the second is the reduction of the carbon to form a metal carbide. We investigate the competing energetics of these reactions by comparing the formation energies for all elemental metals within the Materials Project database[8] that are known to exist as both a metal fluoride and a metal carbide. From these results, we identify periodic trends and derive guidelines for the choice of electron conducting additives in fluoride-ion batteries.

4.2 Results and Discussions

A typical anode composite in the discharged state normally consists of a metal fluoride MF_y, a carbon additive, and a fluoride conductor, which would be a second metal fluoride in the case of all solid-state FIBs. These materials are often intimately ground together, for example, via planetary ball milling, to keep particle sizes small to facilitate the transformation process. During the reduction process of the anode material, i.e., charging, one can consider two reactions that are in competition with each other.

$$MF_y + y\, e^- + x\, C \rightarrow M + y\, F^- + x\, C \quad (1)$$

$$MF_y + y\, e^- + x\, C \rightarrow MC_x + y\, F^- \quad (2)$$

These reactions differ with respect to the chemical species that is being reduced. For Equation (1), the reduction occurs on the metal directly, whereas for Equation (2), the reduction

occurs at the carbon and/or at the metal, depending on the difference in the electronegativities of M and C.

Equation (1) is a common conversion reaction of a metal fluoride to a metal. Its chemical and therefore electrochemical potential depends on the reductivity of the metal, represented by the Fermi energy of the metal, as well as the lattice energies of both the metal M and the metal fluoride MF_y. We acknowledge that practically, the MF_y compound with the lowest value of y is most relevant to be used as an anode material (although all MF_y compounds within 75 meV/atom of the hull were included in our considerations). To illustrate this, one can compare the potentials of FeF_2/FeF_3 and Fe/Fe_3, as a representative for MF_y/MF_{y+1} and M/MF_{y+1}. For example, before FeF_3 (total energy: −6.19 eV/atom) is reduced to metallic Fe, reduction to FeF_2 (total energy: −6.69 eV/atom) occurs at a potential of ~0.8 V higher than the potential of Fe/FeF_3.

Equation (2) is a complex reaction. To understand the potential impact of the kinetics of carbide formation, the microscopic structure becomes important. Thus, we first discuss the structure of carbon blacks as a representative additive.[9] Carbon blacks can have different degrees of crystallinity or amounts of defects, depending on the synthesis conditions that have been used for material preparation. They can be obtained from the pyrolysis of hydrocarbons and consist of regions in which sp^2 hybridized carbon layers are parallel to each other (graphite-related orientation), as well as disordered regions, even with sp^3-type or sp-type bonding. Metal insertion into the graphitic regions, similar to the lithiation of graphite, is a multistep process that occurs via staged filling of the graphitic layers. This insertion process requires a small degree of structural reorganization with mainly expansion along the c-axis but has a limited capacity per carbon atom (e.g., MC_6, see Figure 4-1a for structural depiction). For this process, the electrons are transferred to the empty states immediately above the Fermi level of graphite (Figure 4-1b).[10] The insertion of metals has been reported not only for lithium[11] and potassium[12] but also

for lanthanides (e.g., Yb and Eu) under the formation of metal inserted compounds. These materials can be prepared by heating carbon under a metal vapor for volatile lanthanides or by heating compacted powders of carbon and metal.[13]

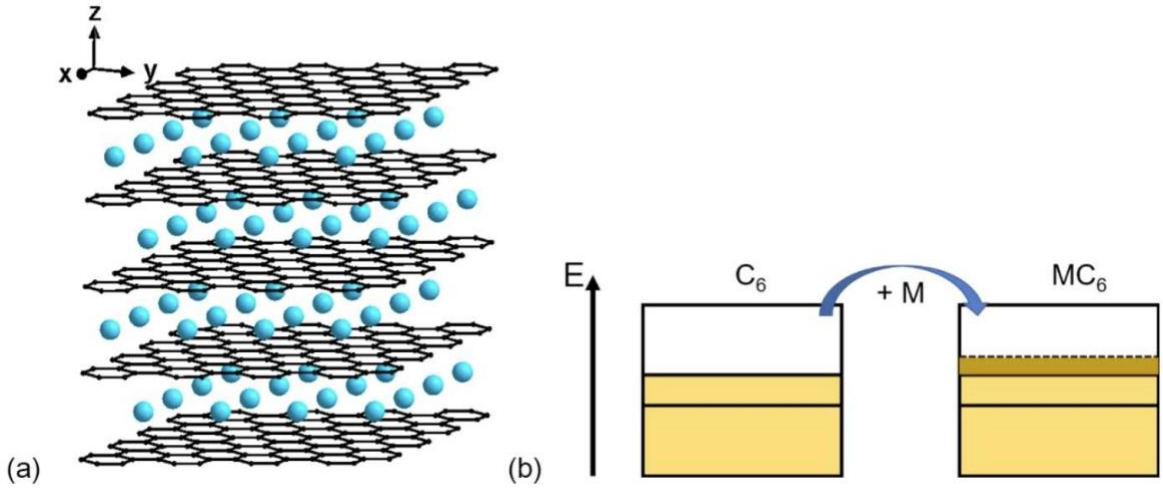


Figure 4-1. Intercalation features for some carbide materials. (a) Crystal structure of metal inserted graphite on the example of EuC_6. (b) Schematic depiction of the change in the electronic structure for M insertion into graphite.

Metal insertion into graphite might likely be favorable for kinetic reasons, and for certain metals, such carbides also represent the thermodynamically most stable product (e.g., EuC_6). However, carbon materials can also consist of regions with structures not related to graphite. For such regions, removal of carbide species under the formation of metal carbides (or nanoscopic clusters) might also be imagined, as well as the formation of surface adducts of the cationic metal species in addition to reduction of the host structure. Thus, it will also be important to consider carbide compounds such as EuC_2 [14] (see Figure 4-2a) or La_2C_3 [15] (see Figure 4-2b), which might represent the energetics of the metal cation to negatively charged carbon bonds. Similar considerations can be made for metal carbides with lower degree of ionic M–C bonding, for example, Fe_3C[16] (see Figure 4-2c).

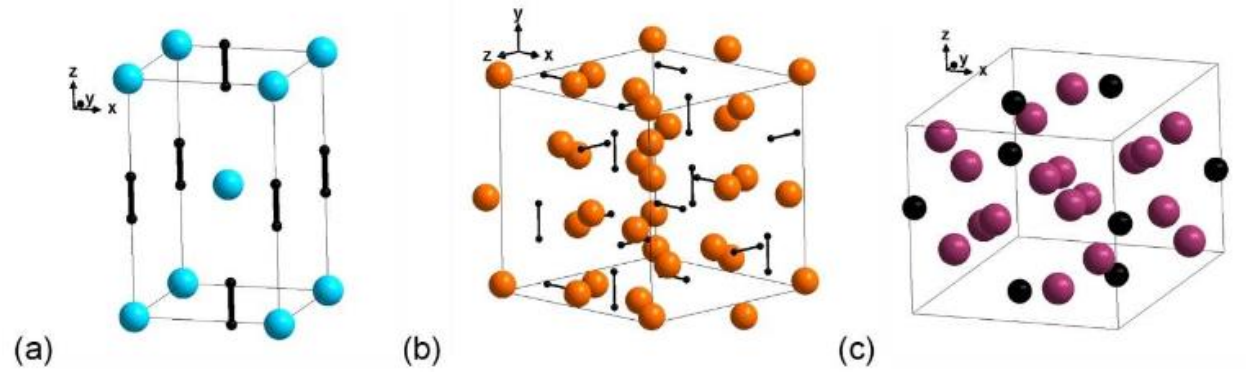


Figure 4-2. Crystal structures of several metal carbides. EuC_2 (a), La_2C_3 (b), and Fe_3C (c).

In the following, we will discuss the energetics of both reactions (Figure 4-3). Lithium is a strong reductant forming highly stable LiF and will be used as the reference for the electrochemical potentials in this work. For reacting metal fluorides with lithium, all compounds are solid; thus, one can easily conclude that these reactions must be exothermal reactions with $\Delta H_1 < 0$ eV for metals which are solid at ambient temperature. The same holds true for the carbide formation of stable metal carbides (which cannot decompose into the elements), which will also be an exothermal reaction with $\Delta H_{carb.form.} < 0$ eV. Consequently, the enthalpy of the carbon reduction coupled to metallization from MFy decomposition will be even more exothermal with $\Delta H_2 = \Delta H_1 + \Delta H_{carb.form.} < 0$ eV if a stable metal carbide exists. At this stage, we acknowledge that this is not true for all known carbides. Certain metal carbides (e.g., those of Au, Ag, and Hg) are prepared at temperatures above the melting point of the metal or via a gas phase reaction,[17–19] and their formation is only stabilized from overcoming the lattice energy of the metal, resulting in $\Delta H_{carb.form.} > 0$ eV.

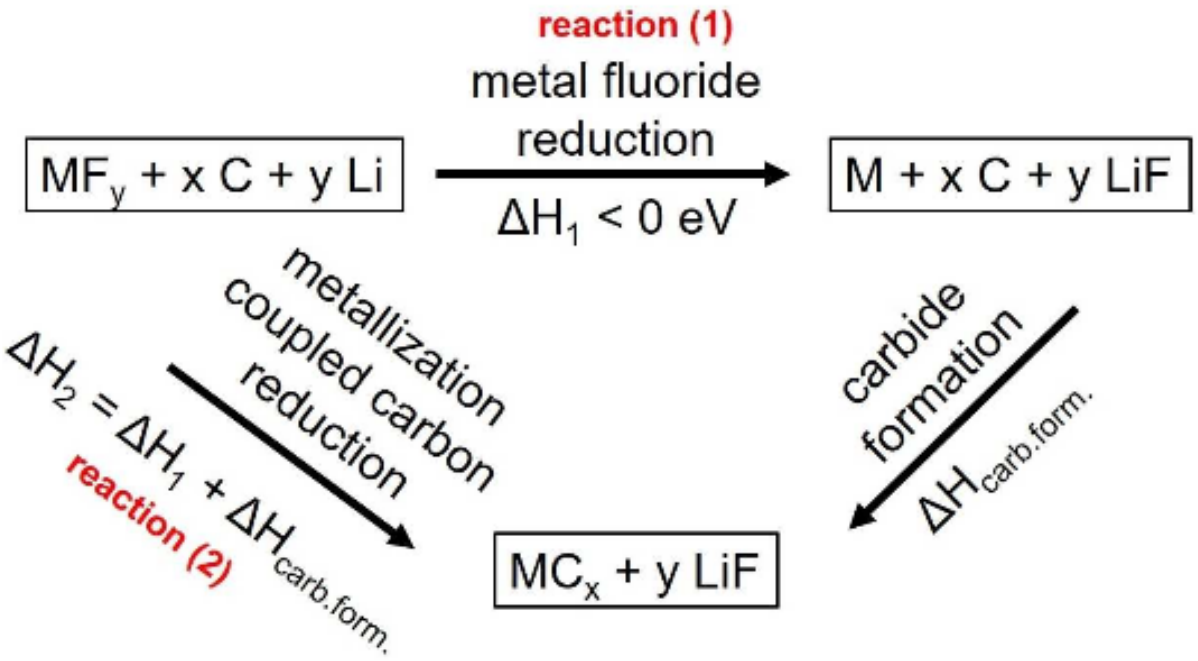


Figure 4-3. Reaction scheme of energetics comparing the metal fluoride reduction [Eq. (1)], to the metallization coupled carbon reduction, [Eq. (2)].

Neglecting entropic contributions to the free enthalpy ΔG will automatically imply that the potential $U = -\frac{\Delta G}{zF} \approx -\frac{\Delta H}{zF}$ (with *z* being the number of transferred electrons and *F* being Faraday's constant; 96,485 C/mol, see Methods chapter) can be derived from the energy difference of products and reactants or from the differences of the reaction enthalpies of Equations (1) and (2), respectively.

$$U(M/MF_Y)_{vs.\ Li/LiF} = -\frac{E(M)+yE(LiF)-yE(Li)-e(MF_y)}{y} = -\frac{\Delta H_1}{yF} \quad (3)$$

$$U(MC_x/MF_Y + xC)_{vs.\ Li/LiF} = -\frac{E(MC_x)+yE(LiF)-xE(C)-yE(Li)-e(MF_y)}{y} = -\frac{\Delta H_2}{yF} \quad (4)$$

Furthermore, one can consider the potential difference ΔU between carbon reduction and metal fluoride reduction.

$$\Delta U(MC_x - M) = U(MC_x/MF_Y + xC)_{vs.\ Li/LiF} - U(M/MF_Y)_{vs.\ Li/LiF} =$$

$$\frac{E(MC_x)+E(M)-xE(C)}{y} = -\frac{\Delta H_2-\Delta H_1}{yF} = -\frac{\Delta H_{carb.form}}{yF} \quad (5)$$

From this, we conclude the following:

(1) The carbon reduction under metal carbide formation will become thermodynamically favorable over the metal fluoride reduction (i.e., the potential of the metallization-induced carbon reduction is higher than the potential of the metal fluoride reduction) for exothermal carbide formation reactions between carbon and metal fluoride. In these cases, the potential of $U(MC_x/MF_y + xC)$ will be higher than the potential of $U(M/MF_y)$, i.e., carbon would be a stronger oxidizer than the metal fluoride.

(2) The absolute value of this potential difference is proportional to 1/y. Thus, the lower the metal-to-fluoride ratio in the MF_y compound, the higher will be $|\Delta U|$. If one considers a pair of metal fluorides MF_m and MF_n of the same metal M with m < n, this implies that the fluoride-poor metal fluorides can strongly favor metal carbide formation if $\Delta H_{carb.form.} < 0$ eV. In reality, overpotentials might affect the carbide formation process, and it is reasonable to assume that carbide materials with a structure close to graphite (respectively metal-poor carbides) might be favored for kinetic reasons. This can become especially relevant if metals can form various MC_x metal carbides with different values of *x*, and some of them have more complex structures which require a strong degree of reorganization. From this one could in principle expect that the formation of a crystalline carbide induces strong overpotentials, which can then favor the metal fluoride reduction (Figure 4-4a).

(3) Graphite is the thermodynamically most stable modification of carbon. The formation energy of metal carbides from metastable carbon species (e.g., non-graphitic regions within carbon materials) will thus be energetically more favorable and would lead to higher values of ΔU accordingly. We exemplified this by calculating the values of $U(MC_x/MF_y + \frac{x}{60} C_{60})$ and the

corresponding ΔU values additionally. Though the absolute potential differences have to be read with caution, this shows that the formation of crystalline metal carbides would become energetically even more accessible.

(4) Further, non-graphitic carbon can also form non-crystalline surface adducts of metals undergoing reduction. The energy of such metal carbides cannot be easily calculated and would require detailed DFT-based optimization which is beyond the scope of this manuscript. However, one can estimate the potential influence from the analogy of metals (e.g., Na) that do not form a stable carbide. For Na-ion batteries, it is known that although Na cannot be inserted into graphite, it can reduce non-graphitic carbon regions and form surface adducts there. This can happen at potentials just above the potential of Na/Na^+ (adsorption within micropores) up to ~1–2 V for hard carbon materials and can be relevant for the commonly used carbon additives.

(5) Let us additionally consider the case of a metal carbide with an energy above the convex hull, i.e., being metastable under ambient conditions. From a simple energetic viewpoint, the corresponding metal fluorides should be transformed first to the metal in the reduction in the conversion process, followed by the reduction of carbon under the formation of the carbide. Practically, conversion processes are often accompanied by overpotentials, and the crystallization of the metal species to the thermodynamically most stable metallic state might be stronger impeded for kinetic reasons than the metal carbide formation itself (especially considering the non-graphitic regions within carbon materials and the formation of surface adducts). It has been discussed previously that this might be strongly impacted by the melting point of the metal and the fluoride ion conductivity of the corresponding metal fluoride.[20] Thus, if there are considerable overpotentials hindering the metal-to-metal fluoride transformation,

carbide formation could in principle take place if it is itself not affected by similarly strong kinetic inhibition (see Figure 4-4b).

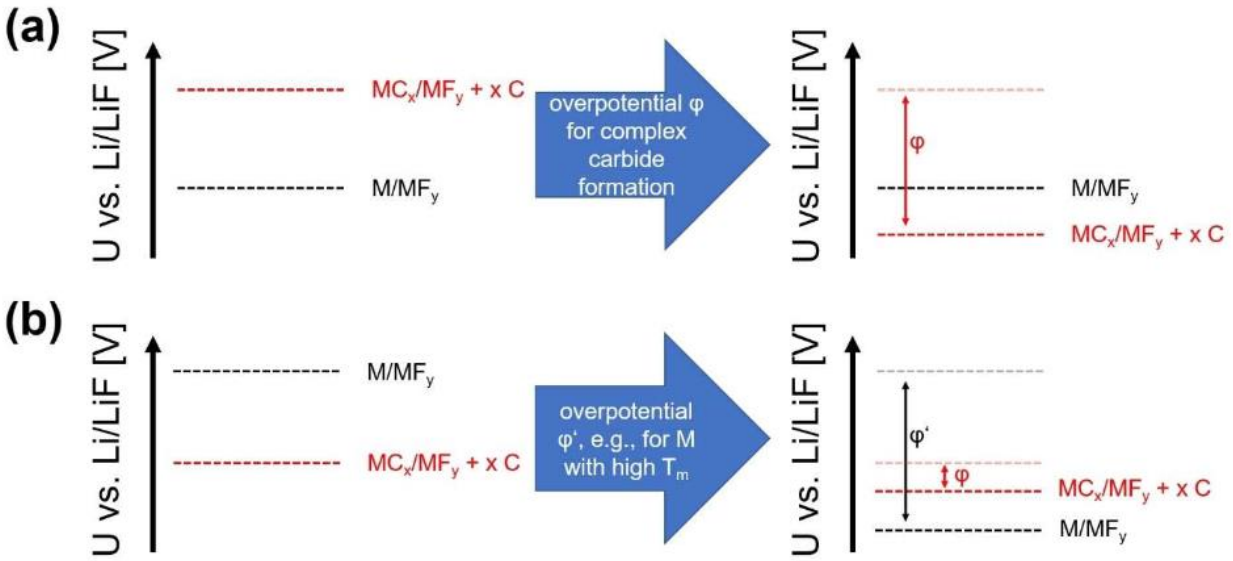


Figure 4-4. Impact of overpotentials in formation energetics. Overpotentials can favor targeted metal formation (a) or undesirable metal carbide formation (b).

The values for $U(M/MF_y)_{vs.\ Li/LiF}$, $U(MC_x/MF_y + xC)_{vs.\ Li/LiF}$, and $\Delta U(MC_x{-}M)$ were calculated for all combinations of MF_y and MC_x available within the Materials Project Database. These values for the different potentials are tabulated in the Appendix and comprise the data for stable and unstable metal carbides with energies on or above the convex hull. According to the considerations mentioned above, one can narrow these data by comparing the most reasonably stable MF_y compounds with the most stable metal carbides MC_x. Additional details are provided in Chapter 2. This summary reveals valuable information about which elements might favor carbide formation prior to the reduction of the respective metal fluoride or when carbon interactions of the metal (not to be confused with carbon fluorination for high voltage cathodes) might become relevant.

These findings are summarized as follows and show in Figure 4-5:

(1) For the late first-row transition metals starting with Cu, as well as the late second/third-row transition metals starting with Ru and Os, respectively, metal formation seems to be the most plausible process for metal fluoride reduction. In addition, these M/MF_y combinations have high potentials, implying that these metals are likely to be used on the cathode side, for which the low potentials required for carbon reduction will be practically not induced. Indeed, for such materials one would rather expect an oxidation of carbon under formation of fluorinated carbon species as has been found for cathode materials. The unfavourability of carbide formation is further extended to the p-block metals of the respective row of the periodic table. Apart from Cu (which does not seem to form a reasonably stable carbide), all these metals form metal-rich carbides with $x \leq 1$. Considering that carbide formation would have to occur at the interface between M and C, this would imply that a fairly large metal cluster would have to form prior to the reaction with C. This consideration is of special importance for ZnF_2, PbF_2, or SnF_2, which have been recently investigated as reference electrodes or as anodes for FIBs. The values of $\Delta U(MC_x-M)$ for these metals are below −0.5 V, which renders the carbide formation energetically unfavorable and could explain why these materials appear to show good reversibility in FIBs. The fairly low melting points of these metals further support the ease of the MF_y to M conversion process.

(2) Alkaline earth metals (apart from Na, Mg, Ca) form stable metal carbides and have potentials that are sufficiently low for them to be considered as anode materials within FIBs. Therefore, the corresponding metal fluorides are likely not to work as conversion materials in the presence of carbon since carbon reduction will be the most favorable process. Furthermore, we note that all these metals form carbon-rich carbides with $x \gg 1$; the corresponding structures are graphite-related, with metal ions inserted between the graphene layers. Considering that

metal insertion into graphite is a process that requires fairly low structural reorganization and thus potentially low thermal activation, we conclude that carbide formation will likely dominate over metal formation for most alkaline and alkaline earth metals. This consideration will become particularly important when using anodes such as SrF_2, BaF_2, or tysonite-/fluorite-type solid fluoride ion conductors.[21–24] However, the impacts of carbide formation might not be entirely negative, and as we will discuss in the conclusions, this might even provide a beneficial new perspective for the development of anode materials for FIBs.

(3) Sc, Ti, V, Zr, Nb, Hf, and Ta also show a strong tendency to form carbides prior to the reduction of the metal fluoride. In contrast to the alkaline and alkaline earth metals, the corresponding carbides MC_x have values of $x \leq 1$, and the structures of the metal carbides are not related to the structure of graphite. This implies that at the interface to the carbon additive, a large amount of M species would have to be built up, accompanied by a reconstructive reorganization of C and M species for carbide formation. Thus, although the formation of MC_x is energetically favored, overpotentials arising from this redistribution might reduce the likelihood of carbide formation. Nevertheless, once metal carbide clusters form, they are likely to show reduced reversibility for reconverting, which is related to the high melting temperatures of these carbide materials. One must also consider that the metals M have high melting temperatures themselves, which could severely impede the conversion process between the metal and the metal fluoride as well. This would likely explain why these metal fluorides have not been reported to be used as anode materials so far, though their potentials and capacities would reasonably justify their experimental investigation.

(4) Cr, Mn, Fe, Co, Ni, Mo, W, and Re have values of $\Delta U \approx 0$. Therefore, carbide formation vs. metal formation will strongly depend on overpotentials for the different reactions. Since all these

metals have high melting potentials and the corresponding metal carbides MC_x have values of $x \ll 1$, both processes become unfavorable, and these metals are unlikely to be reasonably exploited as anode or cathode materials within conversion-type reactions in the authors' opinion.

(5) The different lanthanides LnC_x deserve special attention since many of their corresponding metal fluorides have been considered as solid electrolytes for FIBs. Remarkably, all lanthanides appear to energetically favor carbide formation over metal formation within a FIB. However, the values of x considerably fluctuate for the different lanthanides, with $x \leq 1$ or $x \gg 1$. Only Eu and Yb seem to favor the formation of graphite intercalation compounds $x \gg 1$ from an energetic viewpoint. However, because carbide formation appears to be generally favorable for lanthanides, one can imagine that these metals would have a strong tendency to form M–C adducts to non-graphite-like regions of carbon additives, which would be energetically susceptible to the formation of lanthanide carbides. Therefore, we assume that the carbide reaction might indeed prove to be a limiting factor for the use of LnF_y-based electrolytes[24–31] at the anode sides and that their usability with low-potential anodes must be conceptually reconsidered.

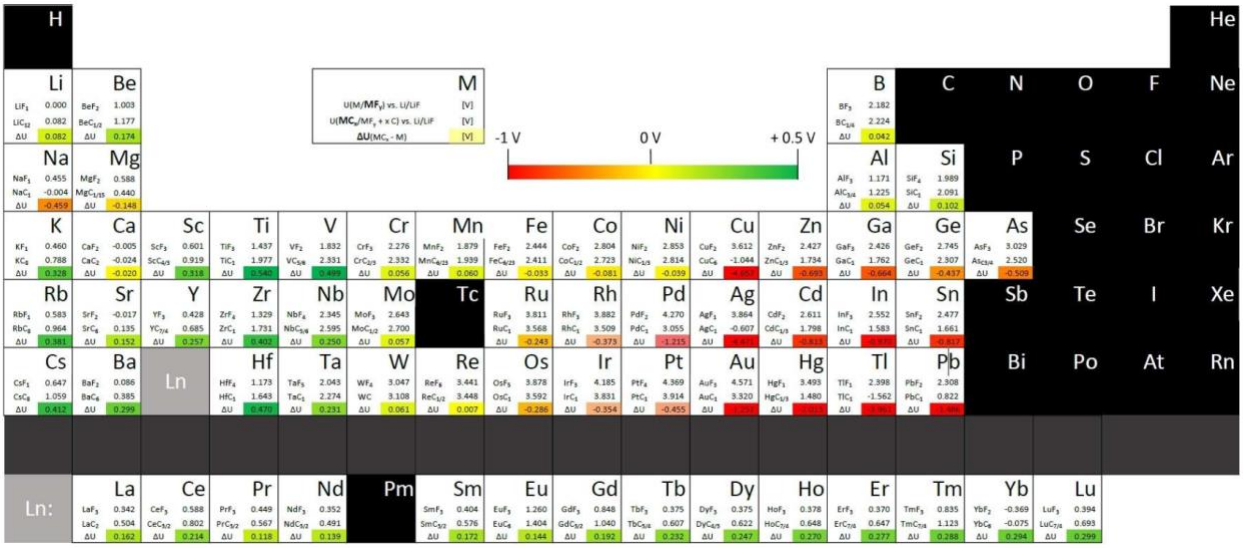


Figure 4-5. Summary of competing formation energetics. Comparison of $U(M/MF_y)_{vs.\ Li/LiF}$, $U(MC_x/MF_y + xC)_{vs.\ Li/LiF}$, and $\Delta U(MC_x\text{-}M)$ for the different combinations of stable MF_y with a low value of y and the thermodynamically most stable carbide MC_x. Actinides were not considered for the calculations since they do not show practical relevance. Furthermore, certain elements (Tc, Pm, Pb, Sb, Bi, Te, Po) did not contain any entries for their corresponding metal carbides. Furthermore, some elements form molecular carbides (H, N, O, S, Cl, Br, I) or do not form carbides at all (noble gases) and were thus not included.

4.3 Conclusions

In this chapter, I have shown that carbide formation has the potential to be a significant side reaction for metal fluoride MF_y conversion-based electrodes within FIBs. This is most severe in combination with electropositive metals such as alkali, alkaline earth, lanthanides and early 3d/4d/5d transition metals but is an unlikely process with anodes such as Sn, Pb, Zn. Although carbide formation would be favored for all these metals, we emphasize that kinetic barriers might facilitate this process most strongly for carbon-rich carbides MC_x with $x \gg 1$, whose structures can be derived from the layered graphite arrangement. However, the complexity of carbon additives, which can also contain non-graphitic regions with higher energies, might render carbon reduction with metal adducts a possible scenario for metals that can form stable carbides and other metals as well. This reaction should be considered as a

potential side reaction within anode materials for FIBs in the future and has not been considered in previous research so far.

Furthermore, we think that carbide formation, especially in the context of metal insertion into graphite, could be exploited for designing anode materials for FIBs. This metal fluoride conversion in combination with metal insertion into graphite host lattices provides the opportunity for improving the cycling stability of conversion anodes, which is currently considered a key limitation for the development of functional FIBs. This result is reminiscent of previous work on cathode development for lithium-ion batteries, for example, by Reddy et al.[32] who used iron metal fluorides at the cathode side (from reacting Fe with carbon fluoride via ball milling) for fluoride storage in the conversion of LiF according to $LiF + Fe \rightarrow FeF_2 + 2\ Li^+ + 2\ e^-$.

Thus, the successful implementation of metals into carbon networks might provide the opportunity to create novel nanostructured anodes with improved reversibility. Although this would imply a reduction in the gravimetric capacity and a reduction of operation potential, this process could be a cheap alternative in combination with light alkaline earth metals, such as Ca^{2+} or Mg^{2+} (e.g., $C_{grav,theo}$ = 860 mAh/g for Mg/MgF_2 vs. $C_{grav,theo}$ = 399 mAh/g for the hypothetical pair $MgC_6/MgF_2 + C_6$). Although the intercalation of carbon is not known for the naked metal cations, it can be supported by the addition of complexation agents and intercalation of the complex instead of the naked metal ion for M = Ca, Mg, Na.

We also think that potassium fluoride KF might deserve special attention for designing electrodes with high reversibility, especially within all solid-state FIBs. The potential for potassium insertion into carbon is at a potential similar to graphite materials used for lithium-ion batteries. For $KF + 8\ C + e^- \rightarrow KC_8 + F^-$, the capacity would be at a reasonable value of $C_{grav,theo}$ = 174 mAh/g. More remarkably, considering the molar volumes of the different reaction partners, the volume change would be as low as ± 2.5% for changing between the charged and

discharged state. Additionally, potassium and carbon have a high abundance and would not represent a limiting factor for battery manufacturing.

REFERENCES

(1) Spahr, M. E.; Goers, D.; Leone, A.; Stallone, S.; Grivei, E. Development of Carbon Conductive Additives for Advanced Lithium Ion Batteries. *J. Power Sources* **2011**, *196* (7), 3404–3413. https://doi.org/10.1016/j.jpowsour.2010.07.002.

(2) Jin, B.; Gu, H. B.; Zhang, W.; Park, K. H.; Sun, G. Effect of Different Carbon Conductive Additives on Electrochemical Properties of LiFePO 4-C/Li Batteries. *Journal of Solid State Electrochemistry* **2008**, *12* (12), 1549–1554. https://doi.org/10.1007/s10008-008-0509-3.

(3) Zhang, L.; Reddy, M. A.; Fichtner, M. Electrochemical Performance of All Solid-State Fluoride-Ion Batteries Based on Thin-Film Electrolyte Using Alternative Conductive Additives and Anodes. *Journal of Solid State Electrochemistry* **2018**, *22* (4), 997–1006. https://doi.org/10.1007/s10008-017-3838-2.

(4) Nowroozi, M. A.; Wissel, K.; Donzelli, M.; Hosseinpourkahvaz, N.; Plana-Ruiz, S.; Kolb, U.; Schoch, R.; Bauer, M.; Malik, A. M.; Rohrer, J.; Ivlev, S.; Kraus, F.; Clemens, O. High Cycle Life All-Solid-State Fluoride Ion Battery with La2NiO4+d High Voltage Cathode. *Commun. Mater.* **2020**, *1* (1), 1–16. https://doi.org/10.1038/s43246-020-0030-5.

(5) Wissel, K.; Schoch, R.; Vogel, T.; Donzelli, M.; Matveeva, G.; Kolb, U.; Bauer, M.; Slater, P. R.; Clemens, O. Electrochemical Reduction and Oxidation of Ruddlesden − Popper- Type La 2 NiO 3 F 2 within Fluoride-Ion Batteries. **2021**. https://doi.org/10.1021/acs.chemmater.0c01762.

(6) Wissel, K.; Heldt, J.; Groszewicz, P. B.; Dasgupta, S.; Breitzke, H.; Donzelli, M.; Waidha, A. I.; Fortes, A. D.; Rohrer, J.; Slater, P. R.; Buntkowsky, G.; Clemens, O. Topochemical Fluorination of La2NiO4+d: Unprecedented Ordering of Oxide and Fluoride Ions in La2NiO3F2. *Inorg. Chem.* **2018**, *57* (11), 6549–6560. https://doi.org/10.1021/acs.inorgchem.8b00661.

(7) Wissel, K.; Malik, A. M.; Vasala, S.; Plana-Ruiz, S.; Kolb, U.; Slater, P. R.; Da Silva, I.; Alff, L.; Rohrer, J.; Clemens, O. Topochemical Reduction of La2NiO3F2: The First Ni-Based Ruddlesden-Popper n = 1 T′-Type Structure and the Impact of Reduction on Magnetic Ordering. *Chemistry of Materials* **2020**, *32* (7), 3160–3179. https://doi.org/10.1021/acs.chemmater.0c00193.

(8) Jain, A.; Ong, S. P.; Hautier, G.; Chen, W.; Richards, W. D.; Dacek, S.; Cholia, S.; Gunter, D.; Skinner, D.; Ceder, G.; Persson, K. A. Commentary: The Materials Project: A Materials Genome Approach to Accelerating Materials Innovation. *APL Mater.* **2013**, *1* (1). https://doi.org/10.1063/1.4812323.

(9) Inagaki, M.; Kang, F. *Materials Science and Engineering of Carbon: Fundamentals*; 2014.

(10) Wertheim, G.; Van Attekum, Pmt.; Basu, S. *ELECTRONIC STRUCTURE OF LITHIUM GRAPHITE*; Pergamon Press Ltd, 1980; Vol. 33.

(11) Dolotko, O.; Senyshyn, A.; Mühlbauer, M. J.; Nikolowski, K.; Ehrenberg, H. Understanding Structural Changes in NMC Li-Ion Cells by in Situ Neutron Diffraction. *J. Power Sources* **2014**, *255*, 197–203. https://doi.org/10.1016/j.jpowsour.2014.01.010.

(12) Guerard, D.; Lagrange, P.; Makr~ni, M. El; Hi, A.; Rold, ? *ETUDE STRUCTURALE DU GRAPHITURE I DE CESIUMt*; 1978; Vol. 16.

(13) Makrini, M. El; Gubrard, D.; Lagrange, P.; Harold, A. *INSERTION DE LANTHANOIDES DANS LE GRAPHITE*; 1980; Vol. 18.

(14) ROBERT E. GEBELT; HARRY A. EICK. *The Preparation and Some Properties of a Europium Dicarbide Phase*; 1963. https://pubs.acs.org/sharingguidelines.

(15) Giorgi, A. L.; Szklarz, E. G.; Krikorian, N. H.; Krupka, M. C. *Preparation and Superconductivity of the Sesquicarbide Phase in the Lanthanum-Thorium-Carbon System*; 1970.

(16) Wood, I. G.; Vočadlo, L.; Knight, K. S.; Dobson, D. P.; Marshall, W. G.; Price, G. D.; Brodholt, J. Thermal Expansion and Crystal Structure of Cementite, Fe3C, between 4 and 600 K Determined by Time-of-Flight Neutron Powder Diffraction. *J. Appl. Crystallogr.* **2004**, *37* (1), 82–90. https://doi.org/10.1107/S0021889803024695.

(17) Bernstein, J.; Armon, E.; Zemel, E.; Kolodney, E. Formation of Indium Carbide Cluster Ions: Experimental and Computational Study. *Journal of Physical Chemistry A* **2013**, *117* (46), 11856–11865. https://doi.org/10.1021/jp403031p.

(18) Reddic, J. E.; Duncan, M. A. *Composite Samples and the Generation of Novel Metal Carbide Clusters*; ELSEVIER, 1997; Vol. 264.

(19) Ticknor, B. W.; Bandyopadhyay, B.; Duncan, M. A. Photodissociation of Noble Metal-Doped Carbon Clusters. *Journal of Physical Chemistry A* **2008**, *112* (48), 12355–12366. https://doi.org/10.1021/jp807867r.

(20) Nowroozi, M. A.; Clemens, O. Insights on the Behavior of Conversion-Based Anode Materials for Fluoride Ion Batteries by Testing against an Intercalation-Based Reference Cathode. *ACS Appl. Energy Mater.* **2018**, *1* (11), 6626–6637. https://doi.org/10.1021/acsaem.8b01630.

(21) Mohammad, I.; Chable, J.; Witter, R.; Fichtner, M.; Reddy, M. A. Synthesis of Fast Fluoride-Ion-Conductive Fluorite-Type Ba1-XSbxF2+x (0.1 ≤ x ≤0.4): A Potential Solid Electrolyte for Fluoride-Ion Batteries. *ACS Appl. Mater. Interfaces* **2018**, *10* (20), 17249–17256. https://doi.org/10.1021/acsami.8b04108.

(22) Clemens, O.; Rongeat, C.; Reddy, M. A.; Giehr, A.; Fichtner, M.; Hahn, H. Electrochemical Fluorination of Perovskite Type BaFeO2.5. *Dalton Transactions* **2014**, *43* (42), 15771–15778. https://doi.org/10.1039/c4dt02485k.

(23) Rongeat, C.; Anji Reddy, M.; Diemant, T.; Behm, R. J.; Fichtner, M. Development of New Anode Composite Materials for Fluoride Ion Batteries. *J. Mater. Chem. A Mater.* **2014**, *2* (48), 20861–20872. https://doi.org/10.1039/c4ta02840f.

(24) Rongeat, C.; Anji Reddy, M.; Witter, R.; Fichtner, M. Solid Electrolytes for Fluoride Ion Batteries: Ionic Conductivity in Polycrystalline Tysonite-Type Fluorides. *ACS Appl. Mater. Interfaces* **2014**, *6* (3), 2103–2110. https://doi.org/10.1021/am4052188.

(25) Rongeat, C.; Reddy, M. A.; Witter, R.; Fichtner, M. Nanostructured Fluorite-Type Fluorides as Electrolytes for Fluoride Ion Batteries. *Journal of Physical Chemistry C* **2013**, *117* (10), 4943–4950. https://doi.org/10.1021/jp3117825.

(26) Düvel, A.; Bednarcik, J.; Šepelák, V.; Heitjans, P. Mechanosynthesis of the Fast Fluoride Ion Conductor Ba1-XLa XF2+ x: From the Fluorite to the Tysonite Structure. *Journal of Physical Chemistry C* **2014**, *118* (13), 7117–7129. https://doi.org/10.1021/jp410018t.

(27) Chable, J.; Dieudonné, B.; Body, M.; Legein, C.; Crosnier-Lopez, M. P.; Galven, C.; Mauvy, F.; Durand, E.; Fourcade, S.; Sheptyakov, D.; Leblanc, M.; Maisonneuve, V.; Demourgues, A. Fluoride Solid Electrolytes: Investigation of the Tysonite-Type Solid Solutions La1-XBaxF3-x (x < 0.15). *Dalton Transactions* **2015**, *44* (45), 19625–19635. https://doi.org/10.1039/c5dt02321a.

(28) Dieudonné, B.; Chable, J.; Mauvy, F.; Fourcade, S.; Durand, E.; Lebraud, E.; Leblanc, M.; Legein, C.; Body, M.; Maisonneuve, V.; Demourgues, A. Exploring the Sm1-XCaxF3-x Tysonite Solid Solution as a Solid-State Electrolyte: Relationships between Structural Features and F- Ionic Conductivity. *Journal of Physical Chemistry C* **2015**, *119* (45), 25170–25179. https://doi.org/10.1021/acs.jpcc.5b05016.

(29) Bhatia, H.; Thieu, D. T.; Pohl, A. H.; Chakravadhanula, V. S. K.; Fawey, M. H.; Kübel, C.; Fichtner, M. Conductivity Optimization of Tysonite-Type La1-XBaxF3-x Solid Electrolytes for Advanced Fluoride Ion Battery. *ACS Appl. Mater. Interfaces* **2017**, *9* (28), 23707–23715. https://doi.org/10.1021/acsami.7b04936.

(30) Chable, J.; Martin, A. G.; Bourdin, A.; Body, M.; Legein, C.; Jouanneaux, A.; Crosnier-Lopez, M. P.; Galven, C.; Dieudonné, B.; Leblanc, M.; Demourgues, A.; Maisonneuve, V. Fluoride Solid Electrolytes: From Microcrystalline to Nanostructured Tysonite-Type La0.95Ba0.05F2.95. *J. Alloys Compd.* **2017**, *692*, 980–988. https://doi.org/10.1016/j.jallcom.2016.09.135.

(31) Dieudonné, B.; Chable, J.; Body, M.; Legein, C.; Durand, E.; Mauvy, F.; Fourcade, S.; Leblanc, M.; Maisonneuve, V.; Demourgues, A. The Key Role of the Composition and Structural Features in Fluoride Ion Conductivity in Tysonite Ce1−xSrxF3−x Solid Solutions. *Dalton Transactions* **2017**, *46* (11), 3761–3769. https://doi.org/10.1039/c6dt04714a.

(32) Reddy, M. A.; Breitung, B.; Chakravadhanula, V. S. K.; Wall, C.; Engel, M.; Kübel, C.; Powell, A. K.; Hahn, H.; Fichtner, M. CFx Derived Carbon-FeF2nanocomposites for Reversible Lithium Storage. *Adv. Energy Mater.* **2013**, *3* (3), 308–313. https://doi.org/10.1002/aenm.201200788.

(33) Zhang, L.; Reddy, M. A.; Fichtner, M. Electrochemical Performance of All Solid-State Fluoride-Ion Batteries Based on Thin-Film Electrolyte Using Alternative Conductive Additives and Anodes. *Journal of Solid State Electrochemistry* **2018**, *22* (4), 997–1006. https://doi.org/10.1007/s10008-017-3838-2.

CHAPTER 5: DISORDERED ELECTRON NETWORK IN Ti_2C

5.1 Introduction

In Chapter 1 I establish that electrides are compelling candidates for FIB anodes through the EAX mechanism, in which a fluoride ion replaces a bare electride electron while the host framework is largely preserved.[1–6] The electride materials previously investigated for this application, Y_2C and Sc_2C, are ordered rocksalt carbide compounds whose anionic electrons are characterized by 2D layered planes.[7–10] However, electride character is not present in every ordered rocksalt carbide and a central finding from the broader electride literature is that electron topology can be tuned by composition, structure, and local environment.[11–16]

This tunability is well established for fully crystalline electride systems, particularly in descriptions of dimensionality where electride sites may occupy isolated cages (0D), channels (1D), planes (2D), or fully connected networks (3D).[2,17] However, the effect of substantial structural disorder on electride character remains poorly understood. Prior studies of disordered electride-like states have focused on 0D systems, where electrons are confined to isolated sites. The clearest precedent for bare electrons persisting despite lattice disruption is the F-center in alkali halides and metal oxides, in which a single electron is trapped at an isolated anion vacancy with no connectivity between neighboring vacancy sites.[18] Similarly, Yang et al. and Chae et al. found that vacancies in CeO and Ca_2N can also produce bare electrons, but these effects remain localized.[19,20] A more developed example comes from mayenite, where Kim, Shimoyama, and Hosono showed that the characteristic 0D electride cage motif survives melt-quenching into an amorphous host,[21] and complementary computational studies linked disordered glass topology in $CaO–Al_2O_3$ to the persistence of localized electron-hosting cavities.[22,23] Ahmed et al. also demonstrated that amorphous electride-like behavior can emerge in Si and in alkali or alkaline earth elements, but these features arise from compression and melting rather than from a disordered vacancy network in the solid state.[24]

Collectively, these precedents confirm that localized, 0D electride-like character can survive disorder, but no studies have investigated whether a connected 3D electron network can do the same. This chapter investigates that open question in Ti_2C, which provides an experimentally accessible order/disorder continuum in an earth-abundant host with a predicted 3D electride ground state.

Titanium carbide adopts a disordered rocksalt (DRX) structure across a wide range of carbon stoichiometries.[25,26] In these structures, C atoms and vacancies are randomly distributed over the anion sublattice against a fully occupied Ti cation framework. At the Ti_2C composition (50% anion site vacancy), the thermodynamically predicted ground state is the ordered Fd-3m phase, in which the Ti-C lattice and C vacancies are arranged in a bicontinuous 3D network. Under the dimensionality framework introduced by Weaver et al.,[17] this ordered Fd-3m phase qualifies as a 3D electride, with bare electrons occupying the interconnected vacancy sites (Figure 5-1).

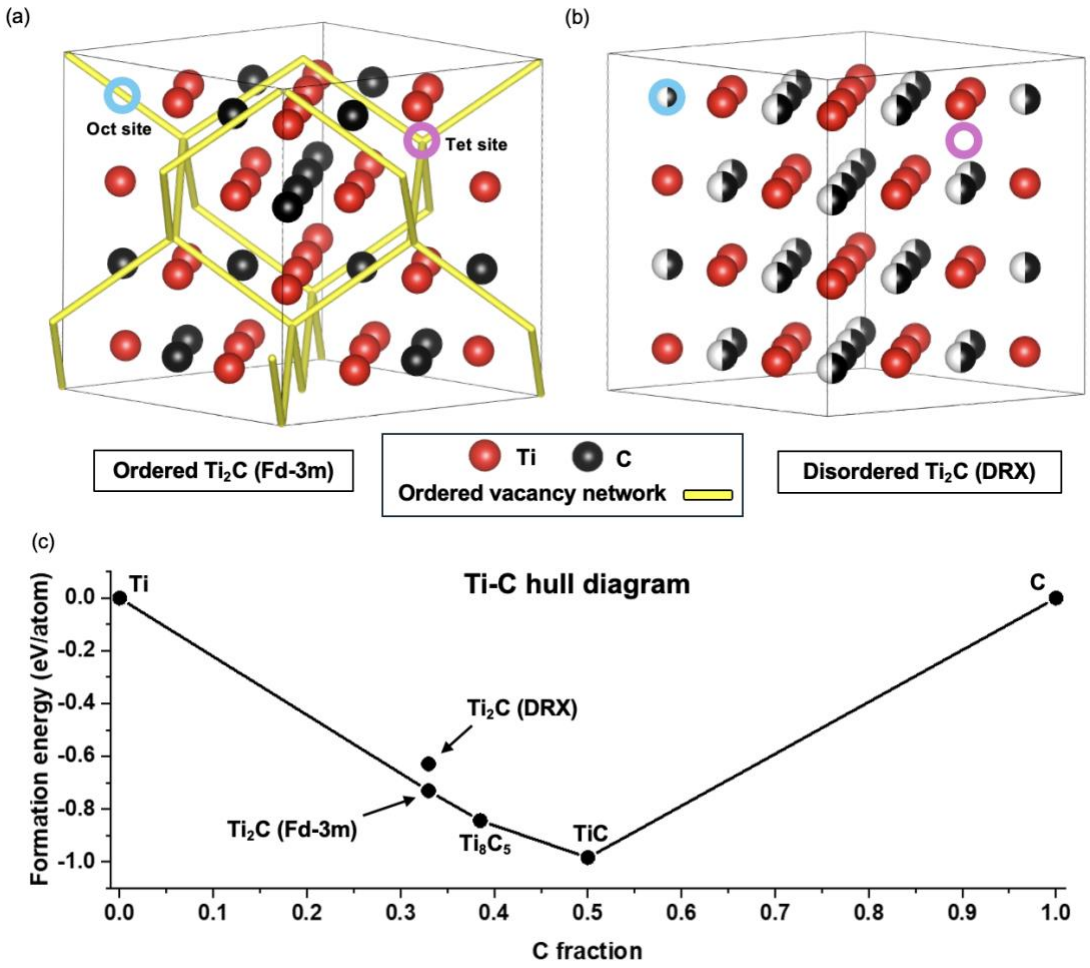


Figure 5-1. Rocksalt Ti-C system. (a) Crystal structure of ordered Fd-3m Ti_2C, with ordered vacancy/electride network shown in yellow. (b) Crystal structure of disordered (DRX) Ti_2C, showing random 50% occupation at C sites. (c) Ti-C hull diagram calculated via DFT, showing that the Fd-3m phase is thermodynamically more stable than the DRX phase.

The experimental reality of Ti_2C, however, is more complex than this thermodynamic prediction suggests. Although some studies report synthesis of ordered Ti_2C, the degree of carbon sublattice ordering achieved in practice remains debated, owing primarily to the difficulty of distinguishing partially ordered from fully ordered phases using diffraction-based methods. Early work in 1967 by Goretzki was the first to report evidence consistent with Fd-3m Ti_2C based on superstructure reflections observed by neutron diffraction.[27] Similar evidence was later reported in 1971 by Bell and Lewis using electron diffraction,[28] and by Em and Tashmetov using X-ray diffraction,[29] where “weak superlattice reflections” were identified. These studies provide

important precedent for ordered Ti_2C, but they were conducted before the widespread use of more advanced quantitative phase-analysis methods, making it difficult to determine whether the reported reflections correspond to fully ordered material rather than partial ordering. This ambiguity persists in more recent work. For example, in 2013 Nguyen et al.[30] reported diffraction features consistent with Fd-3m ordering but noted that it was difficult to establish certainty in phase-pure synthesis because the DRX and Fd-3m phase XRD patterns are nearly indistinguishable.

The crystallographic signature of the Fd-3m superstructure is a weak reflection at 17.7° 2θ, which is dramatically less intense than the strong reflections shared with the parent DRX structure at 36° and 42°. This intensity disparity makes even modern quantitative phase identification against a DRX background highly sensitive to calibration and refinement quality. In Chapter 2, I described my approach to advanced Rietveld refinement analysis to more accurately estimate the degree of order in experimental Ti_2C samples. Considering these characterization challenges, I suggest prior literature claims of phase-pure Fd-3m synthesis are more accurately interpreted as evidence of partial ordering rather than complete conversion. The Ti_2C system therefore presents not a clean binary between "ordered" and "disordered" states, but an experimentally relevant continuum of carbon sublattice configurations.

This continuum makes Ti_2C an ideal test case for the central question motivating this chapter. If the 3D electride state predicted for ordered Fd-3m Ti_2C is a strict consequence of long-range crystallographic periodicity, then departure from ideal vacancy ordering should progressively degrade the connected electron network, reducing it to the kinds of isolated features observed in F-centers, glassy mayenite, and other low-dimensional bare electron features discussed above. Alternatively, if the bare electron character is governed primarily by local charge transfer dynamics, then the 3D network may prove robust to substantial sublattice disorder. The 50% vacancy concentration at the Ti_2C stoichiometry is central to why this system

can distinguish between these possibilities. This concentration is far above the ~20% vacancy site percolation threshold for the FCC sublattice,[31] meaning that vacancy connectivity is topologically guaranteed regardless of how carbon atoms are arranged. The question is therefore not whether the vacancy network remains connected under disorder, but whether the electronic character at each vacancy site is similarly preserved.

In this chapter I address this question through two methods. First, I examine why phase-pure Fd-3m Ti_2C is experimentally inaccessible, using cluster expansion and Monte Carlo simulations to show that a fundamental kinetic mismatch between carbon ordering thermodynamics and carbon diffusivity creates an intrinsic ceiling on the degree of order achievable under realistic thermal processing conditions. Second, I apply electron localization function (ELF) analysis with BadELF charge partitioning across a series of Ti_2C configurations spanning the full order/disorder regime, quantifying how the electronic character of both primary octahedral bare electron sites and secondary tetrahedral interstitial nodes responds to progressive loss of long-range order. Together, these analyses test whether the 3D electride character predicted for ordered Ti_2C is a fragile consequence of crystallographic periodicity or a robust feature of local coordination chemistry. Resolving this issue has broader importance for electride design, as it helps determine whether connected electron networks require highly ordered crystal structures or whether they may also be realized in structurally disordered, earth-abundant materials relevant to FIB electrodes.

5.2 Results and Discussion

5.2.1 Synthesis of Partially Ordered Ti_2C

I began by pursuing phase-pure Fd-3m Ti_2C using a synthesis route based on arc melting Ti ingots and C pellets, followed by annealing in sealed quartz ampules under vacuum. In this procedure, the arc-melted samples were annealed at high temperature and then cooled under controlled conditions to promote carbon ordering within the rocksalt framework. I

systematically varied the maximum hold temperature from 800 to 1200 °C, the hold time at maximum temperature from 2 to 12 days, and the cooling rate from 10 to 100 °C/hr to determine which conditions most effectively increased the ordered fraction. These experiments showed that annealing at 1000 °C for 4 days followed by 20 °C/hr cooling gave the highest degree of detectable C ordering while avoiding unnecessary furnace wear or excessively long heating profiles. Under these conditions, advanced Rietveld refinement (described in Methods) indicated that the arc-melting-based route plateaued at around 45% Fd-3m character. I hypothesized that this ceiling might be due to insufficient Ti/C homogenization due to arc melting. Therefore, I turned to a procedure of annealing ground Ti/C powder mixtures without arc melting with the same heating/cooling profiles. Combining this with one round of regrinding and reannealing to further improve reactant contact and increase Ti/C interfacial area produced the highest degree of partial ordering achieved in this study, but still only to roughly 50% Fd-3m character.

While these methods produced the highest degree of partial ordering, I explored additional variables to determine whether further optimization could improve the ordered fraction. The arc melting process results in material ablation on the order of 15–30% of the total pellet mass, so I tested various ratios of excess Ti and C precursors to maintain the target stoichiometry, and varied total pellet mass from 100–500 mg to minimize ablative effects. To ensure arc melting was producing a homogeneous solid solution, I also modified the number of arcing events (4–8) and individual arcing duration (3–15 seconds). I hypothesized that oxygen incorporation might be inhibiting carbon ordering, and attempted to reduce oxygen content by using higher-purity Ti precursors and arc-melting sacrificial Ti ingots immediately before the Ti_2C sample to scavenge residual oxygen from the reaction chamber. Finally, in the powder-based procedure, I also tried multiple rounds of regrinding and reannealing. These variations did not produce increases in the ordered fraction, and additional experimental details are provided in the Methods chapter. Taken together, these results suggested that the formation of Fd-3m

Ti_2C was limited not by synthetic optimization, but by kinetic barriers that hinder complete conversion to the predicted thermodynamic phase.

5.2.2 Temperature-Dependent Model of C Ordering

To understand this synthetic ceiling, we constructed a cluster expansion (CE) model using the CLEASE package interfaced with Monte Carlo (MC) simulations.[32] The model was trained on approximately 250 Ti_2C configurations containing 32–64 atoms, generated with randomly initialized carbon/vacancy arrangements on the anion sublattice against a fully occupied, static Ti framework. Total energies for these configurations were calculated using VASP with the r^2SCAN meta-GGA functional. The fitted CE model was validated by leave-one-out cross-validation, yielding an error of 5.7 meV/atom, which is small relative to the overall configuration energy range and consistent with reported CLEASE performance. MC simulations were then performed at 17 temperatures spanning 1 to 1500 K on a 1,728-atom supercell, using 3 million steps per temperature with single-atom carbon moves at each step to generate equilibrium carbon configurations across the full temperature range.

To quantify carbon sublattice ordering across the temperature-resolved Monte Carlo supercells, I developed a structural analysis workflow based on local Ti-centered vacancy environments. Each Ti atom in rocksalt Ti_2C occupies an octahedral cage of six carbon/vacancy positions, and the local environment can be encoded as a six-bit motif representing carbon presence or absence at each site. In ordered Fd-3m Ti_2C, all Ti atoms adopt one of eight octahedral face-capping motifs with three carbons and three vacancies. A Ti atom matching one of these motifs is defined as a "first neighbor ordered Ti center" (1NOTC). The 1NOTC is a simple metric of local ordering, but it overpredicts Fd-3m character at high temperatures. At 1300 K the 1NOTC fraction is approximately 25%, yet experimental quenching from this temperature produces no detectable ordering by XRD. A stricter metric, the "second neighbor ordered Ti center" (2NOTC), was therefore introduced which necessitates that the central Ti's

twelve Ti neighbors meet criteria reflected in the Fd-3m structure (described fully in Chapter 2). The 2NOTC metric identifies zero ordered centers at 1300 K, bringing the structural analysis into agreement with experiment. Therefore, the 2NOTC fraction was used to gauge the degree of carbon ordering across the range of temperatures investigated.

The 2NOTC temperature profile (Figure 5-1) reveals that carbon ordering occurs in three regimes: (i) 1500–800 K, where fewer than 10% of Ti centers are 2NOTCs; (ii) 800–600 K, where over 70% of the ordering occurs; and (iii) 600–400 K, where the final ~20% of ordering completes, converging to Fd-3m symmetry at 400 K and lower as confirmed by independent space group analysis. These results indicate that entropy drives disordering above roughly 800 K, while the enthalpic preference for Fd-3m-like ordering is strongest during cooling through the 800–600 K window. Critically, carbon mobility is expected to become severely limited in this same temperature window. Using the Arrhenius diffusion equation, ($D = D_0\, e^{-Q/RT}$) together with reported diffusion parameters[33] for carbon in Ti–C ($D_0 = 4.8 \times 10^{-3}$ m²/s, Q = 330 ± 20 kJ/mol) we estimate a carbon diffusivity ~10^{-24} m²/s at 800 K, decreasing to ~10^{-32} m²/s at 600 K. For comparison, Li^+ diffusion in $LiCoO_2$, a functional battery material, is on the order of 10^{-15} m²/s.[34] This means that C mobility decreases by roughly eight orders of magnitude across the temperature range where most ordering must occur. A simple timescale estimate illustrates the implication: the maximum experimental ordering achieved here, approximately 50% Fd-3m, corresponds to the simulated ordering state near 675 K, where D ≈ 10^{-27} m²/s, reached over a 4-day cooling profile. Reaching 80% ordering would require further progression into the 600 K regime, where a composite diffusion rate of about 10^{-31} m²/s implies an estimated timescale of ~4×10^4 days, or about 110 years. Because this extrapolation extends below the temperature range of the original diffusion measurements, it should be interpreted only as an order-of-magnitude estimate. Even so, the result strongly suggests that carbon mobility becomes

negligible in the critical ordering window, making phase-pure Fd-3m Ti_2C effectively inaccessible under realistic thermal processing conditions.

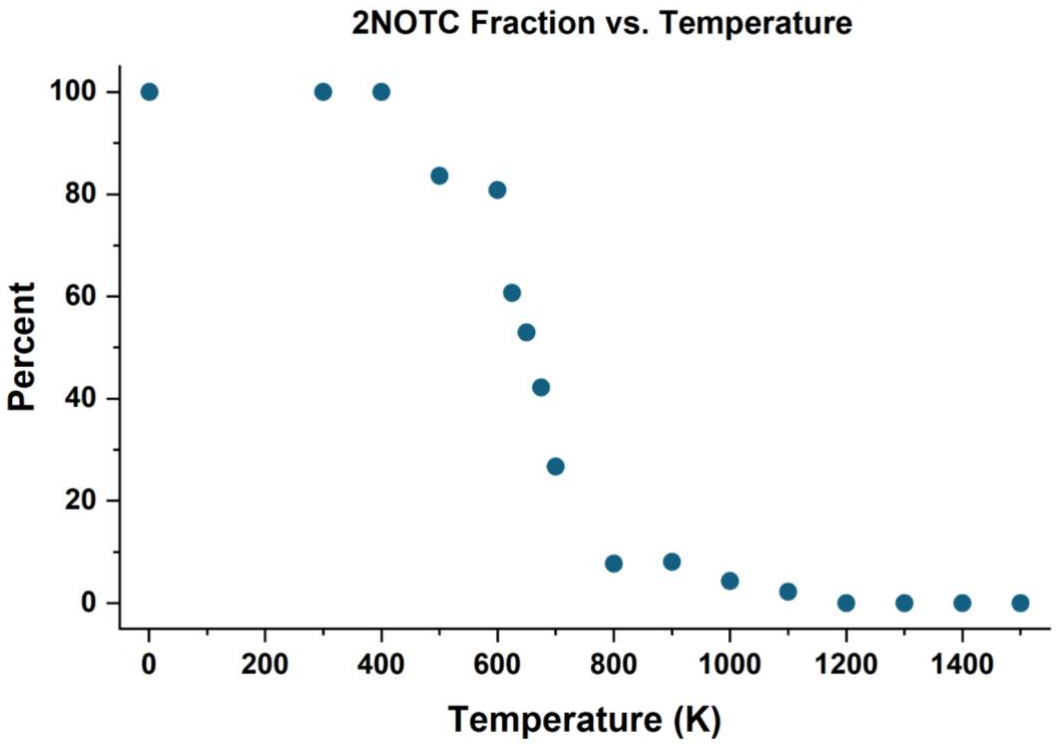


Figure 5-2. 2NOTC fraction vs. Temperature. Less than 10% carbon ordering occurs during cooling from 1500K to 800K, with over 70% of ordering occurring between 800K and 600K. At 100% 2NOTC fraction, the structure is identified as Fd-3m via independent space group analysis.

5.2.3 Vacancy Network Connectivity

To begin answering whether 3D electride networks can persist in partially ordered Ti_2C systems, we investigate whether the vacancy sublattice remains connected in three dimensions with significant carbon disordering. For an FCC rocksalt lattice, each C/vacancy site has 12 nearest C/vacancy neighbors. According to percolation theory, the site percolation threshold for this configuration is 19.8% vacancy occupation, corresponding to ~$TiC_{0.8}$.[31] Because Ti_2C contains 50% carbon vacancies, the vacancy sublattice is far above this percolation threshold, independent of ordering. To confirm this predicted threshold, we quantify connectivity on randomly initialized Ti-C cells with variable vacancy concentration from TiC0.9 to TiC0.5 on

1,600–1,900 atom cells. This analysis demonstrated a marked increase in the size of the largest connected vacancy group at around 20% vacancy concentration, consistent with the threshold predicted by percolation theory. We also find that all vacancies belong to a single connected cluster at and above 40% vacancy concentration, meaning that every vacancy in DRX Ti_2C is reachable from every other vacancy by nearest-neighbor site hopping. Because this connectivity is independent of carbon ordering, the interstitial vacancy network remains fully connected across all possible vacancy configurations. A 3D electron network is therefore never topologically limited by the vacancy landscape itself. However, persistent connectivity alone does not guarantee that bare electron character survives. Disordering may still alter the electronic structure in ways that disrupt electron localization, and investigating those electronic effects motivates the work in the following section.

5.2.4 Electride Topology within Order/Disorder Regime

Having established that phase-pure Fd-3m is kinetically inaccessible but vacancy connectivity persists, we now address the central question of this work: can the three-dimensional electride network predicted for ordered Fd-3m Ti_2C survive when long-range carbon ordering is absent? We address this question by computing the electron localization function (ELF)[35,36] and applying BadELF charge partitioning[37] to a series of ten Ti_2C configurations spanning the full order/disorder regime. Six of these configurations are partially ordered 96-atom structures generated by CE/MC simulations at varying temperatures. Because small-cell MC runs exhibit substantial stochastic noise and independent runs at the same temperature do not reproducibly converge to identical structural motifs, these six structures are used as representative snapshots across the order/disorder continuum, ranked by their 2NOTC fraction, rather than as strictly temperature-indexed configurations. Four additional reference structures complete the series: ideal Fd-3m, Fd-3m with one carbon displaced from its ideal position, Fd-3m with two carbons displaced, and a fully randomized DRX structure.

ELF calculations were performed using VASP with the same parameters described earlier. BadELF analysis was carried out using ElfLabeler parameters chosen to maximize sensitivity to diffuse interstitial electride density while minimizing false assignment of atomic features (min_electride_elf_value = 0.1, min_electride_depth = 0.01, min_electride_charge = 0.01, min_electride_volume = 0.01, min_electride_dist_beyond_atom = 0.01). The covalency filter was additionally disabled (min_covalent_charge = 100, min_covalent_angle = 181°), as it was found to attribute some electride basins to atomic or covalent features under default settings. These parameter choices ensure detection of all interstitial electron features, including low-magnitude tetrahedral nodes that would be missed with default BadELF parameters. Local coordination environments for atoms, octahedral electride basins, and tetrahedral interstitial nodes were assigned using custom Python scripts.

BadELF analysis across all configurations reveals that the total integrated electride charge per formula unit is –1.94 ± 0.03 (1.5% coefficient of variation (CV)). This conservation of total electride charge is supported by stability in all principal atomic and bare electron charge reservoirs (Figure 5-3). Ti oxidation states remain tightly clustered at +2.50 ± 0.02 (CV < 1%), and C oxidation states at –3.07 ± 0.07 (CV = 2.1%), across the full disorder range. The primary octahedral electride site charge averages –1.57 ± 0.08 (CV = 4.9%), displaying modestly greater variation than the atomic constituents but remaining well-conserved as host lattice symmetry decreases. Visual inspection of the ELF topology confirms that all configurations, including the fully random DRX structure, exhibit 32 octahedral electride features in the 96-atom cell, consistent with one electride basin per carbon vacancy, as in the ordered Fd-3m structure.

These results establish that the anionic electron density occupying octahedral vacancies in Ti_2C is not a fragile consequence of crystallographic periodicity but is instead encoded in the local Ti octahedral coordination cage surrounding each vacancy. The invariance of Ti and C oxidation states across all configurations demonstrates that disordering the carbon sublattice

does not disrupt the charge transfer framework that generates octahedral electride features. The local electrostatic potential well responsible for electron trapping thus persists regardless of how carbon atoms are distributed among the octahedral sites.

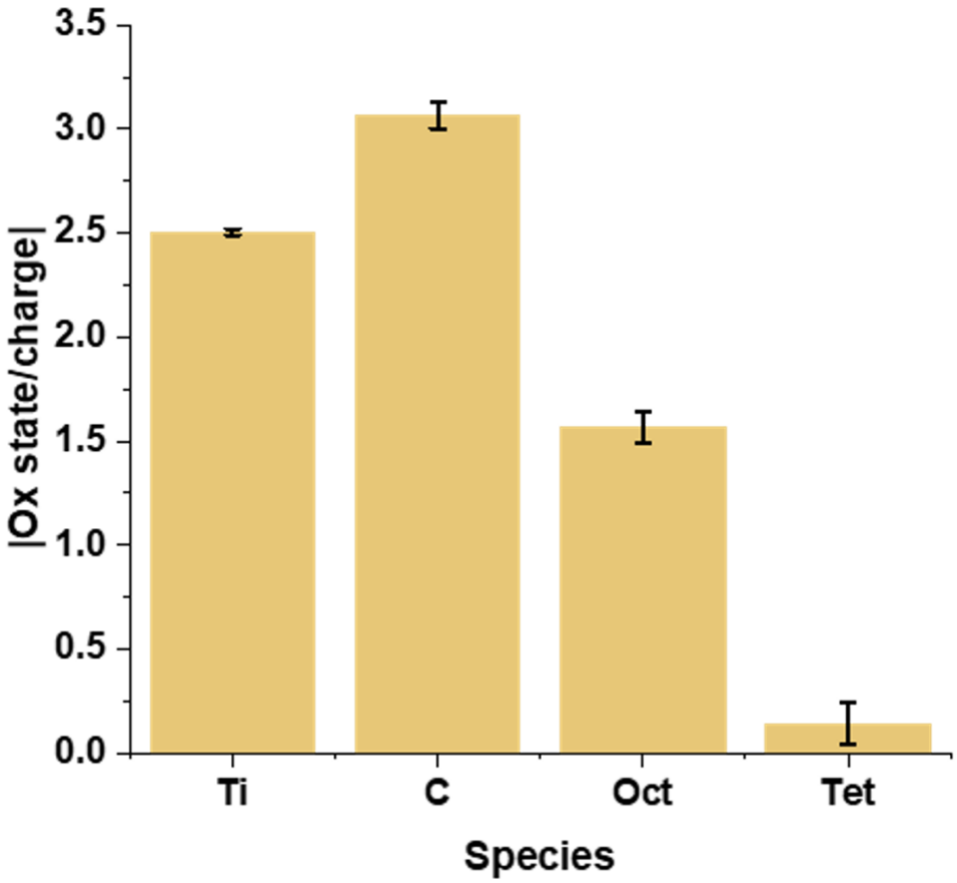


Figure 5-3. Charge/oxidation state statistics for Ti_2C. Average magnitude of oxidation state (Ti or C) or bare electron feature charge (octahedral or tetrahedral site) for BadELF analysis across partially ordered Ti_2C structures.

5.2.5 Tetrahedral Nodes in Network Topology

Compared to the electronic invariance observed in octahedral electride basins, the tetrahedral interstitial nodes, which connect adjacent octahedral electride sites in the Fd-3m network, are substantially modulated by disorder. Tetrahedral node charges display an average of –0.14 ± 0.10 (CV = 72%) with an order of magnitude more variability than any other feature. This variability is strongly correlated with local coordination environment, specifically the ratio of

the four nearest octahedral neighbor sites that are either C-occupied or vacant. We find that tetrahedral node sites with more C neighbors have monotonically decreasing charge (Figure 5-4). The two primary tetrahedral geometries associated with the electride network in Fd-3m are zero-C and two-C neighbor configurations. For the Fd-3m structure, zero-C nodes contain the largest charge of -0.22 ± 0.01 (CV = 2%) and two-C nodes contain 0.10 ± 0.001 (CV = 1%). Non-Fd-3m zero-C tetrahedral nodes also carry the largest charge with an average/variation of –0.29 ± 0.13 (CV = 45%), which is about 32% higher on average with much greater variability than the equivalent Fd-3m structure tetrahedral site. We find charge values of 0.10 ± 0.02 (CV = 20%) in two-C non-Fd-3m nodes, the average of which is consistent with Fd-3m but with increased variation. These results imply that global heterogeneity promotes preferential electronic localization and increased sensitivity to local environments in nodes within vacancy-rich regions.

No tetrahedral site with all four octahedral neighbors occupied by carbon is detected as an electride feature by BadELF under any parameter setting tested. This observation establishes an extinction threshold under which a tetrahedral void serves as an electride connectivity node only when at least one of its four neighboring octahedral sites is a carbon vacancy occupied by anionic electrons. For four-C nodes, the electron density is fully claimed by the C anions and no interstitial localization occurs. This conclusion establishes the role of tetrahedral sites less as independent charge reservoirs like octahedral vacancies but rather as coordination-sensitive bridging elements whose occupancy encodes local electride bonding topology. In the ordered Fd-3m structure, tetrahedral node geometry is globally symmetric. Upon disordering, electron localization in nodes is asymmetrically strengthened, weakened or extinguished, producing a heterogeneous but still globally connected 3D electride network. The electride state in Ti_2C is therefore robust to disorder because its principal charge carriers

(octahedral basins) are locally determined, while the network topology (mediated by tetrahedral nodes) is modulated but not destroyed by the loss of long-range order.

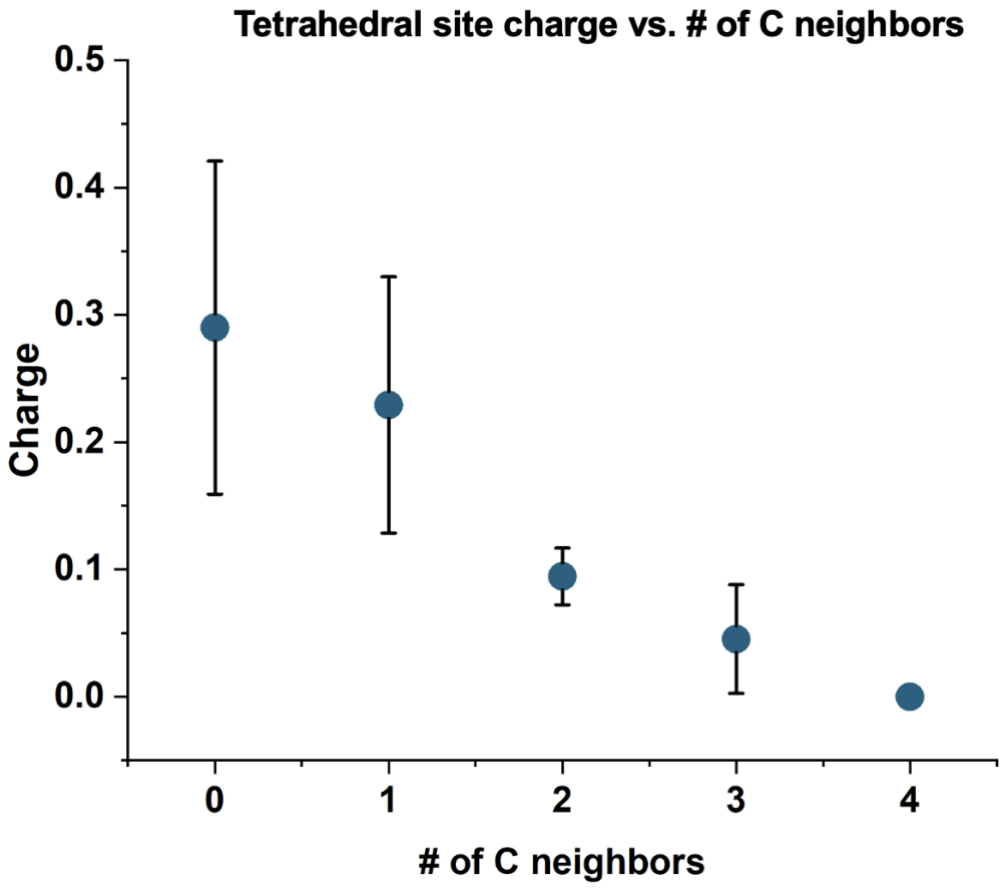


Figure 5-4. Average tetrahedral site charge vs. number of C neighbors. As the number of C neighbors increases, the tetrahedral site charge decreases and is full quenched when fully surrounded(4 neighbors) by C.

5.2.6 Visualizing Disorder-Induced Topological Changes in the ELF

The physical mechanism underlying tetrahedral node modulation is illustrated by examining the ELF response to minimal disordering events. Starting from the ideal Fd-3m structure, we displace a single carbon atom from its ordered position into an adjacent vacancy and calculate the new ELF topology (Figure 5-5). We color the surface topology via ΔELF and select an ELF isosurface value of 0.43 to most clearly highlight the regions of highest topological change. Red regions indicate increased ELF magnitude vs Fd-3m after C

displacement and blue regions indicate decreased ELF magnitude vs Fd-3m after C displacement. Only the atomic ELF of the displaced C is included, which has a greater ELF magnitude than the electride feature. Three main features emerge from this analysis. First, the original octahedral electride basin in Fd-3m (new C position in Figure 5-5) is annihilated by the displaced carbon atom and a new electride basin appears at the vacated carbon position, conserving the total number of octahedral electride features. Second, the two zero-C neighbor tetrahedral nodes that previously connected the now carbon-occupied electride site to its neighbors (original tetrahedral nodes in Figure 5-5) show diminished ELF magnitude. Third, four new one-C neighbor tetrahedral connections form around the newly created vacancy/electride site (new tetrahedral nodes in Figure 5-5). These new connections are visually thinner and have lower ELF magnitudes than the original Fd-3m nodes, indicating weaker but nonzero electride coupling. These findings are consistent with our BadELF charge analysis where zero-C tetrahedral nodes have greater charge magnitude which is correlated with visually thicker topological connections and higher ELF magnitudes. Furthermore, this analysis partly explains the variation in tetrahedral charge seen in vacancy-rich regions. In the C displaced structure, both the old and new tetrahedral nodes have a one-C configuration, but the new nodes are thicker (higher ELF magnitudes), which we propose is due to the now-increased vacancy concentration in that local environment.

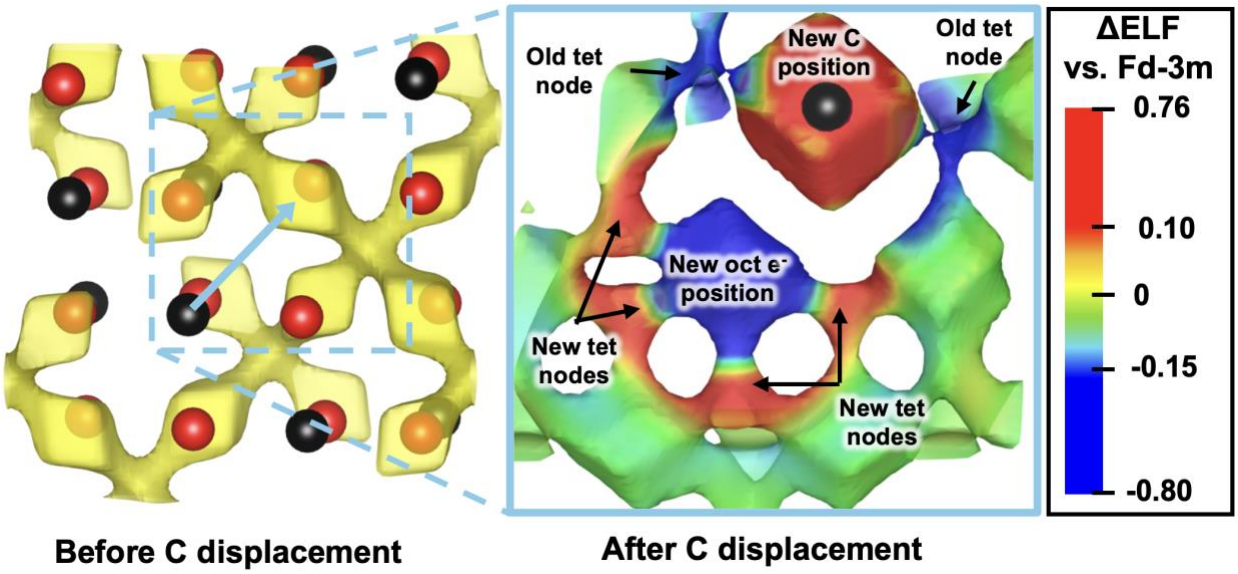


Figure 5-5. Impact of C displacement on ELF topology. (Left) ELF visualization of Fd-3m Ti2C before displacing one C atom. (Right) Resulting ELF visualization after C displacement The surface is colored by ΔELF before and after C displacement. This shows that (i) the octahedral electride feature swap places with the displaced C atom and (ii) the localization of the tetrahedral nodes decrease around the displaced C occupying the original vacancy position and increase around the electride occupying the new vacancy site.

A similar analysis displacing two nearby carbon atoms produces analogous changes, confirming that individual disordering events generate consistent aßnd localized perturbations to the electride topology without propagating disruption to the larger network. This locality is key to understanding why the global 3D network survives extensive disorder. Each carbon displacement disorders the local tetrahedral connectivity landscape, but the octahedral basins and the global network connectivity remain persistent.

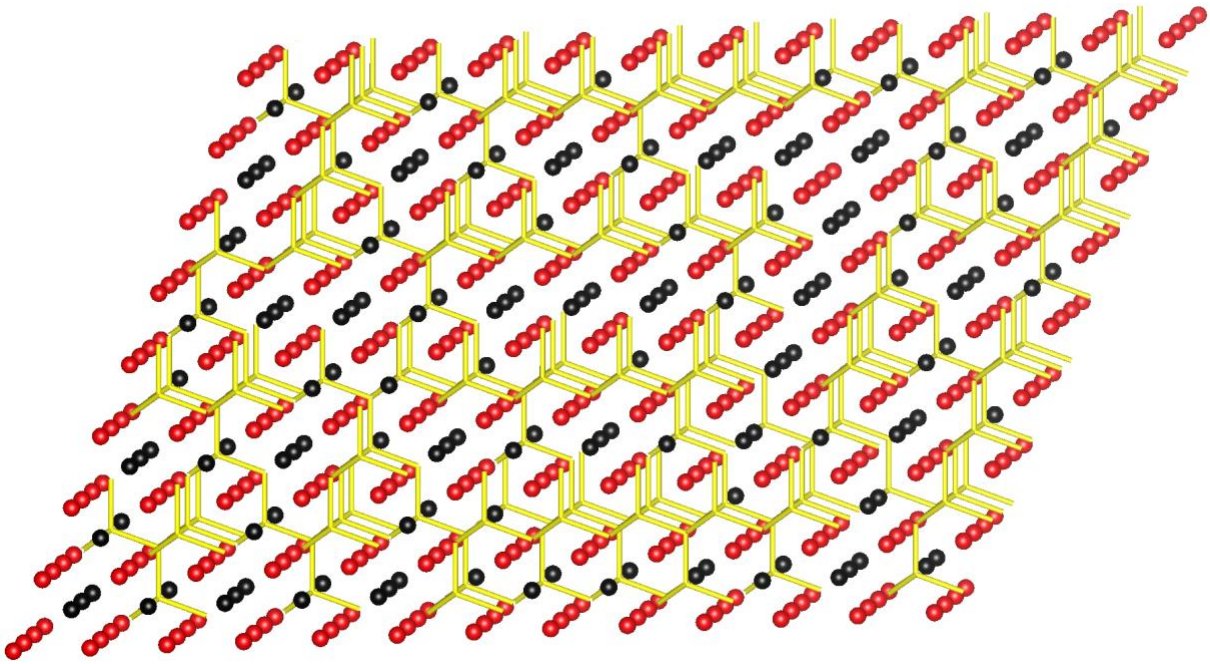


Figure 5-6: Partially ordered Ti_2C electron network. The structure depicts a final Monte Carlo simulation cell (some atoms not shown for visual clarity) of partially ordered Ti_2C. The yellow network illustrates the asymmetric but still 3D-connected electron network comprised of octahedral sites (bonds) and tetrahedral sites (nodes).

5.3 Conclusion

This work provides a unified account of carbon ordering kinetics and disorder-tolerant electride behavior in rocksalt Ti_2C. Cluster expansion and Monte Carlo simulations reconcile the thermodynamically predicted Fd-3m ground state with the mixed, partially ordered phases obtained experimentally by revealing that the majority of carbon ordering occurs within a narrow 600–800 K window where carbon diffusivity decreases by orders of magnitude, effectively arresting long-range order on accessible timescales.

The structural disorder of kinetically trapped Ti_2C does not destroy its global vacancy connectivity or 3D electride character. BadELF analysis demonstrated that total electride charge, Ti/C oxidation states, and primary octahedral electride site charge populations are conserved to within ~5% variance across the full order/disorder regime. In contrast, tetrahedral electride nodes are highly sensitive to local coordination. Their charge decreases in vacancy-

poor environments and are completely quenched when fully surrounded by carbon neighbors, establishing these sites as multi-centered bonding features that mediate network connectivity without disrupting the global electride manifold. This partially ordered structure with a disordered 3D-connected electron network is illustrated in Figure 5.6.

These findings constitute the first computational demonstration of an aperiodic 3D electride, supported by experimental synthesis of the kinetically arrested mixed-phase system. By decoupling electride character from long-range periodicity, this work substantially expands the viable design space for high-dimensional electron networks toward structurally disordered systems. In combination with the earth abundance and low cost of its constituent elements, Ti_2C has emerged as a compelling platform for disorder-tolerant electride design targeting FIB anode materials.

REFERENCES

(1) Druffel, D. L.; Pawlik, J. T.; Sundberg, J. D.; Mcrae, L. M.; Lanetti, M. G.; Warren, S. C. First-Principles Prediction of Electrochemical Electron-Anion Exchange: Ion Insertion without Redox. *Journal of Physical Chemistry Letters* 2020, *11* (1), 9210–9214. https://doi.org/10.1021/acs.jpclett.0c02266.

(2) Hosono, H.; Kitano, M. Advances in Materials and Applications of Inorganic Electrides. *Chem. Rev.* 2021, *121* (5), 3121–3185. https://doi.org/10.1021/acs.chemrev.0c01071.

(3) Dye, J. L. Electrides: Early Examples of Quantum Confinement. *Acc. Chem. Res.* 2009, *42* (10), 1564–1572. https://doi.org/10.1021/ar9000857.

(4) Sun, F.; Guo, Z.; Lu, Y.; Li, J.; Ye, T. N.; Hosono, H.; Wu, J. Electrides: Emerging Electronic Materials for Catalysis. *Fundamental Research*. KeAi Communications Co. January 1, 2025. https://doi.org/10.1016/j.fmre.2024.11.026.

(5) Meng, W.; Bai, J.; Ma, F.; Jiao, Y.; Wang, S.; Jiang, J.; Zhang, X.; Cheng, Z.; Yang, T. Magnetic Electrides: Recent Advances in Materials Realization and Application Prospects. *Applied Physics Reviews*. American Institute of Physics March 1, 2025. https://doi.org/10.1063/5.0233622.

(6) Zhang, X.; Yang, G. Recent Advances and Applications of Inorganic Electrides. *Journal of Physical Chemistry Letters* 2020, *11* (10), 3841–3852. https://doi.org/10.1021/acs.jpclett.0c00671.

(7) Alhasani, Z. A. A.; Ajeel, F. N. DFT Investigations of Structural and Electronic Properties of Two-Dimensional Y2C and Y2CF2 Monolayers. *Nano Trends* 2025, *9*. https://doi.org/10.1016/j.nwnano.2025.100073.

(8) Zhang, X.; Xiao, Z.; Lei, H.; Toda, Y.; Matsuishi, S.; Kamiya, T.; Ueda, S.; Hosono, H. Two-Dimensional Transition-Metal Electride Y2C. *Chemistry of Materials* 2014, *26* (22), 6638–6643. https://doi.org/10.1021/cm503512h.

(9) Tojigamori, T.; Matsui, N.; Suzuki, K.; Hirayama, M.; Abe, T.; Kanno, R. Fluorination/Defluorination Behavior of Y2C in Fluoride-Ion Battery Anodes. *ACS Appl. Energy Mater.* 2024, *7* (3), 1100–1108. https://doi.org/10.1021/acsaem.3c02613.

(10) McRae, L. M.; Radomsky, R. C.; Pawlik, J. T.; Druffel, D. L.; Sundberg, J. D.; Lanetti, M. G.; Donley, C. L.; White, K. L.; Warren, S. C. Sc2C, a 2D Semiconducting Electride. *J. Am. Chem. Soc.* 2022, *144* (24), 10862–10869. https://doi.org/10.1021/jacs.2c03024.

(11) Park, J.; Hwang, J. Y.; Lee, K. H.; Kim, S. G.; Lee, K.; Kim, S. W. Tuning the Spin-Alignment of Interstitial Electrons in Two-Dimensional Y2C Electride via Chemical Pressure. *J. Am. Chem. Soc.* 2017, *139* (48), 17277–17280. https://doi.org/10.1021/jacs.7b10338.

(12) Tang, H.; Wan, B.; Gao, B.; Muraba, Y.; Qin, Q.; Yan, B.; Chen, P.; Hu, Q.; Zhang, D.; Wu, L.; Wang, M.; Xiao, H.; Gou, H.; Gao, F.; Mao, H. kwang; Hosono, H. Metal-to-Semiconductor Transition and Electronic Dimensionality Reduction of Ca2N Electride under Pressure. *Advanced Science* 2018, *5* (11). https://doi.org/10.1002/advs.201800666.

(13) Faseela, K. P.; Kim, Y. J.; Kim, S. G.; Kim, S. W.; Baik, S. Dramatically Enhanced Stability of Silver Passivated Dicalcium Nitride Electride: Ag-Ca2N. *Chemistry of Materials* 2018, *30* (21), 7803–7812. https://doi.org/10.1021/acs.chemmater.8b03202.

(14) Li, W.; You, Y.; Choi, J. H. Oxidation, Stability, and Magnetic Ground States of Two-Dimensional Layered Electrides. *Journal of Physical Chemistry C* 2020, *124* (46), 25316–25321. https://doi.org/10.1021/acs.jpcc.0c07337.

(15) Wang, D.; Li, H.; Zhang, L.; Sun, Z.; Han, D. X.; Niu, L.; Zhong, X.; Qu, X.; Yang, L. First-Principles Study on OH-Functionalized 2D Electrides: Ca 2 NOH and Y 2 C(OH) 2 , Promising Two-Dimensional Monolayers for Metal-Ion Batteries. *Appl. Surf. Sci.* 2019, *478*, 459–464. https://doi.org/10.1016/j.apsusc.2019.01.256.

(16) Li, K.; Gong, Y.; Wang, J.; Hosono, H. Electron-Deficient-Type Electride Ca5Pb3: Extension of Electride Chemical Space. *J. Am. Chem. Soc.* 2021, *143* (23), 8821–8828. https://doi.org/10.1021/jacs.1c03278.

(17) Weaver, S. M.; Lanetti, M. G.; Slamowitz, C. C.; Radomsky, R. C.; Warren, S. C. Assessing Dimensionality in Electrides. *The Journal of Physical Chemistry C* 2025. https://doi.org/10.1021/acs.jpcc.4c06803.

(18) Royce, B. S. H. *THE CREATION OF DEFECTS IN ALKALI HALIDES*; 1967.

(19) Yang, J.; Pan, J.; Deng, J.; Zhang, Y. F.; Li, Y.; Zhu, Y.; Wan, G.; Du, S. Vacancy-Induced Anionic Electrons in Single-Metal Oxides and Their Possible Applications in Ammonia Synthesis. *J. Am. Chem. Soc.* 2024, *146* (30), 21160–21167. https://doi.org/10.1021/jacs.4c07362.

(20) Chae, J.; Kim, G. Effects of a Single Vacancy on Electronic Properties of a Ca2N Electride Bilayer. *Appl. Surf. Sci.* 2023, *612*. https://doi.org/10.1016/j.apsusc.2022.155721.

(21) Sung Wng Kim; Terumasa Shimoyama; Hideo Hosono. Solvated Electrons in High-Temperature and Glasses of TheRoom-Temperature Electride [Ca24Al28O64]4+ 4e−. *Science (1979).* 2011, *333* (6038), 68–71. https://doi.org/10.1126/science.1202232.

(22) Johnson, L. E.; Sushko, P. V.; Tomota, Y.; Hosono, H. Electron Anions and the Glass Transition Temperature. *Proc. Natl. Acad. Sci. U. S. A.* 2016, *113* (36), 10007–10012. https://doi.org/10.1073/pnas.1606891113.

(23) Akola, J.; Kohara, S.; Ohara, K.; Fujiwara, A.; Watanabe, Y.; Masuno, A.; Usuki, T.; Kubo, T.; Nakahira, A.; Nitta, K.; Uruga, T.; Richard Weber, J. K.; Benmore, C. J. Network Topology for the Formation of Solvated Electrons in Binary CaO-Al2O3 Composition Glasses. *Proc. Natl. Acad. Sci. U. S. A.* 2013, *110* (25), 10129–10134. https://doi.org/10.1073/pnas.1300908110.

(24) Ahmed, S.; González-Cataldo, F.; Robinson, V. N.; Militzer, B. Electride Behavior at High Pressure in Silicon and Other Elements in Solid and Liquid Phases. *Phys. Rev. B* 2025, *112* (16), 1651111–16511113. https://doi.org/10.1103/14dp-bf1n.

(25) Weinberger, C. R.; Thompson, G. B. Review of Phase Stability in the Group IVB and VB Transition-Metal Carbides. *Journal of the American Ceramic Society* 2018, *101* (10), 4401–4424. https://doi.org/10.1111/jace.15768.

(26) Yu, X. X.; Weinberger, C. R.; Thompson, G. B. Ab Initio Investigations of the Phase Stability in Group IVB and VB Transition Metal Carbides. *Comput. Mater. Sci.* 2016, *112*, 318–326. https://doi.org/10.1016/j.commatsci.2015.10.038.

(27) Goretzki, H. Neutron Diffraction Studies on Titanium-Carbon and Zirconium-Carbon Alloys. *physica status solidi (b)* 1967, *20* (2), K141–K143. https://doi.org/10.1002/pssb.19670200260.

(28) Bell, P. S.; Lewis, M. H. The Ordered Distribution of Carbon Atoms in Titanium Carbide. *Philosophical Magazine* 1971, *24* (191), 1247–1251. https://doi.org/10.1080/14786437108217083.

(29) Em, V. T.; Tashmetov, M. Y. The Structure of the Ordered Phase in Rocksalt Type Titanium Carbide, Carbidenitride, and Carbidehydride. *Phys. Status Solidi B Basic Res.* 1996, *198* (2), 571–575. https://doi.org/10.1002/pssb.2221980202.

(30) Nguyen, J.; Glandut, N.; Jaoul, C.; Lefort, P. Electrochemical Hydrogen Insertion in Substoichiometric Titanium Carbide TiC0.6: Influence of Carbon Vacancy Ordering. *Langmuir* 2013, *29* (38), 12036–12042. https://doi.org/10.1021/la402043x.

(31) Francisco, S. *The Percolation Model*; 1978.

(32) Chang, J. H.; Kleiven, D.; Melander, M.; Akola, J.; Garcia-Lastra, J. M.; Vegge, T. CLEASE: A Versatile and User-Friendly Implementation of Cluster Expansion Method. *Journal of Physics Condensed Matter* 2019, *31* (32). https://doi.org/10.1088/1361-648X/ab1bbc.

(33) Van Loo, F. J. J.; Wakelkamp, W.; Bastin, G. F.; Metselaar, R. Diffusion of Carbon in TiC1-y and ZrC1-y. *Solid State Ion.* 1989, *32–33* (PART 2), 824–832. https://doi.org/10.1016/0167-2738(89)90364-0.

(34) Uxa, D.; Hüger, E.; Meyer, K.; Dörrer, L.; Schmidt, H. Lithium-Ion Diffusion in Near-Stoichiometric Polycrystalline and Monocrystalline LiCoO2. *Chemistry of Materials* 2023, *35* (8), 3307–3315. https://doi.org/10.1021/acs.chemmater.3c00359.

(35) Luis, F.; Moncayo, G. ELF: The Electron Localization Function.

(36) Burdett, J. K.; Mccormick, T. A. *Electron Localization in Molecules and Solids: The Meaning of ELF*; 1998. https://pubs.acs.org/sharingguidelines.

(37) Weaver, S. M.; Sundberg, J. D.; Slamowitz, C. C.; Radomsky, R. C.; Lanetti, M. G.; McRae, L. M.; Warren, S. C. Counting Electrons in Electrides. *J. Am. Chem. Soc.* 2023. https://doi.org/10.1021/jacs.3c10876.

APPENDIX: SUPPORTING INFORMATION FOR CHAPTER 3

A3.1 Dataset of 168 ternary fluoride material pairs identified from high throughput screening.

f_form	def_form	voltage	per_exp	grav_cap	grav_e_den	f_cost_p_kg
Ca5P3O12F	Ca5(PO4)3	-0.92	-0.53	53.15	-48.81	1.54
TbSF	TbS	0.42	16.4	127.63	53.67	498.19
YSF	YS	0.47	16.62	191.48	90.23	19.98
ReO3F	ReO3	3.48	46.43	105.85	367.87	2707.94
CeOF	CeO	0.08	48.66	153.05	12.81	3.95
PrSF	PrS	0.47	14.15	139.61	66.26	75.82
PrOF	PrO	-0.43	40.94	152.36	-65.73	82.74
LaOF	LaO	-0.49	42.99	154.12	-76.09	4.11
P3Pb5O12F	P3Pb5O12	0.64	2.44	20	12.86	1.78
NdSF	NdS	0.48	14.71	137.23	65.69	42.68
Rh(OF3)2	RhO2	4.49	328.34	646.09	2899.01	60778.08
CeSF	CeS	0.75	19.15	140.19	105.84	3.62
SmSF	SmS	0.46	15.28	133.06	61.47	10.58
Ca10Si6F	Ca5Si3	-0.56	-0.51	45.56	-25.71	2.11
TlSnF3	TlSn	1.91	72.12	211.54	403.91	2264.59
LaSF	LaS	0.44	13.73	141.08	61.64	3.76

ZrNF	ZrN	1.35	59.59	215.74	291.31	26.98
BaAlGeF	BaAlGe	0.04	5.27	104.71	3.83	278.04
LaSeF	LaSe	0.42	13.07	113.15	47.74	10.14
Ca2NF	Ca2N	-0.56	-11.6	236.84	-133.46	1.97
V3Pb5O12F	V3Pb5O12	1.05	0.12	19.15	20.15	41.49
ScOF	ScO	-0.03	57.36	335.21	-9.68	1945.98
TmSeF	TmSe	0.23	36.89	100.42	22.97	1905.38
ThNF	ThN	0.04	37.69	101.12	4.18	251.41
ReO2F3	ReO2	2.96	221.47	292.17	866.24	2491.76
Nb2O2F3	NbO	1.78	83.31	292.59	520.31	50.06
Sr2FeO3F	Sr2FeO3	1.02	8.18	89.91	91.59	4.11
Ca5V3O12F	Ca5V3O12	0.61	1.86	47.5	28.9	100.07
Ca6Al7O16F	Ca6Al7O16	-0.22	-0.64	38.05	-8.28	1.37
Gd2CF2	Gd2C	-0.08	12.03	147.06	-12.21	24.89
Ho2CF2	Ho2C	-0.21	9.31	141.11	-29.14	49.79
Sr2NF	Sr2N	-0.33	-12.45	128.7	-42.75	5.75
GdSF	GdS	0.61	17.47	128.66	78.51	21.79
LuSF	LuS	0.29	44.15	118.57	34.95	497.92
Rb2UF7	Rb2UF6	2.53	32.04	49.45	125.07	4933.65
LiAgF4	LiAgF3	4.35	21.43	140.47	611	298.38

LiBiF6	LiBiF5	4.25	4.43	81.24	344.94	6.48
NaTiF4	Na2Ti2F7	0.43	10.29	91.25	39.3	5.23
Li2CuF6	Li2CuF5	5.49	10.33	140.02	769.17	9.24
Rb3TiF7	Rb3TiF6	0.89	2.84	61.29	54.85	9090.87
Cs3TiF7	Cs3TiF6	0.8	4.66	46.24	36.97	42516.68
Sb2XeF16	Sb2XeF13	4.96	16.63	118.45	587.55	351.14
LiCu2F6	LiCu2F5	3.84	-1.1	108.06	414.48	6.34
CsCu2F6	CsCu2F5	4.11	5.81	71.66	294.5	21964.75
CsReF8	CsReF6	3.79	9.7	113.78	431.06	18890.86
Rb2CuF6	Rb2CuF4	4.41	31.23	153.82	679.05	7604.95
NbOF3	Nb2O2F3	2.03	56.88	242.33	492.1	41.81
KAgF4	KAgF3	4.27	26.66	120.21	513.03	255.01
NaVF6	NaVF4	3.64	38.12	285.24	1039.56	100.8
K2TiF6	K2TiF5	0.94	8.26	111.65	105.31	7.43
KVOF4	KVOF3	3.19	17.46	147.23	470.09	106.05
Sb2XeF16	Sb2XeF15	4.71	8.75	39.48	185.79	351.14
CeAsO4F	CeAsO4	2.37	26.77	89.93	212.95	2.64
MnZnF6	MnZnF5	4.13	12.41	114.37	472.06	2.12
TiPO4F	TiPO4	1.44	25.92	165.61	238.01	4.18
RbCrF6	RbCrF5	4.94	14.32	106.59	526.31	5271.21

Cs2AgF6	Cs2AgF4	4.57	26.36	109.92	502.15	33800.64
Na2TiF6	Na2TiF5	1.05	18.93	128.95	135.16	4.4
TiH8(NF3)2	TiH8N2F5	1.15	9.13	135.41	156.26	3.99
CaTiF6	CaTiF5	1.36	34.48	132.72	180.17	4.29
LiVF4	Li2V2F7	1.46	20.05	100.1	146.13	144.74
MgTiF6	MgTiF5	1.18	18.13	143.97	169.26	4.46
LiFeF6	LiFeF5	5.6	11.36	151.61	848.4	4.71
SbH7F12	SbH7F11	1.7	8.48	75.12	128.04	3.29
Li2AgF6	Li2AgF5	5.16	6.2	113.69	586.62	244.28
Pt(OF3)2	PtO2	4.6	290.79	471.48	2168.93	15901.48
OsOF5	OsOF4	3.49	20.95	88.98	310.7	7578.99
LiMnF4	Li2Mn2F7	3.02	-0.66	97.2	293.65	6.04
CaPdF6	CaPdF4	3.91	45.13	205.78	804.34	20223.97
RbSnF3	Rb16Sn16F47	0.02	7.8	6.41	0.11	5081.25
Rb2MnF6	Rb2MnF5	3.54	2.24	78.86	279.03	7796.74
CaMnF6	CaMnF5	4.15	19.43	128.23	532.24	2.01
NbCl4F	NbCl4	2.09	16.71	105.64	221.09	27.07
LiAgF6	LiAgF4	5.77	27.93	234.28	1351.05	249.16
Na2PdF6	Na2PdF4	3.65	32.36	201.22	734.49	19776.11
TaCl4F	TaCl4	1.52	24.26	78.42	119.05	162.16

Cs2MnF6	Cs2MnF5	3.5	4.84	61.65	215.56	37786.88
CaCoF6	CaCoF5	4.94	24.74	125.83	621.69	10.58
Na3MoO4F	Na3MoO4	0.77	6.96	108.11	83.23	16.55
VPO4F	VPO4	3.15	26.68	162.52	512.32	113.85
IO2F	IO2	3.42	22.12	150.65	514.51	25.21
Ba2Mn2F11	BaMnF5	5.4	14.13	45.16	243.75	1.16
LuSeO3F	LuSeO3	1.41	27.7	83.51	118.07	355.97
VOF3	VOF2	3.74	45.04	216.25	808.41	151.38
ZnCoF6	ZnCoF5	5.22	20.69	112.45	587.01	9.77
ZnNiF6	ZnNiF5	5.35	18.11	112.57	602.16	5.09
TmSeO3F	TmSeO3	1.62	4.85	85.11	138.07	1614.97
AgAsF7	AgAsF6	4.52	-5.99	84.87	383.68	179.09
K2ReF8	K2ReF6	3.01	16.95	128.73	387.95	1649.72
MgMnF6	MgMnF5	4.06	13.67	138.7	563.17	1.99
Cd(AuF6)2	Cd(AuF4)2	4.96	29.13	145.99	724.39	24034.28
LiVF6	LiVF5	3.81	24.73	155.94	594.01	113.18
YSeO3F	YSeO3	1.48	29.57	114.12	168.83	19.12
Li2MnF6	Li2MnF5	4.04	10.12	146.61	592.94	8.14
K2PdF6	K2PdF4	3.6	12.95	179.51	645.55	17645.36
MgCoF6	MgCoF5	5.28	22.14	135.89	717.86	11.25

BaFeF5	Ba7Fe7F34	2.67	1.65	13.29	35.44	0.87
KTlF4	KTlF3	3.1	-8	83.89	259.79	2688.99
NClOF4	NClO	4.54	55.83	757.89	3443.89	1.13
LiAuF6	LiAuF4	4.87	22.15	168.62	820.98	27760.2
Sb2XeF16	Sb2XeF14	5.09	16.75	78.97	402.12	351.14
MgNiF6	MgNiF5	5.41	8.73	136.06	735.39	5.59
RbTlF4	RbTlF3	3.28	4.26	73.26	240.04	5967.87
KVF4	KVF3	1.72	28.06	161.42	276.94	116.25
LiCrPO4F	LiCrPO4	1.77	14.65	155.01	274.98	6.94
CaNiF6	CaNiF5	5.5	22.87	125.97	692.98	5.34
LiV2F6	LiV2F5	1.34	-3.47	120.29	161.38	170.98
CsTlF4	CsTlF3	3.42	7.63	64.85	221.98	21951.38
WOF4	WOF3	2.82	38.72	97.17	274.2	24.09
KAuF6	KAuF4	4.8	19.8	153.13	735.13	25209.83
Li2VF6	Li2VF5	3.18	11.15	149.88	476.56	112.03
Ba(AuF6)2	Ba(AuF4)2	5.24	52.8	141.2	740.16	23245.19
Li2CoO2F	Li2CoO2	1.26	11.07	216.47	272.2	25.32
LiVPO4F	LiVPO4	1.66	24.37	155.96	259.21	112.63
CsVOF4	CsVOF3	3.07	23.23	97.16	298.72	29844.68
CaCrF6	CaCrF5	4.47	22.73	130.06	581.96	3.93

Sb2XeF16	Sb2XeF12	5.11	16.3	157.94	807.63	351.14
KMnF4	KMnF3	3.26	18.8	157.63	513.21	4.45
S(OF)2	SO2	3.2	15.8	525.21	1682.65	0.83
BaWF7	Ba2W2F11	2.25	6.33	88.52	198.75	14.96
CaFeF5	CaFeF4	2.67	28.99	140.38	375.48	1.6
RbBiF6	RbBiF4	4.19	38.21	131.24	549.73	3247.27
KCrF6	KCrF4	4.7	27.75	261.37	1227.89	5.96
Sb2BrF17	Sb2BrF15	5.48	10.25	82.93	454.38	3.73
MgAs2(XeF9)2	MgAs2(XeF8)2	5.05	-0.71	68.84	347.54	608.15
Rb2MnF6	Rb2MnF4	3.26	25.46	157.72	514.23	7796.74
ZnCrF6	ZnCrF5	4.38	14.78	115.83	507.63	3.82
As(BrF2)3	AsBr3	3.66	29.02	375.17	1373.2	3.19
SbClF10	SbClF8	5	16.41	154.39	771.69	3.14
BaFeF5	BaFeF4	2.69	16.03	93.01	250.12	0.87
AgBF5	AgBF4	4.36	23.65	125.43	546.31	264.1
MgCrF6	MgCrF5	4.28	20.04	140.84	602.97	4.07
LiFe2F6	LiFe2F5	2.63	6.47	115.22	303.27	3.68
KBiF6	KBiF4	4.32	46.49	148.05	640.22	5.7
NaCrF6	NaCrF4	4.81	39.53	283.65	1364.92	4.17
LiFeF6	LiFeF4	5.61	17.32	303.22	1702.09	4.71

CsBrF6	CsBrF4	4.28	20.57	164.02	701.51	25135.07
K2NiF6	K2NiF4	4.71	27.61	213.66	1006.47	8.19
LiMnPO4F	LiMnPO4	3.29	15.87	152.41	500.93	4.61
Rb2CrF6	Rb2CrF5	4.62	20.08	79.55	367.51	7865.97
CaWF6	CaWF5	1.81	21.78	79.32	143.47	20.15
Cs2MnF6	Cs2MnF4	3.16	31.6	123.3	389.19	37786.88
YbOF	YbO	2.73	42.28	128.83	351.47	14.42
CaSnF6	CaSnF4	2.32	67.63	196.51	455.51	9.31
LiMnF4	LiMnF3	3.39	15.96	194.39	658.39	6.04
BaCrF6	BaCrF5	4.41	12.98	88.36	389.81	2.48
BaSnF6	BaSnF4	2.41	14.88	144.86	349.8	6.71
CaMoF6	CaMoF5	2.8	20.13	107.2	300.56	16.67
Rb2NiF6	Rb2NiF4	4.6	32.25	156	717.81	7713.61
MgMoF6	MgMoF5	2.57	16.41	114.42	293.77	17.64
K2CrF6	K2CrF5	4.79	14.97	109.76	526.25	7.07
TlSbF6	TlSbF4	2.86	27.84	121.79	348.65	1952.46
LiFePO4F	LiFePO4	2.83	20.18	151.63	429.06	4.16
RbBrF4	RbBr	4.05	63.94	444.16	1800.84	5490.66
FeSO4F	FeSO4	3.12	16.32	156.82	489.12	0.44
CaNiF6	CaNiF4	5.14	59.38	251.94	1295.34	5.34

NaSbF6	NaSbF4	2.91	51.03	207.17	601.89	3.88
KBrF4	KBr	3.92	48.83	549.79	2153.5	5.17
Rb3CrF7	Rb3CrF6	4.23	4.76	60.72	256.77	9005.7
CsSbF6	CsSbF4	2.77	24.19	145.4	403.46	22282.27
KSbF6	KSbF4	2.88	22.67	195.03	562.38	5.23
CsAsF6	CsAsF4	2.96	10.6	166.56	492.84	25523.39
BaNiF6	BaNiF4	5.45	23.49	172.91	941.59	3.49
ReSbOF10	ReSbOF9	3.05	15.99	52.15	159.09	1336.13
LiBiF6	LiBiF4	4.7	40.5	162.48	763.96	6.48
SrNiF6	SrNiF4	5.17	23.4	205.92	1065.49	6.24
CsSO3F	CsSO3	2.67	12.69	115.54	308.06	35408.5
LiSbF6	LiSbF4	2.94	30.71	220.87	650.26	6.24

Table A3-1: Dataset of 168 ternary fluoride material pairs identified from high throughput screening.

APPENDIX: SUPPORTING INFORMATION FOR CHAPTER 4

A4.1 Subset of competing formation energetics identified from high throughput screening. The metal fluoride and metal carbide pairing with the highest voltage difference is given for each element. Red coloring indicates greater thermodynamic drive for metal fluoride formation, and green coloring indicates greater thermodynamic drive for metal carbide formation.

f_form	c_form	voltage_metal	voltage_carbide	voltage_diff	f_e_hull	c_e_hull
AgF	AgC	3.864	-0.607	-4.471	0.000	2.236
AlF3	Al4C3	1.171	1.225	0.054	0.000	0.000
AsF3	As4C3	3.029	2.520	-0.509	0.000	0.872
AuF3	AuC	4.571	3.320	-1.251	0.000	1.877
BaF2	BaC6	0.086	0.385	0.299	0.000	0.000
BeF2	Be2C	1.003	1.177	0.174	0.000	0.000
BF3	B4C	2.182	2.224	0.042	0.000	0.000
CaF2	CaC2	-0.005	-0.024	-0.020	0.000	0.013
CdF2	Cd3C	2.611	1.798	-0.813	0.000	1.220
CeF3	Ce2C3	0.588	0.802	0.214	0.000	0.000
CoF2	Co2C	2.804	2.723	-0.081	0.000	0.108
CrF3	Cr3C2	2.276	2.332	0.056	0.000	0.000
CsF	CsC8	0.647	1.059	0.412	0.000	0.000
CuF2	CuC6	3.612	-1.044	-4.657	0.000	1.331

DyF3	Dy3C4	0.375	0.622	0.247	0.000	0.000
ErF3	Er15C19	0.370	0.628	0.259	0.000	0.005
EuF3	EuC6	1.260	1.404	0.144	0.000	0.000
FeF2	Fe23C6	2.444	2.411	-0.033	0.000	0.052
GaF3	GaC	2.426	1.762	-0.664	0.000	0.995
GdF3	Gd2C3	0.848	1.040	0.192	0.000	0.000
GeF2	GeC	2.745	2.307	-0.437	0.000	0.437
HfF4	HfC	1.173	1.643	0.470	0.000	0.000
HgF	Hg3C	3.493	1.480	-2.013	0.000	1.510
HoF3	Ho4C7	0.378	0.648	0.270	0.000	0.000
InF3	InC	2.552	1.583	-0.970	0.000	1.455
IrF3	IrC	4.185	3.831	-0.354	0.000	0.531
KF	KC8	0.460	0.788	0.328	0.000	0.000
LaF3	La2C3	0.342	0.481	0.139	0.000	0.000
LiF	LiC12	0.000	0.082	0.082	0.000	0.000
LuF3	Lu4C7	0.394	0.693	0.299	0.000	0.000
MgF2	Mg15C	0.588	0.440	-0.148	0.000	0.277
MnF2	Mn23C6	1.879	1.939	0.060	0.000	0.000
MoF3	Mo2C	2.643	2.700	0.057	0.000	0.000
NaF	NaC	0.455	-0.004	-0.459	0.000	0.229

Nb2F5	Nb2C	2.129	2.409	0.280	0.000	0.000
NbF4	Nb6C5	2.345	2.595	0.250	0.068	0.000
NdF3	Nd2C3	0.352	0.491	0.139	0.000	0.000
NiF2	Ni3C	2.853	2.814	-0.039	0.000	0.058
NpF3	Np2C3	1.268	1.233	-0.034	0.000	0.041
OsF5	OsC	3.878	3.592	-0.286	0.000	0.716
PbF2	PbC	2.308	0.822	-1.486	0.000	1.486
PdF2	PdC	4.270	3.055	-1.215	0.027	1.215
PrF3	Pr2C3	0.449	0.567	0.118	0.000	0.000
PtF4	PtC	4.369	3.914	-0.455	0.000	0.910
PuF3	Pu2C3	1.026	1.063	0.036	0.000	0.000
RbF	RbC8	0.583	0.964	0.382	0.000	0.000
ReF6	Re2C	3.441	3.448	0.007	0.000	0.000
RhF3	RhC	3.882	3.509	-0.373	0.000	0.560
RuF3	RuC	3.811	3.568	-0.243	0.000	0.365
ScF3	Sc3C4	0.601	0.919	0.318	0.000	0.000
SeF4	CSe2	3.741	3.607	-0.134	0.000	0.357
SiF4	SiC	1.989	2.091	0.102	0.000	0.000
SmF3	Sm2C3	0.404	0.576	0.172	0.000	0.000
SnF2	SnC	2.477	1.661	-0.817	0.000	0.817

SrF2	SrC6	-0.017	0.135	0.152	0.000	0.000
TaF5	TaC	2.043	2.274	0.231	0.000	0.000
TbF3	Tb4C5	0.375	0.607	0.232	0.000	0.000
TiF3	TiC	1.437	1.977	0.540	0.000	0.000
TlF	TlC	2.398	-1.562	-3.961	0.000	1.980
TmF3	Tm4C7	0.835	1.123	0.288	0.000	0.000
VF2	V6C5	1.832	2.331	0.499	0.000	0.000
WF4	W2C	3.047	3.053	0.006	0.000	0.065
YbF2	YbC6	-0.369	-0.075	0.294	0.000	0.000
YF3	Y4C7	0.428	0.685	0.257	0.000	0.000
ZnF2	Zn3C	2.427	1.734	-0.693	0.000	1.040
ZrF4	ZrC	1.329	1.731	0.402	0.000	0.000

Table A4-1. Subset of competing formation energetics identified from high throughput screening.